Polarization Effects in Group III-Nitride Materials and Devices

by

Qiyuan Wei

A Dissertation Presented in Partial Fulfillment
of the Requirements for the Degree
Doctor of Philosophy

Approved April 2012 by the
Graduate Supervisory Committee:

Fernando Ponce, Chair
Kong-Thon Tsen
John Shumway
Jose Menendez
David Smith

ARIZONA STATE UNIVERSITY

May 2012

ABSTRACT

Group III-nitride semiconductors have wide application in optoelectronic devices. Spontaneous and piezoelectric polarization effects have been found to be critical for electric and optical properties of group III-nitrides. In this dissertation, firstly, the crystal orientation dependence of the polarization is calculated and in-plane polarization is revealed. The in-plane polarization is sensitive to the lateral characteristic dimension determined by the microstructure. Specific semi-polar plane growth is suggested for reducing quantum-confined Stark effect.

The macroscopic electrostatic field from the polarization discontinuity in the heterostructures is discussed, b ased on that, the band diagram of InGaN/GaN quantum well/barrier and AlGaN/GaN heterojunction is obtained from the self-consistent solution of Schrodinger and Poisson equations. New device design such as triangular quantum well with the quenched polarization field is proposed.

Electron holography in the transmission electron microscopy is used to examine the electrostatic potential under polarization effects. The measured potential energy profiles of heterostructure are compared with the band simulation, and evidences of two-dimensional hole gas (2DHG) in a wurtzite AlGaN/ AlN/ GaN superlattice, as well as quasi two-dimensional electron gas (2DEG) in a zinc-blende AlGaN/GaN are found. The large polarization discontinuity of AlN/GaN is the main source of the 2DHG of wurtzite nitrides, while the impurity introduced during the growth of AlGaN layer provides the donor states that to a great extent balance the free electrons in zinc-blende nitrides. It is also found that the quasi-2DEG concentration in zinc-blende AlGaN/GaN is about one order of magnitude lower than the wurtzite AlGaN/GaN, due to the absence of polarization.

Finally, the InAlN/GaN lattice-matched epitaxy, which ideally has a zero piezoelectric polarization and strong spontaneous polarization, is experimentally studied. The breakdown in compositional homogeneity is triggered by threading dislocations with a screw component propagating from the GaN underlayer, which tend to open up into V-grooves at a certain thickness of the $In_xAl_{1-x}N$ layer. The V-grooves coalesce at 200 nm and are filled with material that exhibits a significant drop in indium content and a broad luminescence peak. The structural breakdown is due to heterogeneous nucleation and growth at the facets of the V-grooves.

To my parents and my wife.

ACKNOWLEDGMENTS

I feel very fortunate to conduct the research under the supervision of Prof. Fernando Ponce. He taught me a lot about how to approach research problems, how to analyze and understand the results from a physicist's perspective. He never runs out of ideas and always has the magic to solve difficult problems. I also appreciate his patience and trust before I developed the maturity during the research.

I would also like to thank my committee members- Prof. David Smith, Prof. John Shumway, Prof. Jose Menendez, Prof. Kong-Thon Tsen, -for reviewing this dissertation.

I am extremely grateful to Prof. David Smith for his wonderful teaching of transmission electron microscopy, and Prof. Martha Mccartney for her contribution to the electron holography built at ASU. I appreciate Dr. Zhihao Wu, Dr. Lin Zhou and Dr. Kewei Sun for sharing their hands-on experience of microscopy. Also thanks to Dr. Alec Fischer, Dr. Yu Huang, Mr. Reid Juday, Ms. Jingyi Huang and Mr. Yong Wei for their collaboration.

I want to thank Prof. Ferdinand Scholz and Dr. Joachim Hertkorn at Ulm University, Germany; Prof. Donat As at Universität Paderborn, Germany; Prof. Takashi Egawa and Dr. Zhitao Chen at Nagoya Institute of Technology, Japan, for providing samples and interesting topics that are the subject of the research reported here.

I sincerely thank my parents for their support throughout my long schooling. I deeply appreciate my wife Ti Li for her constant love.

TABLE OF CONTENTS

Page

CHAPTER Page

LIST OF TABLES

Table Page

LIST OF FIGURES

FIGURE Page

FIGURE Page

FIGURE Page

FIGURE Page

CHAPTER 1

INTRODUCTION TO GROUP-III NITRIDES

1.1 CRYSTAL GROWTH OF GROUP-III NITRIDES

Growth of high quality crystalline GaN films is the prerequisite for any GaN-based device application. The growth of single crystal GaN was reported in 1969 by Maruska at RCA using hydride vapor phase epitaxy (HVPE).[1] HVPE growth uses a mixture of hot gaseous gallium chloride and ammonia to react in a temperature controlled quartz furnace, as the result, GaN film is deposited on a foreign substrate. The main drawback of HVPE is that its growth rate is as fast as hundreds of μm per hour, which makes it difficult to precisely control the thickness of nitride epilayer. For instance, a quantum well in the active region of a light emitting device is typically 3 nm in thickness, which is not readily achieved by HVPE growth. However, HVPE is an effective method to fabricate bulk GaN as a homogeneous substrate for subsequent epitaxy.

Alternatively, metal-organic vapor phase epitaxy (MOVPE) has been adopted for nitride growth where metal organic (e.g., trimethyl-gallium) gases and ammonia are used as reactants. MOVPE has an intermediate growth rate of ~2 μm/hr, and it is suitable for mass production because it can process several wafers per run. During the initial attempts of MOVPE growth of GaN, the film was composed of crystalline grains with sub-micron dimensions and the surface was rough. This problem was solved by using a low-temperature deposited buffer layer by Akasaki and Amano in 1986.[2] With this technique, crack free GaN films with flat surfaces were accomplished, while the electrical and optical properties were also improved. The mechanism of this optimized growth was understood in this way: after the deposition and heating of a buffer layer, a dense concentration of crystallites is formed. These crystallites serve as nucleation sites around

which the island growth of GaN begins. Then the small islands of GaN grow laterally and coalesce, resulting in a quasi-two-dimensional growth of GaN.

The optimum growth condition for GaN using MOVPE was well-established. Typically GaN is grown at 1000-1100 ^{o}C with a V/III ratio of thousands at near-atmospheric-pressure. The high temperature is used for promoting the crystallographic quality, while a large V-III ratio is due to the inefficient ammonia pyrolysis. Not only the growth of GaN but also of other group-III nitrides and their alloys such as InGaN and AlGaN is desirable for semiconductor device applications. In order to grow InGaN, the lower dissociation temperature of indium requires a lower growth temperature, but the cracking efficiency of ammonia drops with decreasing temperature, so that a higher V/III ratio is necessary. In addition, nitrogen is often substituted for hydrogen as carrier gas in order to prevent the formation of indium droplets. [3, 4] In order to grow AlGaN, higher temperatures and lower V/III ratios are used. A challenge is that the parasitic reaction between trimethyl-aluminum and ammonia often generates polymers that contaminate the reactor chamber and reduce the aluminum incorporation. [5] Reactor design was optimized to minimize this parasitic reaction, including innovations such as the use of a separate inlet for ammonia.

Besides HVPE and MOVPE, molecular beam epitaxy (MBE) is another technique for growing GaN. Elemental sources in ultra-pure gas form are directed toward a heated substrate under ultrahigh vacuum conditions (typically 10^{-5}-10^{-11} torr). The low pressure results in a long mean free path for the gaseous elements, hence they do not interact with each other but are transported as a "beam" and deposited on the substrate wafer. The growth rate of MBE is slow, less than 1 μm/hr, which enables a precise layer-by-layer growth process, hence abrupt interfaces. Another advantage of MBE growth is that the ultrahigh-vacuum environment allows real-time control of growth using in-situ

measurement techniques, such as reflection high-energy electron diffraction (RHEED); [6] hence the growth rate, the alloy composition and the strain relaxation during hetero-epitaxy can be monitored. However, MBE growth is not widely used for commercial applications because of the high expense for ultrahigh-vacuum apparatus, as well as long production time.

Of the above-mentioned growth techniques, one common problem is the choice of substrate materials. Since bulk GaN crystal is difficult to obtain in nature, foreign substrates are commonly used. An ideal substrate material for nitride epitaxial growth and device applications must satisfy the following requirements: 1. small lattice mismatch to the nitride epilayer, which guarantees a low extended defect density; 2. small thermal expansion mismatch to the nitride epilayer which prevents cracks and bowing of the wafer; 3. chemically robust during the epi-growth; 4. high thermal conductivity and stability for device operation. The most popular substrates are sapphire and SiC, whose properties will be discussed in detail in the next section.

1.2 PHYSICAL PROPERTIES OF GROUP-III NITRIDES

The electronegativity of nitrogen atom is much larger than other group-V elements. It leads to a higher ionicity of nitride semiconductors compared to the other III-V compounds. Crystal structures with high ionicity tend to have the wurtzite structure. [7] However, the zinc-blende and rock-salt structures have also been observed for GaN under special conditions.

Table 1.1 *Crystallographic data of wurtzite GaN, AlN, InN, and the favored substrates sapphire and 6H-SiC. [8]*

Properties	AlN	GaN	InN	Sapphire	6H-SiC
Lattice parameter, *a*	3.112	3.189	3.545	4.758	3.081
c	4.982	5.185	5.703	12.991	15.092
c/a	1.601	1.626	1.609	2.730	1.633 (×3)
Thermal expansion coefficient along *a*	4.2	5.6	5.7	7.5	4.2
Thermal expansion coefficient along *c*	5.3	3.2	3.7	8.5	4.7

The unit of lattice parameter is Angstrom and the unit of thermal expansion coefficient is 10^{-6} °C $^{-1}$.

The data in Tab. 1.1 are from experimental measurements of bulk material. For epitaxy, a small lattice mismatch and thermal expansion mismatch between substrate and epilayers is desired. From this point of view, 6H-SiC is more suitable than sapphire for nitride epitaxy, however, its price is more than 10 times of sapphire. Generally sapphire substrate is more favorable in industry.

When GaN is epitaxially grown on a sapphire substrate, the GaN cell conforms to a reduced periodic structure but not the unit cell of sapphire, as shown in Fig. 1.1. The solid and empty circles represent Al atom and vacancy of sapphire, respectively, with a density ratio of 2:1. The reduced periodic structure is marked with dash lines and the unit cell is marked with solid lines. The gray circles represent Ga/N atom of GaN epilayer. From this figure it can be found that there is a 30° rotation between unit cell of sapphire and GaN, in other words, GaN $[11\bar{2}0]$ axis is aligned with sapphire $[1\bar{1}00]$axis while

GaN $[1\bar{1}00]$ axis is aligned with sapphire $[11\bar{2}0]$ axis. This phenomenon appears because this topological setup reduces the lattice mismatch from 33% to 16%, which favors the pseudomorphic growth.

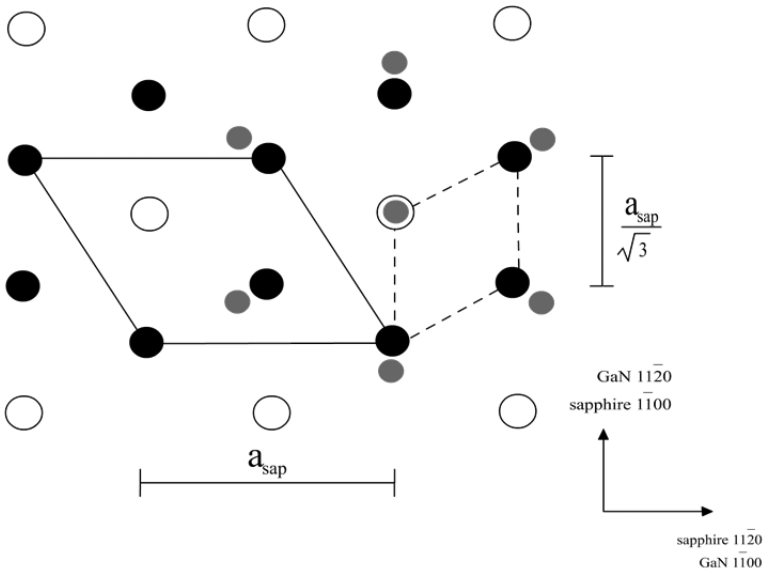

Fig.1.1. Crystallographic alignment of epitaxial *c*-oriented GaN grown on *c*-oriented sapphire substrate.

It is interesting to notice that the *c/a* ratio of the III-nitride semiconductors is smaller than the ideal value for tetrahedron ($\sqrt{8/3} \approx 1.633$). This deviation leads to a displacement between cation and anion's centers, hence a net dipole moment along *c*-axis in wurtzite nitrides. The magnitude of this displacement can be estimated with a very simple model: taking one tetrahedron building block with four N atoms at the corner and one metal atom in the center of the specific tetrahedron, as shown in Fig. 1.2, the net force applying on the metal atom must vanish at mechanical equilibrium. Assuming that all the forces acting on point charges are Coulombic type, the distance between the top N atom and central metal atom (the bond length along the *c*-axis) can be calculated in units of *c*, usually defined as an internal parameter *u*, by the following equation:

$$\frac{3(\frac{1}{2}-u)c}{[\frac{a^2}{3}+(\frac{1}{2}-u)^2c^2]^{\frac{3}{2}}}=\frac{1}{u^2c^2} \tag{1.1}$$

The net dipole moment in the tetrahedron is *Ze(u-0.375)c*, where *Z* is the effective charge of the metal atom. The net dipole moment per unit volume is the polarization, in this case of unstrained material, called spontaneous polarization which is equal to $\frac{Ze(u-0.375)}{\sqrt{3}a^2/24}$. Using the value of *a* and *c* of GaN in Tab.1.1 and $Z \approx 3$ for Ga, it is obtained that the spontaneous polarization of GaN is -0.0285 C/m^2. The negative sign means that for Ga polarity, the spontaneous polarization is directing downward, to the *-c* direction. The model used here gives a value close to the first-principle calculation result of -0.029 C/m^2 by Bernardini. [9] The simple model proposed here provides us the basic ideas about spontaneous polarization, including its direction, magnitude, and how it is related with the lattice parameters.

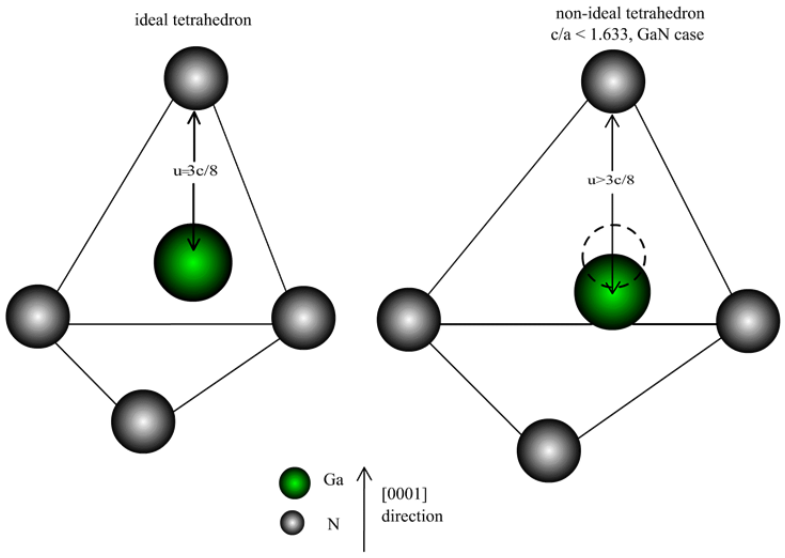

Fig.1.2. Illustration of spontaneous polarization from non-ideal *c/a* ratio of GaN tetrahedron. The Ga-N bond along the *c*-axis is larger than 3*c*/8 according to the mechanical equilibrium, which results in a net dipole along the $[000\bar{1}]$ direction.

To consider GaN with the zinc-blende structure, an equivalent lattice constant of wurtzite is defined so as to make the volume per atom for wurtzite and zinc-blende structures are identical:

$$\frac{1}{12}\frac{3\sqrt{3}}{2}a_{wz}^2 c_{wz} = \frac{1}{8}a_{zb}^3 \text{, therefore, } a_{zb} = (\sqrt{3}a_{wz}^2 c_{wz})^{1/3}. \quad (1.2)$$

From the wurtzite GaN lattice constant in Table 1.1, the equivalent lattice constant for zinc-blende GaN is 0.4503 nm, which is close to the experimental data 0.449 nm of zinc-blende GaN. [10] The corresponding Ga-N bond length is 0.1950 nm in the zinc-blende structure, which is close to the summation of tetrahedral radii of Ga and N (0.196 nm) according to Pauling. [11]

For ternary alloys such as AlGaN, InGaN and InAlN, the lattice constant follows Vegard's law:

$$a(A_x B_{1-x} N) = x \cdot a(AN) + (1-x) \cdot a(BN) \quad (1.3)$$

In terms of band structure, the nitride semiconductors have a direct band gap, which cover the full range of the visible spectrum. These properties guarantee their application in optoelectronic devices. The band gaps of AlN, GaN, and InN at room temperature are 6.25, 3.51 and 0.78 eV, respectively. For ternary alloys, a bowing parameter is used to approximately describe their band gap:

$$E_g(A_x B_{1-x} N) = xE_g(AN) + (1-x)E_g(BN) - bx(1-x) \quad (1.4)$$

The recommended bowing parameters of AlGaN, InGaN, InAlN are 0.7, 1.4 and 2.5 eV, respectively. [12] The band gap can be plotted as a function of equivalent bond length for those alloys according to equation (1.2), (1.3) and (1.4), as shown in Fig. 1.3.

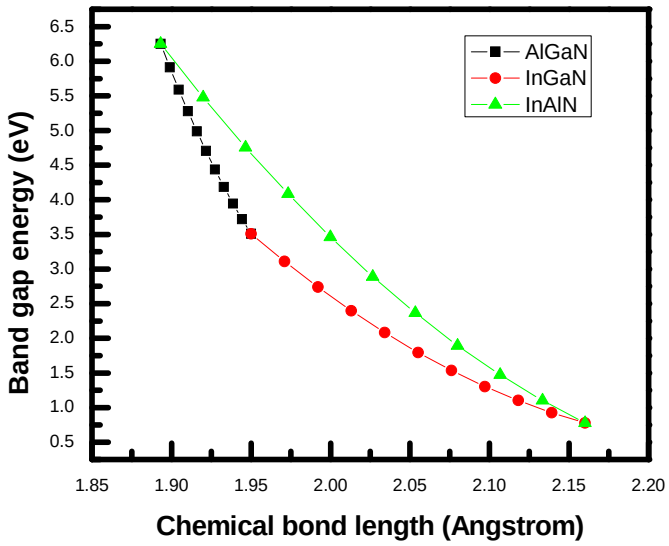

Fig.1.3. Band gap as a function of chemical bond length of AlGaN, InGaN, and InAlN alloys. The adjacent points in the curve refer to 10% composition difference.

1.3 DEVICE APPLICATIONS OF GROUP-III NITRIDES

For semiconductor device applications, n-type and p-type doping is of great importance. Si and Mg are commonly used as dopant and acceptor due to their relatively low activation energy. During the early years, p-type GaN was believed to be impossible to achieve due to self-compensation from residual donors. It means that GaN films have a tendency towards an intrinsic donor concentration of $10^{19}/cm^3$ or higher even without intentionally doping. The most likely intrinsic donor is nitrogen vacancy due to the high growth temperature and high nitrogen volatility. [1, 13] However, with the application of low-temperature buffer layer techniques, the intrinsic impurities are reduced to be less than $10^{17}/cm^3$, resulting in the possibility of high level of p-doping. [2, 14]

A breakthrough for GaN-based semiconductor devices was made by Akasaki and Amano in 1989 when p-type conducting GaN was achieved using low energy electrons beam irradiation (LEEBI) on the as-grown Mg-doped GaN. [15] The Mg was mostly

passivated by hydrogen from the carrier gas during growth, while the LEEBI treatment broke up the Mg-H complex and rendered Mg into an active dopant. Despite a successful achievement of p-conductivity, LEEBI requires a scanning over the whole wafer, which is time-consuming, and the penetration depth of the electron beam is limited. It was later found by Nakamura in 1991 that thermal annealing at temperatures up to 1000 ^{o}C under hydrogen-free atmosphere provided p-type conducting GaN as well.[16] Thermal annealing is a faster, easier way for mass production of p-type GaN than LEEBI.

After the realization of p-type GaN, it becomes possible to grow GaN-based light emitting diodes (LED). An LED consists of a p-n junction such that when a forward bias is applied the electrons and holes are injected toward the junction and recombine with each other. Ideally, each injected electron-hole pair generates one photon with energy of band gap of the junction material. A GaN p-n junction LED was first reported by Akasaki and Amano in 1989.[17] In the 1990s, Nakamura at Nichia developed a two-flow MOCVD reactor and introduced a thermal annealing method for p-type GaN. Nichia also optimized the growth of InGaN layer as the active region in LEDs. In 1993, Nichia announced commercial blue InGaN-based LEDs. With the advances in technology for crystal growth, device processing and packaging, nowadays high-brightness and high-efficiency nitride LEDs with reasonable prices are produced by many companies, such as Nichia, Osram, Lumileds, and Cree.

Although the luminous efficiency of the GaN-based LED is ~ 100 to 200 lm/W at the present time, which is one order of magnitude higher than standard incandescent light bulb, there still is much space left for improvement of LED performance. One critical factor that limits the efficiency is the polarization effect. As discussed in Sec. 1.2, nitride materials have large spontaneous and piezoelectric polarizations, resulting in strong internal fields in the active region. In order to increase the carrier density for

recombination in the active region, thin quantum wells are typically used. A 3 nm-thick InGaN quantum well with polarization field is taken into account for the calculation of the band diagram and eigen states for electrons and holes in Fig. 1. 4. The band edge difference is intentionally large (a reduced band gap for InGaN) for a better visualization of the results.

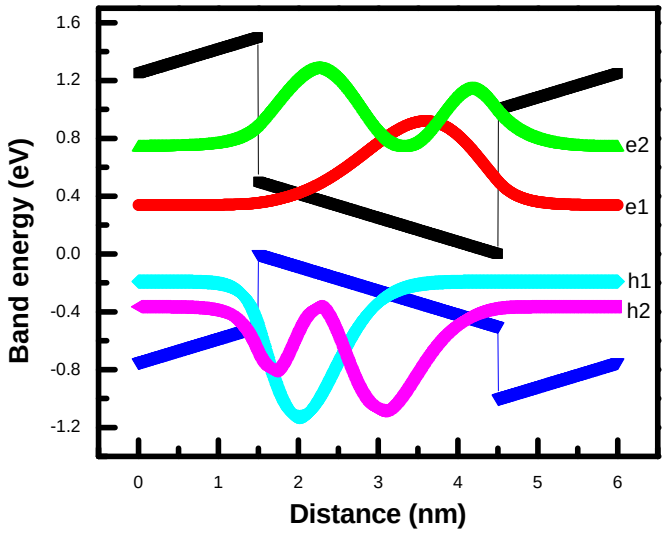

Fig.1.4. Electron and hole distribution in a 3 nm-thick $In_{0.08}Ga_{0.92}N$ quantum well with polarization field of 1.7 MV/cm.

In Fig. 1.4, the polarization field is calculated from the indium composition, which will be discussed in detail in Chapt. 3. The probability distributions for the ground state and the first excited state for electrons and holes are shown. The ground level of each state indicates the corresponding eigen-energy. The electrons and holes are localized toward opposite sides in the quantum well.

According to Fermi's golden rule, the radiative recombination rate is proportional to the overlap of electron and hole wave functions: $\int \varphi_e \varphi_h dz$. The calculated overlap is shown in Fig. 1.5. The ground state energy $E_{e1}+E_{h1}$, where the

conduction band edge and valence band edge are taken as zero energy point for electron and holes, respectively, is also shown. Both of them are calculated as a function of piezoelectric field, which is normalized to the unscreened maximum field of 1.7 MV/cm. This figure reflects the quantum-confined Stark effect, which includes two aspects: 1. The overlap between electron and hole wave function decreases. 2. The emission energy decreases. The former results in a low efficiency, the latter leads to the unstable emission wavelength, both are detrimental to LED performance. A promising technique to solve this problem is to use non-*c*-plane for growth, which will minimize or diminish the polarization field along the growth direction. The crystal orientation dependence of polarization field will be discussed in Chapt. 3.

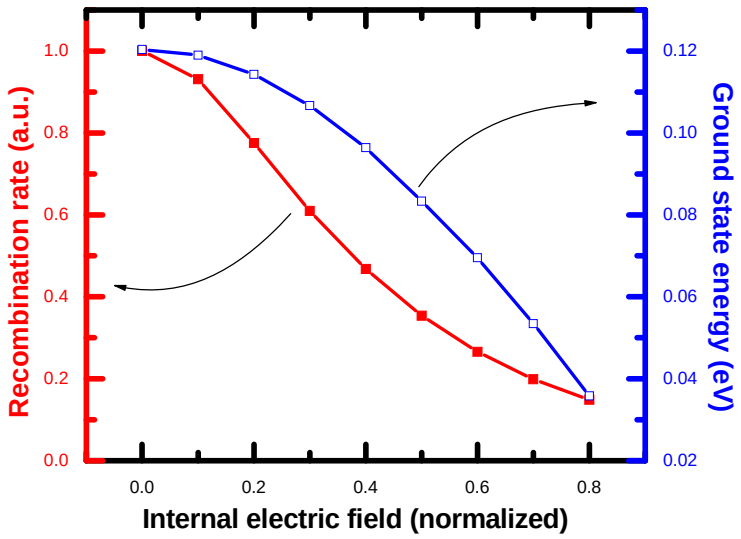

Fig.1.5. Electron and hole radiative recombination rate and ground state energy as a function of normalized internal electric field in a 3 nm-thick InGaN quantum well.

Another challenge that limits the LED performance is the efficiency droop. High-power LED usually works with current density higher than 10 A/cm^2, and its efficiency decrease drastically in that current range. [18] A possible reason for efficiency droop is

strong Auger recombination for nitrides. The internal quantum efficiency is determined by three different recombination processes: 1. Shockley-Read-Hall (SRH) recombination, by which carriers recombine non-radiatively at crystal defects. One carrier (either electron or hole) is involved for each SRH recombination therefore the recombination rate is A·n, where A is called the SRH parameter and n is the injected carrier density. 2. Radiative recombination, by which one electron and one hole recombine with each other and emit a photon. The radiative recombination rate is $B \cdot n^2$ where B is the radiative coefficient. 3. Auger recombination, by which the energy from recombination of electron and hole does not convert into photon energy, but excites another electron in the conduction band to a higher energy state. The Auger recombination rate is $C \cdot n^3$ since three particles are involved, where C is the Auger parameter.

The internal quantum efficiency is defined as the ratio of number of photons emitted to number of carriers injected into the active region. Therefore it can be expressed by the A, B, and C coefficients by:

$$\eta_{IQE} = \frac{Bn^2}{An + Bn^2 + Cn^3}\ , \tag{1.5}$$

The injected carrier density can be converted into current density by:

$$J = \frac{nqd}{\tau} \approx qd(An + Bn^2 + Cn^3)\,, \tag{1.6}$$

where d is the active region thickness and τ is the carrier lifetime.

The internal quantum efficiency can be calculated as a function of the injected current density according to Equations 1.5 and 1.6, as shown in Fig. 1.6.

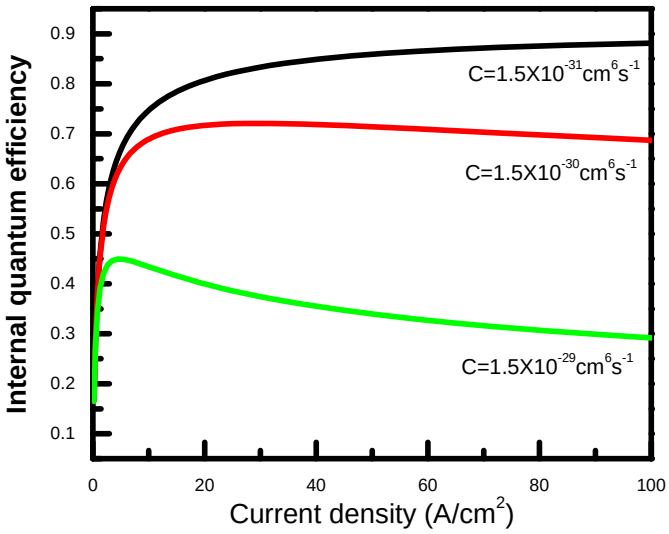

Fig.1.6. Internal quantum efficiency droop with increasing current density.

The SRH parameter A and the radiative coefficient B are $1.0\times10^{7}\mathrm{s}^{-1}$ and $2.0\times10^{-11}\mathrm{cm}^{3}\mathrm{s}^{-1}$, respectively, using values from the literature. [19] The Auger parameter C has values $1.5\times10^{-31}\mathrm{cm}^{6}\mathrm{s}^{-1}$, $1.5\times10^{-30}\mathrm{cm}^{6}\mathrm{s}^{-1}$, $1.5\times10^{-29}\mathrm{cm}^{6}\mathrm{s}^{-1}$, which cover the full range of values in the literature. The stronger the Auger recombination, the more significant efficiency droop appears.

It is also argued that efficiency droop is related with device structure, specially the design of electron-block-layer, which leads to the problem of electron overflow. [18] It is still of debate what is the main reason for the efficiency droop and how to alleviate it. A possible method is to increase the active region thickness, hence reduce the effective volume carrier density. However, when active region goes thicker, its material quality could degrade, as well as the QCSE is more serious. Non-polar growth on free-standing GaN is desired for growing thick active regions in LEDs.

Based on the success of GaN-based LEDs, laser diodes (LDs) have been developed and commercialized. The main difference in the epitaxial structure of LED and LD is that LD requires thick cladding layers and waveguides to confine the light emitted

from the active region. The light guiding is achieved by using AlGaN layers because their refractive indices are lower than that of InGaN in the active region, while they have larger band gap than InGaN which prevents the light to be absorbed out of the active region. A schematic structure of GaN-based laser diode is shown in Fig. 1.7. The carrier confinement is illustrated in the band diagram, while the optical confinement is achieved by design of the refractive index of the layers.

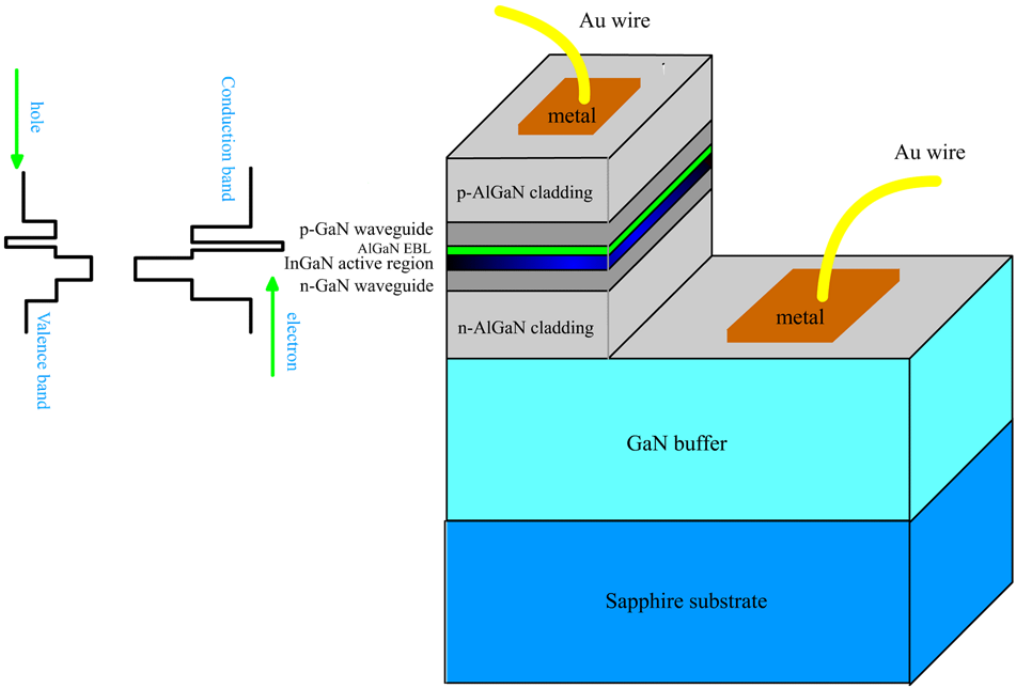

Fig.1.7. Schematic structure of a GaN-based laser diode. The device structure is shown on the right and the band diagram of the active region is shown on the left.

Laser actions require three conditions: 1. There must be a gain medium, which is the InGaN active layer in Fig. 1.7. With high injection current, the population inversion (the probability of finding electrons in the conduction band is higher than in the valence band) must be achieved, which makes stimulated emission overwhelm light absorption. 2. There must be a resonant cavity in order to provide optical feedback, which is achieved by cleaving two parallel $[1\bar{1}00]$ mirror planes. 3. The optical gain must exceed the total absorption loss, which requires a high material quality to minimize defect and impurity

scattering, as well as a high-reflection coating on the cleavage planes to reduce the cavity loss.

Besides the optoelectronic application, GaN is also attractive for electronic devices. One example is the high-electron-mobility transistor (HEMT). Conventionally, the epitaxial structure of HEMTs consists of a modulation-doped heterostructure, in which the layer with wider band gap is doped while the layer with narrower band gap is undoped. The mobile electrons (holes) will be accumulated in the undoped, narrow-gap layer within several nm of the interface, which are called 2-dimensional electron gas (2DEG) or 2-dimensional hole gas (2DHG). Due to the spatial separation from impurities, these free carriers have high mobility, as well as high sheet concentration. For AlGaN/GaN HEMTs, the strong spontaneous and piezoelectric polarization introduce extra interface charges, which result in a better accumulation of the 2DEG or 2DHG. [20] The corresponding band diagram is shown in Fig. 1.8.

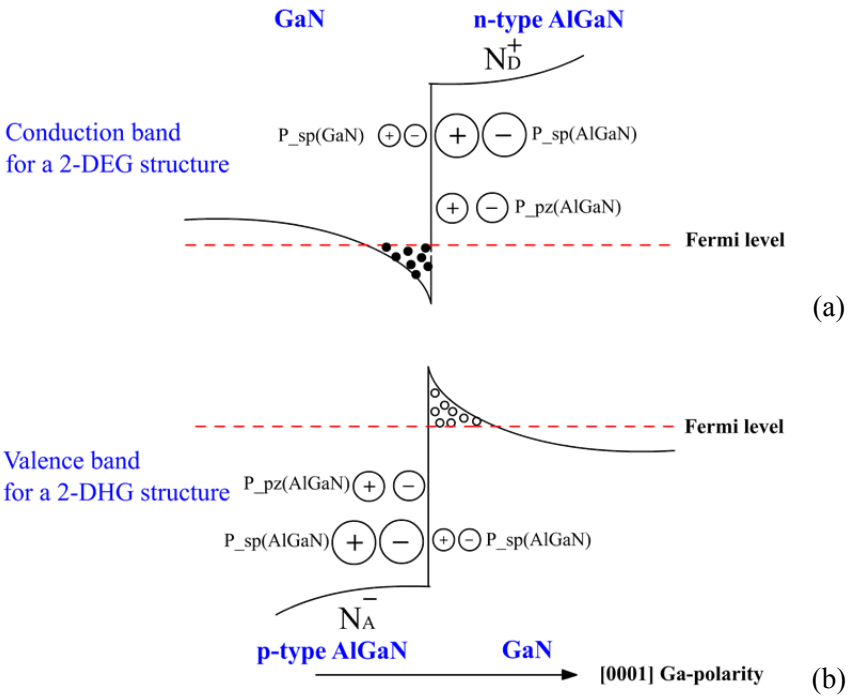

Fig.1.8. Band diagrams of AlGaN/GaN heterostructures for 2DEG and 2DHG. (a) Conduction band of 2DEG structure, the spontaneous and piezoelectric dipoles results in a positive charge on the interface, which enhances the accumulation of electrons. (b) Valence band of 2DHG structure, the spontaneous and piezoelectric dipoles results in a negative charge on the interface, which enhances the accumulation of holes.

1.4 LAYEROUT OF THIS DISSERTATION

This dissertation investigates the polarization effects in group-III nitrides on both theoretical and experimental sides.

In Chapter 2, experimental techniques for studying III-nitride materials and devices are reviewed. The principle of diffraction contrast, micro-diffraction and high-resolution imaging and electron holography in transmission electron microscopy (TEM) are introduced, and examples of their application on III-nitride are presented. The practical issues for characterizing nitride material using TEM are discussed. This chapter provides a guide for people studying the nitride using TEM.

In Chapter 3, piezoelectric and spontaneous polarizations are calculated for different growth planes. The model for strain calculation is based on Romanov's pioneer

work, [21] while the in-plane polarization component is first time revealed in my results. Since typical nitride heterostructure grown on non-polar and semi-polar planes deviate from perfect planar structures, the in-plane polarization leads to a significant electrostatic potential variation, which is sensitive to the lateral characteristic dimension determined by the microstructure. Those results indicate that specific semi-polar plane growth is preferred in terms of reducing quantum-confined Stark effect in light emitting devices.

Based on the polarization calculation of Chapter 3, Chapter 4 describes band diagram calculation under the polarization effect, by the self-consistently solving Schrödinger and Poisson equation. The electrostatic potential profiles measured by electron holography in the following chapters are compared with the calculations using the solver introduced in this chapter. Calculation also shows that the self-screening of polarization field appears beyond the critical composition or thickness. In addition, new active region design under the polar-plane growth, including the Si-doped barrier and triangular quantum wells are proposed.

Polarization fields enhance the accumulation of free carriers in heterojunctions. In Chapter 5, the electronic band structure of a modulation-doped *p*-type AlGaN/AlN/GaN heterostructure, where the AlGaN layer is compositionally graded, is studied by electron holography. The epilayer is grown along wurtzite (0001) plane, therefore strong polarizations are presented. The electrostatic potential profile and the two-dimensional hole gas (2DHG) distribution are measured with high spatial resolution across the heterostructure. A positive curvature in the potential profile is observed, and it is considered as evidence for the accumulation of holes in a 2DHG at the AlN/GaN interface. It is also observed that the potential barrier for the 2DHG is greatly affected by acceptor ionization in the *p*-AlGaN layer. This knowledge of nature of the energy barriers for hole transfer between adjacent channels is important in the optimization of vertical

conductivity of *p*-type AlGaN/GaN heterostructures, which can be used as current spreading layers in GaN-based light emitting diodes or laser diodes.

In order to better understand how the polarization charges affect the free carrier accumulation, Chapter 6 studies cubic $Al_{0.3}Ga_{0.7}N$/GaN heterostructures grown by plasma-assisted molecular beam epitaxy on 3C-SiC (001) substrates, which has zero spontaneous and piezoelecitrc polarization due to higher crystal symmetry. A profile of the electrostatic potential across the cubic-AlGaN/GaN heterojunction is obtained using electron holography in the transmission electron microscope. The experimental potential profile indicates that the unintentionally doped layers show n-type behavior and accumulation of free electrons at the interface with a density of $5.1 \times 10^{11}/cm^2$, about one order of magnitude less than in wurtzite AlGaN/GaN junctions. A combination of electron holography and cathodoluminescence measurements yields a conduction-to-valence band offset ratio of 5:1 for the cubic AlGaN/GaN interface, which also promotes the electron accumulation. Band diagram simulations show that the donor states in the AlGaN layer provide the positive charges that to a great extent balance the two-dimensional electron gas.

InAlN is a group-III nitride alloy which can be grown lattice-matched to GaN, hence has zero piezoelectric polarization. In Chapter 7, the $In_xAl_{1-x}N$/GaN system is found to show compositional instability at the lattice-matched composition (x=0.18) in epitaxial layers grown by metal organic chemical vapor deposition. The breakdown in compositional homogeneity is triggered by threading dislocations, propagating from the GaN underlayer, with a screw component, and which tend to open up into V-grooves at a certain thickness of the $In_xAl_{1-x}N$ layer. The V-grooves coalesce and are filled with material that exhibits a significant drop in indium content and a broad luminescence peak.

TEM observations suggest that the structural breakdown is due to heterogeneous nucleation and growth at the facets of the V-grooves.

In Chapter 8, the main findings of this dissertation are summarized and future work is suggested.

REFERENCES

[1] M. P. Maruska and J. J. Tietjen, Appl. Phys. Lett. **15**, 327 (1969).

[2] H. Amano, N. Sawaki, I. Akasaki, and Y. Toyoda, Appl. Phys. Lett. **48**, 353 (1986).

[3] S. Nakamura and T. Mukai, Jpn. J. Appl. Phys. **31**, L1457 (1992).

[4] F. Scholz, V. Harle, F. Streuber, H. Bolay, A. Edornen, B. Kaufmann, V. Syganow, and A. Hangleiter, J. Cryst. Growth. **170**, 321 (1997).

[5] C. H. Chen, H. Liu, D. Steigerwald, W. Imler, C. P. Kuo, M. G. Craford, M. Ludowise, S. Lester, and J. Amano, J. Electron. Mat. **25**, 1004 (1996).

[6] A. Y. Cho, Surf. Sci. **17**, 494 (1969).

[7] J. C. Phillips, *Bonds and Bands in Semiconductors*, Academic, New York, (1973).

[8] B. Gil, *Low-dimensional nitride semiconductors*, Oxford Univ. Press, Oxford, (2002).

[9] T. Lei, M. Fanciulli, R. J. Molnar, T. D. Moustakas, R. J. Graham, and J. Scanlon, Appl. Phys. Lett. **59**, 944 (1991).

[10] F. Bernardini, and V. Friorentini, Phys. Rev. B. **56**. R10024 (1997).

[11] L. Pauling, *The nature of the chemical bond*, Chapter 4, Cornell Univ. Press, New York, (1960).

[12] I. Vurgaftman and J. R. Meyer, J. Appl. Phys. **94**, 3675 (2003).

[13] M. Ilegems and H. C. Montgomery, J. Phy. Chem. Solids. **34**, 885 (1973).

[14] S. Nakamura, Jpn. J. Appl. Phys. **30**, L1705 (1991).

[15] H. Amano, M. Kito, K. Hiramatsu, and I. Akasaki, Jpn. J. Appl. Phys. **28**, L2112 (1989).

[16] S. Nakamura, M. Senoh, and T. Mukai, Jpn. J. Appl. Phys. **30**, L1708 (1991).

[17] I. Akasaki, H. Amano, Y. Koide, K. Hiramatsu, and N. S. Sawaki, J. Cryst. Growth. **98**, 209 (1989).

[18] M. H. Kim, M. F. Schubert, Q. Dai, J. K. Kim, and E. F. Schubert, Appl. Phys. Lett. **91**, 183507 (2007).

[19] M. Zhang, P. Bhattacharya, J. Singh, and J. Hinckley, Appl. Phys. Lett. **95**, 201108 (2009).

[20] O. Ambacher, J. Majewski, C. Miskys, A. Link, M. Hermann, M. Eickhoff, M. Stutzmann, F. Bernardini, V. Fiorentini, V. Tilak, B. Schaff, and L. Eastman, J. Phys.: Condens. Matter **14**, 3399 (2002).

[21] A. E. Romanov, T. J. Baker, S. Nakamura, and J. Speck, J. Appl. Phys. **100**, 023522 (2006).

CHAPTER 2

EXPERIMENTAL TECHNIQUES

2.1 TRANSMISSION ELECTRON MICROSCOPY

All material properties can be traced back to the type of atoms, atomic configuration, and their arrangement into microstructures. Transmission electron microscopy (TEM) is a powerful technique for material characterization, especially for microstructural features. It has been developed since the 1930s and uses a high energy electron beam for imaging. Typically a 200 kV electron beam corresponding to a wavelength of 2.51 pm can provide near-atomic resolution (a few angstrom). With a correction of the lens system, nowadays the TEM resolution can be pushed into the sub-angstrom regime [1, 2]. One problem of TEM is that it requires a very thin specimen for observation due to relatively strong electron scattering within the material, hence only providing some "representative" features, and the real 3D microstructures exhibit themselves as 2D projected images viewed in transmission. Despite these limitations, TEM is still unrivaled among the material characterization tools because of its ability of direct observation of microstructures.

Three sub-areas of TEM techniques are of great importance for studying the microstructure of crystalline specimens, in our case, group-III nitrides: (a) electron diffraction, (b) diffraction contrast technique, and (c) high-resolution (HR) imaging. In addition, electron holography (EH) in the TEM is a technique to investigate the electric and magnetic fields in the material, which is particularly useful for GaN which exhibits strong polarization fields. Those techniques are the main characterization tools in my research and they will be introduced in this chapter.

Crystals can be investigated in reciprocal space by analysis of the diffraction pattern (DP). For the wurtzite GaN (the most common phase), the structure factor of a unit cell for (*hkml*) diffraction is:

$$F = (f_{Ga} + f_N e^{2\pi i u l})(1 + e^{2\pi i(\frac{1}{3}h + \frac{2}{3}k + \frac{1}{2}l)}) \tag{2.1}$$

where u is the internal parameter that approximately equals to 3/8. The extinction condition is $h + 2k = 3n$ and l is odd, for example, (0001) diffraction is forbidden under the kinematical condition. However, (0001) diffraction is often dynamically excited in the $[11\bar{2}0]$ zone axis, which is shown in Fig.2. 1. This can be simply understood as double diffraction from allowed $(1\bar{1}00)$ and $(\bar{1}101)$ planes.

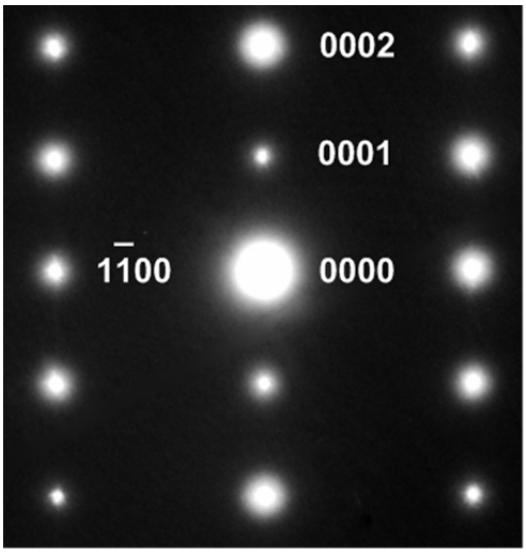

Fig. 2.1. A typical diffraction pattern of GaN along the $[11\bar{2}0]$ zone axis. The (0001) diffraction spot is visible but weaker, and it can be understood as the result of double diffraction.

On the contrary, the (0001) spot can never be excited by dynamic diffraction under $[1\bar{1}00]$ zone because it cannot be acquired by superposition of the allowed diffraction with this zone. But sub-spots between (0000) and (0002) can also be produced by atomic ordering or superlattice diffraction.[3,4] In order to prevent this ambiguity, the electron diffraction study is usually favored to be performed under the $[1\bar{1}00]$ zone axis.

One example of diffraction pattern under the [$1\bar{1}00$] zone axis is shown in Fig.2.2. The sample studied is an AlGaN/GaN long-period superlattice grown on GaN underlayer. (a) and (b) correspond to diffraction patterns from the GaN underlayer and the AlGaN/GaN superlattice, respectively. No dynamically excited diffraction spot exists in (a). The superlattice spots in (b) indicate good periodicity, while the superlattice periodicity can be internally calibrated by the materials' lattice spacing in the DP.

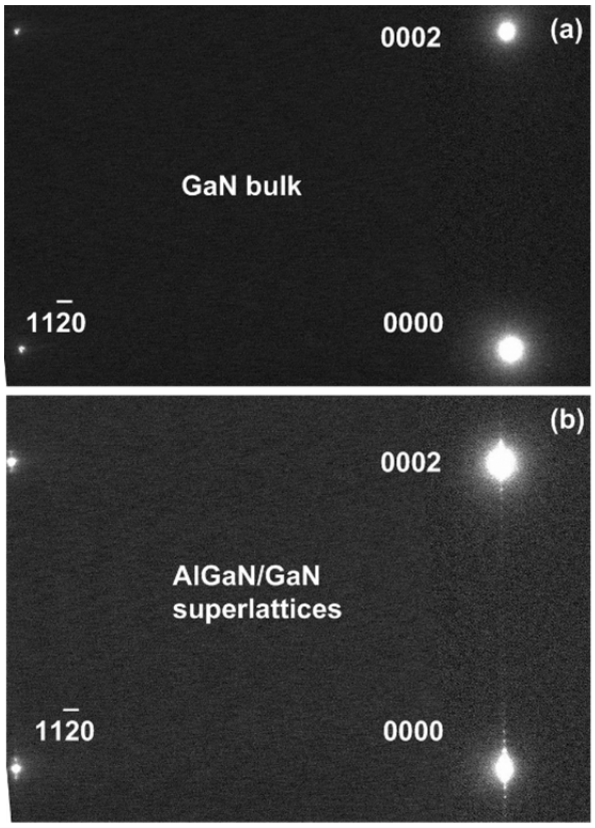

Fig. 2.2. Diffraction patterns of (a) a GaN underlayer and (b) an AlGaN/GaN superlattice taken along the <$1\bar{1}00$> zone axis. A long camera length is used for improved resolution of the superlattice spots.

Another example of electron diffraction of GaN is convergent beam electron diffraction (CBED) which is used to determine the polarity and specimen thickness. GaN

as a polar crystal lacks a center of symmetry, but this is not reflected by conventional electron diffraction in which the (0002) and $(000\bar{2})$ spots appear identical. In order to investigate the polarity, the CBED technique is used. Electron diffraction with parallel illumination gives sharp spots on the back focal plane, while diffraction with convergent beam illumination produces diffraction disks with a wealth of contrast detail. These details can be simulated using dynamic diffraction theory, which involves multiple scattering events of the electron wave as it travels through the sample, so that the resulting disk patterns depend on the crystal polarity and thickness. [5] Figure 2.3 shows an example of simulated and experimental CBED pattern of a standard GaN film grown by MOCVD.

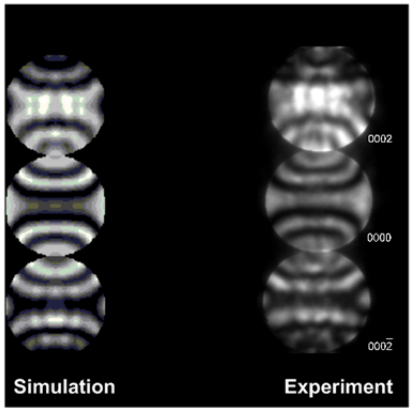

Fig. 2.3. Simulated and experimental CBED patterns of GaN along the $[11\bar{2}0]$ zone axis.

In Fig. 2.3, the asymmetry of (0002) and $(000\bar{2})$ disks can be clearly seen. A thickness of 140 nm is used in simulation to achieve the best match. The change of CBED pattern can be recognized within 10 nm of thickness variation, giving an error bar of $\pm$ 5 nm. In addition, by comparing the CBED pattern and shadow image of specimen, it can be found that the studied film has a Ga-terminated polarity.

Based on the diffraction conditions, another TEM technique called diffraction contrast is commonly used particularly in the investigation of crystal defects. The most

common defects of group-III nitride that are observable in TEM are dislocations, stacking faults, grain boundaries, and precipitates. Every defect can be characterized as a local displacement off the perfect crystal atom positions. The amplitude of diffracted wave is sensitive to the displacement vector Δr and to the deviation parameter s (s indicates how much the diffraction vector is away from exact Bragg condition:$\Delta k=g$):

$$\psi_g \propto \sum_r f(r)e^{2\pi i\Delta kr} = \sum_r f(r)e^{2\pi i(g-s)(R+\Delta r)} \approx \sum_r f(r)e^{2\pi i(-sr+g\Delta r)} \qquad (2.2)$$

By comparing the defected region and perfect crystal region, a phase difference of $g\cdot\Delta r$ can be found and this difference determines the image contrast at the defect. The defects have null contrast when $g\cdot\Delta r=0$. Table 2.1 lists the displacement vectors for dislocations and stacking faults in GaN, and their visibility criterion:

Table 2.1. *The most common types of defects in GaN and their characteristics.*

Defect type	Displacement vector	Visible under $g=<11\bar{2}0>$?	Visible under $g=<1\bar{1}00>$?	Visible under $g=<0002>$?
Edge dislocation	$\propto \frac{1}{3}<11\bar{2}0>$	Yes	No	No
Screw dislocation	$\propto<0001>$	No	No	Yes
Mixed dislocation	$\propto \frac{1}{3}<11\bar{2}3>$	Yes	No	Yes
I_1 BSF	$\frac{1}{6}<2\bar{2}03>$	No	Yes	No
I_2 BSF	$\frac{1}{3}<1\bar{1}00>$	No	Yes	No
E BSF	$\frac{1}{2}<0001>$	No	No	No

This table indicates that when studying edge, screw and mixed dislocations, TEM specimen should be thinned and observed along <$1\bar{1}00$> projection and using g=<$11\bar{2}0$> and g=<0002>. On the other hand, <$11\bar{2}0$> projection and g=<$1\bar{1}00$> is the proper condition to study stacking faults. That is also because the ABAB... sequence can only be observed under g=<$11\bar{2}0$> zone axis. In addition, the visible criterion for the I1 BSF and the I2 BSF are identical for the g vectors listed in the table. In order to distinguish them, a dynamically excited spot such as g=<0001> or g=<$3\bar{3}03$> is needed.[6] Extrinsic SFs are not visible under g vectors listed in the table. To visualize them, g=<$1\bar{1}01$> should be used.

For an improved visualization of dislocations, a more delicate operation in the diffraction contrast techniques is necessary. Weak-beam dark-field (WB-DF) microscopy is often adopted for producing sharp dislocation lines in the image. The diffraction contrast depends on the deviation parameter s. The exact Bragg condition (s=0) is poor for imaging dislocations since diffraction contrast will be shown over a large area with a crystal plane distortion close to the dislocation core, leading to a wide and fuzzy image of the dislocation. [7] A positive deviation vector is desired under which the diffraction contrast will be asymmetric around the dislocation core, and the darker contrast side in the dark-field image is indistinguishable with the background intensity. Therefore, the dislocations will appear as sharp bright lines in the weak-beam dark-field images. In practice, a g-3g condition is often used, which is illustrated in Fig. 2.4.

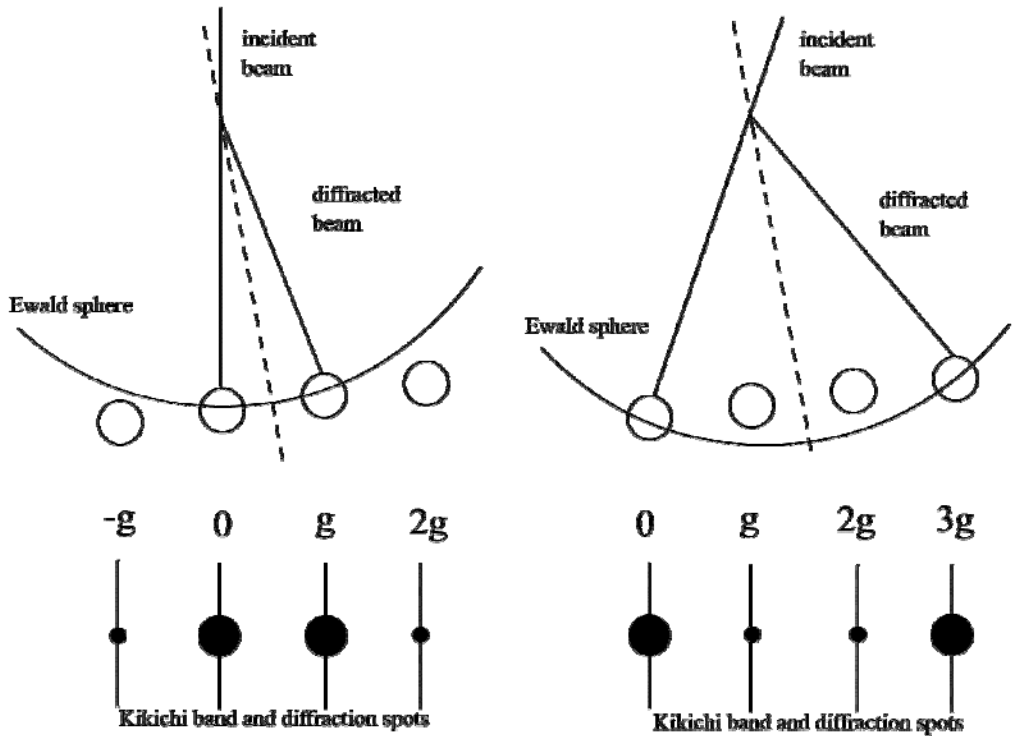

Fig. 2.4. Schematic diagram of *g*-3*g* condition in WBDF. The vertical direction is the optic axis in the TEM, the dash line represents the diffraction plane.

First the specimen is tilted close to a two-beam condition, where the g diffraction spot is strongly excited, as shown in the left part of Fig. 2.4. Then the DF beam-deflection coils are used to change the direction of incident beam, which is equivalent to rotating the Ewald sphere in reciprocal space. The 3g reflection spot is strongly excited while the g reflection spot on the optic axis becomes weak, as shown in the right part of Fig. 2.4. The Kikuchi band is fixed to the specimen so that it can be taken as a reference for checking the *g*-3*g* condition.

One limitation of the diffraction contrast technique is that the position of the dislocation image is not exactly the real position of dislocation core, because this contrast is rather a result of the variation of orientation of crystal planes around the defects. In order to directly study the microstructural nature of defects, more important, the atomic configuration of the material, high-resolution TEM (HRTEM) technique is indispensable.

The general purpose of using HRTEM is to obtain an image with atomic resolution. The actual resolution is mainly limited by the characteristics of the microscope lens. When the incident beam passes through the specimen, the wave function at the exit plane is determined by the atomic potential. This electron wave at the specimen exit surface is the object of the microscope. During the following imaging process, the phase of the electron wave is distorted by spherical aberration and defocus of the objective lens, which can be described by the phase contrast transfer function. In other word, the object is smeared out by the imperfection of objective lens. To overcome this obstacle, a series of images needs to be acquired with different defocus values, then the image series has to be compared with a simulated series, and finally one of the images whose spatial intensity distribution fits best with the proposed atomic structure is chosen. In HRTEM, the specimen has to be tilted and viewed edge-on along low-index crystallographic directions to determine the atomic structure. For the most common wurtzite GaN cross-section sample, the $[11\bar{2}0]$ zone axis is more suitable than the $[1\bar{1}00]$ one since the AB stacking sequence can be observed and the lateral lattice spacing is larger than the one under $[1\bar{1}00]$ zone. Figure 2.5 shows the ideal atomic configuration of GaN along $[11\bar{2}0]$ zone. Figure 2.6 shows a realistic HRTEM image of GaN along $[11\bar{2}0]$ zone.

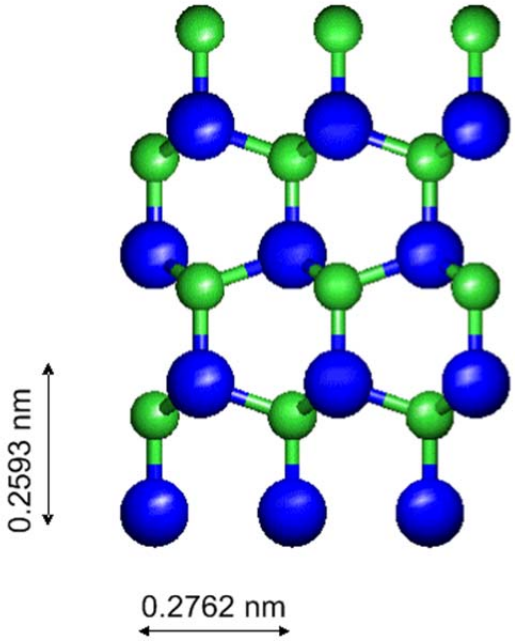

Fig. 2.5. Atomic configuration of GaN along the $[11\bar{2}0]$ zone axis. Blue balls represent Ga atoms and green ones represent N atoms. The characteristic dimensions resolvable in HRTEM are indicated.

Fig. 2.6. HRTEM image of GaN along the $[11\bar{2}0]$ zone axis. The atomic configuration matches well with the ball-and-stick model in Fig. 2.5.

2.2 ELECTRON HOLOGRAPHY

Although HRTEM is a powerful technique for studying the atomic arrangement, its resolution is still far from the requirement to examine the polarization effect that

requires resolution and identification of the individual Ga and N atoms. From previous discussion in Section 1.2, a measurement of Ga-N bond length with a precision of 0.001c (~ 0.5 pm) is needed for studying the polarization directly from the structural perspective. This required precision is even smaller than the typical electron wavelength in TEM, not to mention the smearing out from the contrast transfer function due to objective lens imperfections. Therefore other experimental techniques need to be developed to study the polarization effects.

Electron holography (EH) in TEM is a phase imaging technique which was initially proposed to improve the resolution,[8,9] while it was later found to be particularly useful for studying the electric and magnetic fields in materials,[10-12] including polarization field in nitrides [13,14]. EH uses the phase difference between electron waves to form interference patterns, in which the electric and magnetic field in the specimen are encoded.

Generally, the phase of the incident electron beam in the TEM is modulated through two steps: First, the electron wave senses the potential of specimen, hence its kinetic energy increases and its phase shifts. Second, this modulated wave at the exit plane (the actual object in TEM) is convoluted by contrast transfer function from the objective lens as it travels in the column of the microscope, and phase information is converted into amplitude information for imaging. The whole process is the basis of the high-resolution imaging technique, in which the image contrast is determined by the crystal potential, spherical aberration, and defocus of the objective lens together, making it difficult to explain the image contrast variations. However, in electron holography we can directly obtain the phase, and the crystal electrostatic potential of materials can be mapped. The principle of electron holography will be discussed in details next.

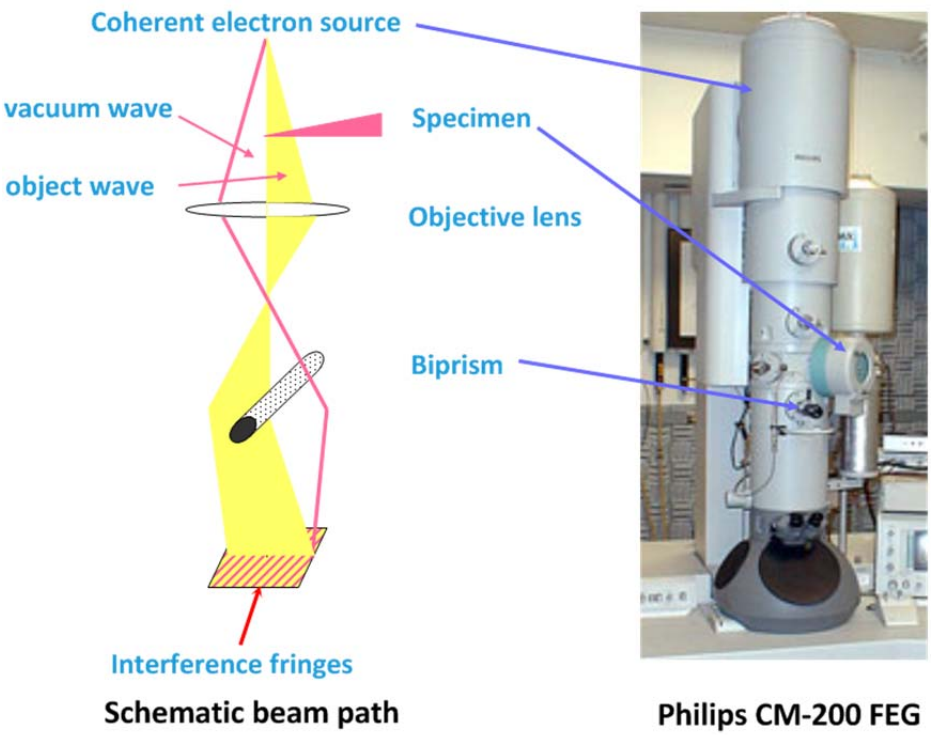

Fig. 2.7. Schematic beam path of off-axis EH. The position of electron source, specimen and biprism in Philips CM-200 FEG microscope is shown on the right.

The most common experimental approach is the off-axis electron holography setup shown in Fig. 2.7. In this setup, the highly-coherent incident electron beam generated by the field-emission gun is split into two parts in order to produce phase difference and interference. One part passing through the specimen is called the object wave, the other traveling across vacuum is called the vacuum or reference wave. If the Coulomb potential from all ions and electrons in the material can be represented by their projected value V, the energy-momentum equations for object and vacuum waves are (relativistic effects have to be considered since the kinetic energy of incident beam, E = 200 keV, is close to the rest energy of electron, E_0 = 511 keV):

$$p_{vac}{}^2c^2 = m^2c^4 - m_0{}^2c^4 = (E + E_0)^2 - E_0{}^2$$

$$p_{obj}{}^2c^2 = (E + E_0 + eV)^2 - E_0{}^2 \qquad (2.3)$$

Then the phase difference when beam is passing along a specimen with thickness of t in the z-direction can be determined:

$$\Delta\varphi = \int_0^t \frac{p_{obj} - p_{vac}}{\hbar} dz = \frac{eV(E+E_0)}{E(E+2E_0)} \frac{2\pi t}{\lambda} = C_E V t \tag{2.4}$$

where λ is the wavelength of the vacuum beam, C_E is a constant for a fixed accelerating voltage in TEM. For 200 keV electron beam, $C_E = 0.00728$ rad/V·nm.

In order to interfere, the object and vacuum waves have to be deflected to overlap spatially. This is achieved by inserting an electrostatic biprism near the back focal plane. Typically the biprism is made of metal-coated quartz fiber. When a positive voltage is applied to the biprism, the positive charges in the conducting wire attract the two electron beams causing them to overlap and interfere at the image plane. Because those two beams have an angle with respect to each other, this interference pattern, or so-called hologram, is a cosine fringe pattern superimposed on a background intensity, as expressed below:

$$I = 1 + A^2 + 2\mu A \cdot \cos(\Delta\varphi - 4\pi\alpha x / \lambda) \tag{2.5}$$

where A is the amplitude of the electron beam passing through the object, normalized to the amplitude of the incident beam. μ represents the visibility of fringes, ideally $\mu = 1$, but due to some experimental factor such as stability,[15] a 30-40% fringe contrast is common and still suitable for EH. α represents the angle between deflected beams, which is proportional to the biprism voltage V_b.[16]

The biprism voltage should be carefully chosen for holography. A higher voltage will expand the overlap region hence cover a large view of sample, also the fringe spacing is finer, leading to better spatial resolution; however, the stability of the biprism,

hence the visibility of fringes, could be reduced at high voltage. Depending on the region of interest, a biprism voltage from 30V to 120V can be applied.

A digital reconstruction process can be used when the image is recorded with a charge coupled device. The Fourier transform of equation 2.5 gives:

$$FT(I) = FT(1+A^2) \otimes \delta(k) + FT(\mu A e^{i\Delta\varphi}] \otimes \delta(k - 2\alpha/\lambda) + FT(\mu A e^{-i\Delta\varphi}] \otimes \delta(k + 2\alpha/\lambda) \quad (2.6)$$

which is a complex image with real and imaginary parts. This Fourier transformed image in the k-space can be divided into 3 bands corresponding to three terms in Equation 2.6. The first term (centered at k=0, central band) does not contain the phase information, while the other two terms (sidebands) that are complex conjugates of each other, have phase information $\Delta\varphi$ encoded. To retrieve the phase, the Fourier transformed image is cropped with only one sideband remained. Then this cropped sideband image will be inverse Fourier transformed, the phase and amplitude parts is simultaneously acquired. Figure 2.8 gives an example of EH reconstruction. The sample studied is an InGaN quantum well embedded in GaN quantum barriers. The phase and amplitude images are reconstructed from the original pair of holograms.

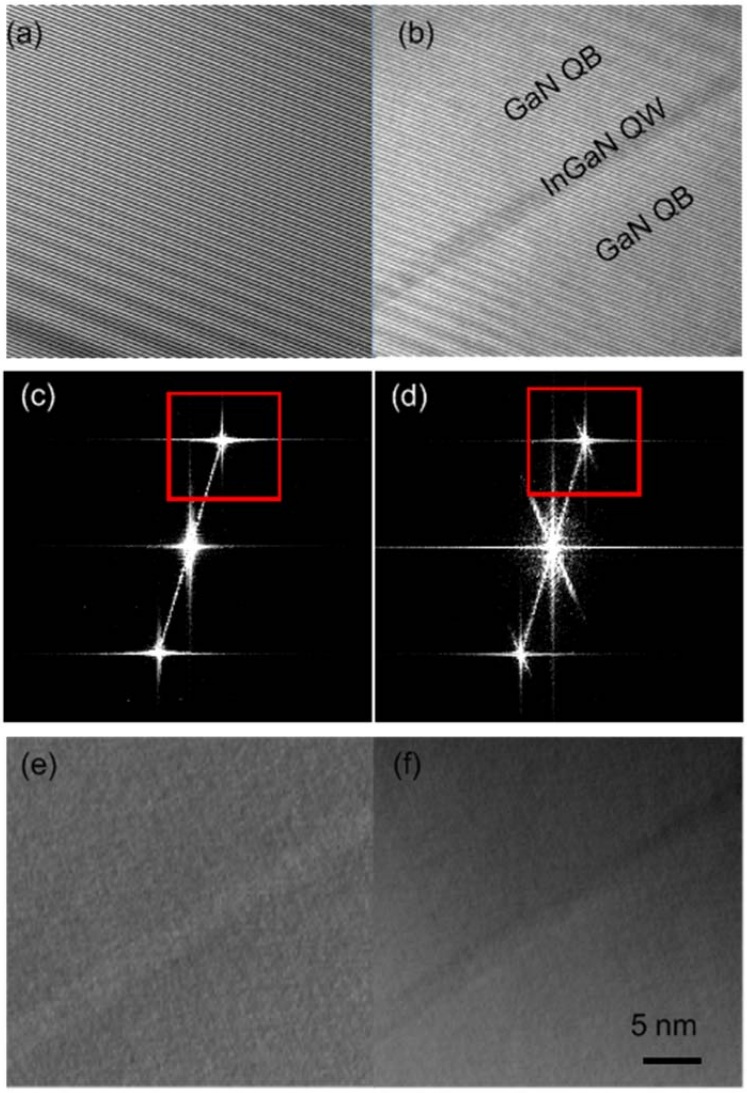

Fig. 2.8. Hologram reconstruction for an InGaN/GaN quantum well/barrier sample. (a) and (b) are holograms taken with and without the sample, respectively. (c) and (d) are the corresponding FFT images (showing the log of modulus) of (a) and (b). The sidebands are indicated by the red squares. (e) and (f) are phase and amplitude distribution of the sample, reconstructed from sidebands in (c) and (d).

According to Equation 2.4, the potential profile of interest can be acquired once the phase image is obtained and the sample thickness is known. Here the amplitude image is helpful for determining the sample thickness. Taking inelastic scattering as Poisson processes with a characteristic length λ, since the interference happens only if the

number of inelastic scattering events is zero, the thickness information can be related with the amplitude information by: [17]

$$t = 2\lambda \ln(A_v / A_o) \tag{2.7}$$

where A_v / A_o is the amplitude ratio of vacuum and object waves, which is obtained by dividing the sidebands from a pair of hologram with and without the object. λ is the inelastic mean free path for 200 keV electrons passing through the material. If the TEM sample thickness is known from a particular geometry, or can be determined by an independent technique such as CBED, the inelastic mean free path λ can be properly established. A standard GaN sample is used for the calibration of λ. The determination of thickness using CBED is already shown in Fig. 2.3, and the thickness profile from EH using 61 nm as inelastic mean free path is shown in Fig. 2.9, with the standard deviation as error bar. Those results indicate a calibrated value of 61 nm as inelastic mean free path of 200 keV electrons passing through GaN material. Because the region of interest usually contains a large area of GaN material, with the calibrated value of λ, the full thickness profile t(x,y) can be extrapolated and the potential profile V(x,y) can be obtained using Equation 2.4.

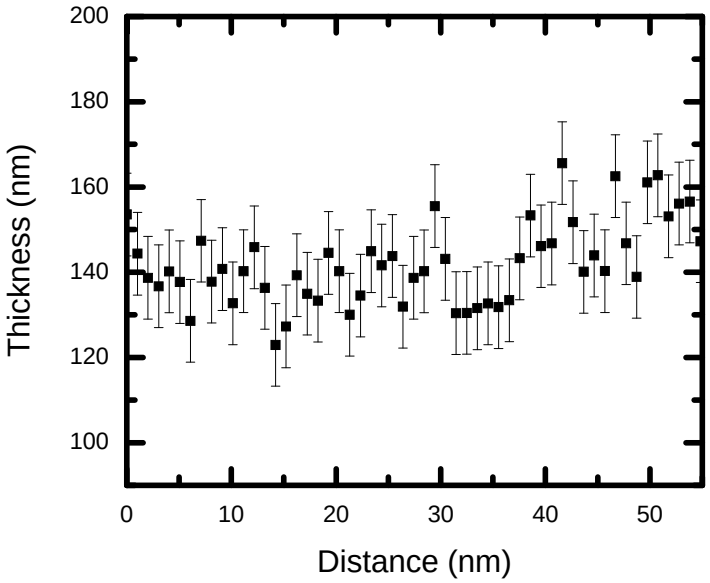

Fig. 2.9. EH thickness profile of a standard GaN sample. An inelastic mean free path of 61 nm is assumed. The resulting thickness is consistent with the value obtained in Fig. 2.3 using CBED for the same specimen, ~140 nm.

One practical problem during the hologram reconstruction is the phase unwrapping.[18] On the one hand, the phase is calculated from the complex image of the inverse Fourier transformed sidebands, which implies that only the principal value of the complex number argument (within $[-\pi, \pi]$, so-called wrapped phase) is accessible. On the other hand, taking typical parameters in equation 2.4, such as V ~ 16.8 eV for GaN [19] and t=100 nm, the physically-meaningful phase $\Delta\varphi$ is around 12.2 rad that is outside the $[-\pi, \pi]$ range. The difference between wrapped phase and physically-meaningful phase has to be treated by the process called phase unwrapping.

Phase unwrapping algorithm generally assumes that the phase map is continuous, in practice, the local phase jump is less than π.[20] Only under this assumption, the phase can be recovered unambiguously. The theoretical values of electrostatic potentials of group-III nitrides differ by less than 4 V [19], so that the phase discontinuity in nitride heterostructure is estimated to be less than π when the sample thickness is not far beyond

100 nm. That guarantees that the most phase unwrapping algorithm is applicable for nitride heterostructures. If the electrostatic potential changes very abruptly for some other heterostructures, or if the TEM specimen is too thick, special attention should be paid when applying phase unwrapping.

Phase unwrapping is achieved by integrating the wrapped phase gradients. This can be easily implemented for the one-dimensional case. For a 2-D phase map, the integration should be path independent in order to make the result consistent. However, this is not automatically satisfied as demonstrated in the literature. [21] To overcome this problem, the residues of phase map have to be determined first and branch cuts that connecting residues need to be made carefully, depending on the specific algorithm. Finally the integration can be performed along a path not crossing with branch cuts. Three different algorithms, including Goldstein, Flynn and a hybird of those two have been implemented as the "ASUholography" script by Paul R. Perkes and M. R. McCartney. The author of this dissertation greatly appreciates using the results of their work.

REFERENCES

[1] P. E. Batson, N. Dellby, and O. L. Krivanek, Nature **418**, 617 (2002).

[2] D. J. Smith, Materials Today. **11**, 30 (2008).

[3] P. Ruterana, R. Aguinet, M. A. Poisson, Phy. Stat. Solidi (b). **216**, 663 (1999).

[4] D. Korakakis, K. F. Ludwig, and T. D. Moustakas, Appl. Phys. Lett. **71**, 72 (1997).

[5] F. A. Ponce, D. P. Bour, W. T. Young, M. Saunders, and J. W. Steeds, Appl. Phys. Lett. **69**, 337 (1996).

[6] F. Wu, Y. D. Lin, A. Chakraborty, H. Ohta, S. P. Denbaars, S. Nakamura, and J. S. Speck, Appl. Phys. Lett. **96**, 231912 (2010).

[7] B. Fultz, and J. M. Howe, 2001. *Tansmission electron microscopy and diffractometry of materials*, 2nd ed. (pp. 362). New York: Springer.

[8] D. Gabor, Nature. **161**, 777 (1948).

[9] H. Lichte, Ultramicroscopy. **20**, 293 (1986).

[10] S. Frabboni, G. Matteucci, G. Pozzi, M. Vanzi, Phys. Rev. Lett. **55**, 2196 (1985).

[11] M. R. McCartney, D. J. Smith, R. Hull, J. C. Bean, E. Voelkl, and B. Frost, Appl. Phys. Lett. **65**, 2603 (1994).

[12] M. R. McCartney, and D. J. Smith, Annu. Rev. Mater. Res. **37**, 729 (2007).

[13] J. Cai, and F. A. Ponce, J. Appl. Phys. **91**, 9856 (2002).

[14] Z. H. Wu, M. Stevens, F. A. Ponce, W. Lee, J. H. Ryou, D. Yoo, and R. D. Dupuis. **90**, 032101 (2007).

[15] W. J. de Ruijter, and J. K. Weiss, Ultramicroscopy. **50**, 269 (1993).

[16] G. F. Missiroli, G. Pozzi, U. Valdrè, J. Phys. E: Sci. Instr. **14**, 649 (1981).

[17] M. R. McCartney, and M. Gajdardziska-Josifovska, Ultramicroscopy. **53**, 283 (1994).

[18] D. J. Smith, W. J. de Ruijter, J. K.Weiss, and M. R. McCartney MR. 1999. *Quantitative electron holography.* In L. F. Allard, E. Volkl, and D. C. Joy (Eds.), *Introduction to Electron Holography*, (pp. 1107–24). New York: Kluwer.

[19] P. Kruse, M. Schowalter, D. Lamoen, A. Rosenauer, and D. Gerthsen, Ultramicroscopy, **106**, 105 (2006).

[20] D. C. Ghiglia, and M. D. Pritt. 1998. *Two-dimensional phase unwrapping: theory, algorithm and software,* (pp. 25). New York: John Wiley.

[21] D. C. Ghiglia, G. A. Mastin, and L. A. Romero, J. Opt. Soc. Am. **4**, 267 (1987).

CHAPTER 3

CRYSTAL ORIENTATION DEPENDENCE OF POLARIZATION OF NITRIDES

This chapter reports the crystal orientation dependence of polarization in InGaN/GaN and AlGaN/GaN heterostructures. The total polarization fields of pseudomorphic $In_xGa_{1-x}N$/GaN and $Al_xGa_{1-x}N$/GaN heterostructures with $0 \leq x \leq 0.4$ have been calculated as a function of the crystal orientation, based on the pseudomorphic strain model. For an arbitrary crystal orientation, the piezoelectric polarization prevails in the InGaN/GaN system while the spontaneous polarization prevails in the AlGaN/GaN system.

Especially, the direction and magnitude of in-plane piezoelectric polarization, which is not negligible for the non-polar and semi-polar growth are first time reported. The analytical expression of in-plane polarization are derived and explicitly shown. The in-plane potential due to polarization fields in non-polar epilayers is found to depend on the degree of planarity of the heterojunctions, and on the respective lateral dimensions. Since the deviation from perfect planar structure is always observed for non-polar growth planes, our results indicate the advantage of using semi-polar growth planes for reducing the total polarization fields.

In addition, the values of polarization presented in this chapter are the basis of band diagram calculation in the following chapters.*****

(*) This chapter has been published as:
Q. Y. Wei, T. Li, Z. H. Wu, and F. A. Ponce. *In-plane polarization of GaN-based heterostructures with arbitrary crystal orientation.* Physica Status Solidi A, 10 June 2010, Vol. **207** (10), pp 2226-2232.

3.1 POLARIZATION FIELDS IN GROUP-III NITRIDES

Ab-initio calculations have shown that piezoelectric constants of group III-nitrides are about 10 times larger than those of InAs, GaAs and AlAs.[1] Also the variation in the lattice parameter in this family of semiconductors is relatively larger; for instance,InN and GaN have a lattice mismatch of ~11%. Thus, the piezoelectric polarization in InGaN epilayers grown on a GaN substrate can have large values, in the order of MeV/cm. On the other hand, wurtzite nitride material also has a non-zero spontaneous polarization along its c-axis and the magnitude of spontaneous polarization is comparable to the piezoelectric one, especially for AlGaN.[1] The internal electrostatic field of GaN-based quantum wells grown on the c-plane were first determined from the quantum-confined Stark effect,[2] and later by electron holography.[3-5]

Piezoelectric polarization develops when an internal dipole moment is generated as atoms of opposite charge polarity are displaced from their equilibrium positions by an external stress field. Its direction is determined by the stress and strain field acting on the crystal associated with a specific geometric configuration. On the other hand, spontaneous polarization is an intrinsic property of materials and its direction is always along c-axis for wurtzite structure. Therefore, the polarization field can be modified by changing the crystal growth orientation. Light emitting diodes (LEDs) have been successfully produced using non-polar heterostructures such as a-plane and m-plane InGaN/GaN quantum wells [6-7] and AlGaN/GaN quantum wells.[8] The quantum efficiency and the output power of this type of non-polar LEDs were subsequently improved by lowering the density of extended defects.[9] Semi-polar plane GaN-based LEDs and diode lasers have also been demonstrated.[10-12]

Although there have been significant advances in non-polar and semi-polar GaN-based device fabrication, the orientation dependence of the piezoelectric polarization is

still under investigation.[13-15] Recently some group reported the experimental evidence of in-plane electric field for a-plane GaN.[16] In this chapter we report a comprehensive calculation and analysis of the total polarization of nitride heterostructures with arbitrary crystal orientation, and of the in-plane piezoelectric polarization and its effect on low-dimensional heterostructures. In section 3.2, we present a general description of the calculation model of piezoelectric polarization. In section 3.3, we take both the piezoelectric and spontaneous polarization into account and calculate the total polarization for InGaN/GaN and AlGaN/GaN systems. In section 3.4, we focus on the discussion of in-plane electric field for the non-polar growth.

3.2 PIEZOELECTRIC POLARIZATION IN WURTZITE NITRIDES

The piezoelectric field is related to the strain tensor ε_{jk} by:

$$P_i = e_{ijk}\varepsilon_{jk} \tag{3.1}$$

where e_{ijk} is the piezoelectric tensor.

The strain tensor is related to the stress tensor σ_{ij}, by Hooke's law:

$$\sigma_{ij} = C_{ijkl}\varepsilon_{kl} \tag{3.2}$$

where C_{ijkl} is the elastic stiffness tensor.

Due to the symmetry of the wurtzite structure, the number of independent elements in the piezoelectric and the elastic stiffness tensors can be reduced to the following matrix notation:[17]

$$e_{ijk} = \begin{bmatrix} 0 & 0 & 0 & 0 & e_{15} & 0 \\ 0 & 0 & 0 & e_{15} & 0 & 0 \\ e_{31} & e_{31} & e_{33} & 0 & 0 & 0 \end{bmatrix}$$

and,

$$C_{ijkl} = \begin{bmatrix} C_{11} & C_{12} & C_{13} & 0 & 0 & 0 \\ C_{12} & C_{11} & C_{13} & 0 & 0 & 0 \\ C_{13} & C_{13} & C_{33} & 0 & 0 & 0 \\ 0 & 0 & 0 & C_{44} & 0 & 0 \\ 0 & 0 & 0 & 0 & C_{44} & 0 \\ 0 & 0 & 0 & 0 & 0 & \frac{C_{11}-C_{12}}{2} \end{bmatrix}$$

where the suffixes follow the standard matrix notation:

1→xx, 2→yy, 3→zz, 4→yz, 5→xz, 6→xy.

A pseudomorphically strained epilayer (e.g. InGaN on a GaN substrate) experiences a biaxial strain along the basal plane. The elastic strain in the epilayer is determined by the lattice mismatch, $\varepsilon=(a_{sub}-a_{epi})/a_{epi}$. Due to the symmetry of the basal plane, the strain is uniform along all directions, and no shear strain is present on the plane. A condition of pseudomorphicity requires that:

$$\varepsilon_{xx} = \varepsilon_{yy} = \varepsilon, \varepsilon_{xy} = 0 \tag{3.3}$$

In pseudomorphic growth, the in-plane stress is the only externally applied stress, therefore:

$$\sigma_{zz} = \sigma_{xz} = \sigma_{yz} = 0 \tag{3.4}$$

The remaining strain components, ε_{zz} , ε_{yz} , and ε_{xz} , can be determined from Hooke's law in Equation. 3.2 taking into consideration the known values of the stress in Equation (3.4).

Following this approach, the strain tensor for the (0001) polar case can be derived as:

$$\varepsilon_{xx} = \varepsilon_{yy} = \varepsilon \,, \varepsilon_{zz} = -\frac{2C_{13}}{C_{33}}\varepsilon \,, \varepsilon_{xy} = \varepsilon_{yz} = \varepsilon_{xz} = 0 \,.$$

Substituting the strain tensor into Equation (3.1), the piezoelectric polarization is:

$$P_z = 2\varepsilon(e_{31} - e_{33}\frac{C_{13}}{C_{33}}), P_x = P_y = 0\,.$$

We proceed now to calculate the piezoelectric polarization for a nitride epitaxial layer grown on any (*hkil*) planes. In Fig. 3.1, the z-axis is the same as the crystallographic c-axis. The growth direction is defined as the z' axis, and the polar angle θ is the one between the z and z' axes. Due to the isotropy of the (0001) basal plane, rotating the original (xyz) coordinates system by an azimuth angle about the z-axis will not change the piezoelectric tensors and the strain tensors, which determine the magnitude of piezoelectric polarization. Thus, it is reasonable to take any direction on the basal plane as the x-axis. For convenience we may take the intersection of the (0001) and the (*hkil*) growth planes as the x-axis. For instance, in Fig. 3.1 the x-axis is along <$11\bar{2}0$> direction for the growth plane of $\{1\bar{1}0l\}$.

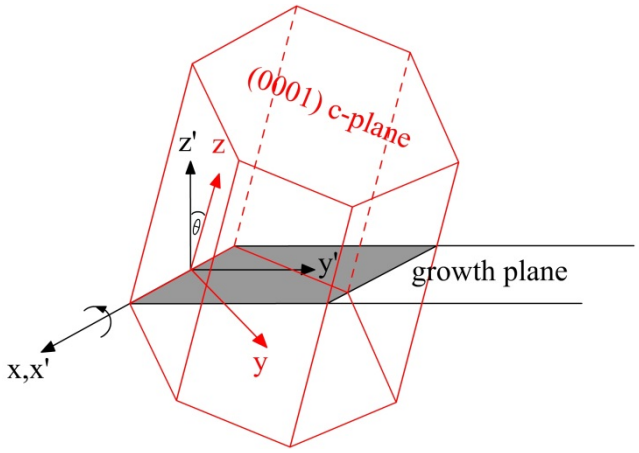

Fig. 3.1. Diagram of the coordinate system showing the polar angle defined by the z-vector (parallel to the wurtzite c-vector) and the normal to the growth plane, z'.

The previous (xyz) coordinate system is related to the new (x'y'z') coordinate system by a rotation about the x-axis that results in a new value of the polar angle. The equations (3.1) to (3.4) above become (3.1') to (3.4'), with the subscripts xyz being

changed into x'y'z'. The piezoelectric and the elastic stiffness tensors would be transformed as:

$$e_{i'j'k'} = U_{i'i}U_{j'j}U_{k'k}e_{ijk}\,,\; C_{i'j'k'l'} = U_{i'i}U_{j'j}U_{k'k}U_{l'l}C_{ijkl} \tag{3.5}$$

where U is the rotation matrix, with the polar angle as its only parameter.

We will use above equations (3.1') through (3.4') plus (3.5) to perform the calculation, with a small variant. We note that equation (3.3') is an approximation that assumes isotropy and it is only correct when the c/a ratios in the epilayer and substrate materials are exactly the same. A rigorous constrained condition has been proposed for the more general case [18]:

$$\begin{aligned}
\varepsilon_{xx} &= \varepsilon, \\
\varepsilon_{yy} &= \frac{a_s c_s - \sqrt{(a_e c_s)^2 \cos^2\theta + (a_s c_e)^2 \sin^2\theta}}{\sqrt{(a_e c_s)^2 \cos^2\theta + (a_s c_e)^2 \sin^2\theta}}, \\
\varepsilon_{xy} &= 0
\end{aligned} \tag{3.3''}$$

where the subscripts "s" and "e" refer to the substrate and the epilayer, respectively. These equations take into consideration the full geometric conditions, and we shall adopt them in the calculation of the total piezoelectric polarization.

The piezoelectric and elastic constants used in my calculation are listed in Table 3.1. The elastic constants for GaN are from experimental measurements,[22] while most for InN and AlN are calculated (we found no reliable experimental data).[23] The piezoelectric constants for nitrides are well accepted in the literature.[2]

TABLE 3.1 *Piezoelectric constants and elastic coefficients used in this work.*

Constants	e_{31}	e_{33}	e_{15}	C_{11}	C_{12}	C_{13}	C_{33}	C_{44}
GaN	0.49[a]	0.73[a]	-0.3[a]	390[b]	145[b]	106[b]	398[b]	105[b]
InN	0.57[a]	0.97[a]	-0.3[d]	223[c]	115[c]	92[c]	224[c]	48[c]
AlN	0.60[a]	1.46[a]	-0.47[a]	396[c]	137[c]	108[c]	373[c]	116[c]

The unit of the piezoelectric constant is C/m^2 and the unit of the elastic constant is Gpa.

a). Calculated in Ref. 2.

b). Experimental data from Ref.22.

c). Calculated in Ref.23.

d). Available data was not found in literature. We assume that it is close to the value for GaN.

3.3 CALCULATED VALUES OF THE TOTAL POLARIZATION

We will now determine the direction of the non-zero in-plane piezoelectric polarization. It is shown in the appendix that using equations (3.2'), (3.3'') and (3.4'), we obtain:

$$\varepsilon_{x'z'} = \varepsilon_{x'y'} = 0 \qquad \text{(A), see Appendix}$$

On the other hand, the rotation transform of the piezoelectric tensor in equation (3.5) results in:

$$e'_{11} = e'_{12} = e'_{13} = e'_{14} = 0,$$
$$e'_{15} = e_{15}\cos\theta, e'_{16} = -e_{15}\sin\theta$$

Since that $\varepsilon_{x'z'}$ and $\varepsilon_{x'y'}$ are the fifth and sixth terms of the strain tensor, it follows that the piezoelectric field along the x' axis, calculated using equation (3.1'), is:

$$P_{x'} = \sum e'_{xjk}\,\varepsilon'_{jk} = 0\,.$$

The vanishing of x'-component for piezoelectric polarization is the result of the isotropy of basal c-plane while the inclination axis (x and x') is taken as the direction lying on the basal plane. It should be noticed that the spontaneous polarization is always along c-axis so that its x' component is also zero.

In a similar way, we can derive the expression for the piezoelectric polarization along the y' direction:

$$P_{y'} = -e_{31}\sin\theta\varepsilon_{x'x'} - (e_{31}\sin\theta\cos^2\theta + e_{33}\sin^3\theta + e_{15}\cos^2\theta\sin\theta)\varepsilon_{y'y'} - (e_{31}\sin^3\theta + e_{33}\sin\theta\cos^2\theta - e_{15}\sin\theta\cos^2\theta)\varepsilon_{z'z'} - [(e_{31} - e_{33})\sin\theta\sin 2\theta - e_{15}\cos\theta\cos 2\theta]\varepsilon_{y'z'}$$

Last two equations mean that the in-plane piezoelectric polarization is along the y' direction, i.e. $[l{\cdot}h, l{\cdot}k, l{\cdot}i, -(h^2 + k^2 + i^2)]$ using Miller-Bravais indices. As an example, the in-plane electric field for the *a*- and *m*- plane growth (along the non-polar $[11\bar{2}0]$ and $[1\bar{1}00]$ directions) is parallel to [0001], which is the same as the direction of piezoelectric polarization dipole for the conventional (0001) growth epilayer. Another example is for the semipolar plane $(11\bar{2}2)$, where the in-plane polarization field is parallel to $[11\bar{2}\bar{3}]$.

We now determine the magnitude of piezoelectric polarization for different indium compositions. In a first approximation, variations in the indium composition will change the values of the strain tensor components ε_{jk} in equation (3.1'). Changes in the piezoelectric constants e_{ijk} and the elastic coefficients C_{ijkl} should also be taken into consideration by applying Vegards' law.

Figure 3.2 shows the calculated piezoelectric polarization for an InGaN layer with indium compositions of 10%, 20%, 30%, 40%, and with arbitrary crystal orientation (polar angles from 0^o to 90^o).

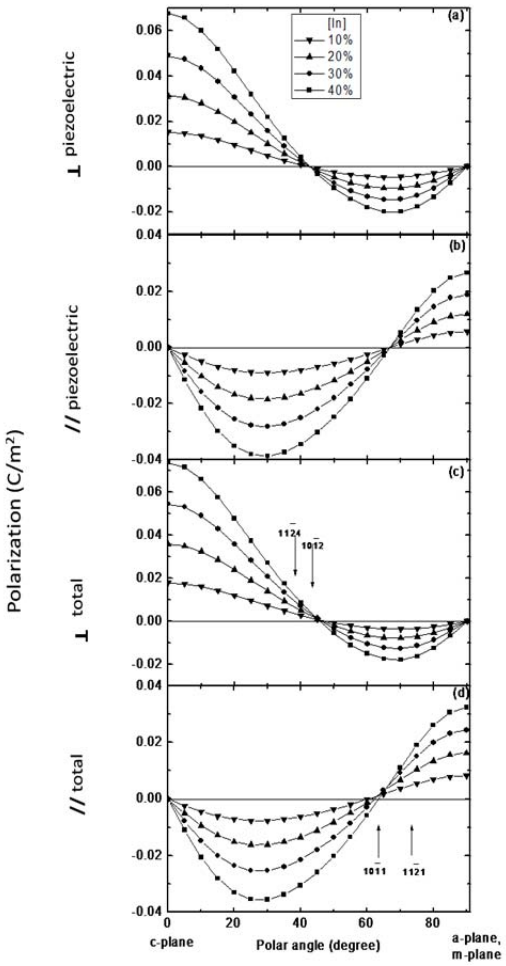

Fig. 3.2. Perpendicular and in-plane components of the polarization in the InGaN/GaN system as a function of polar angle, for indium compositions ranging from 10% to 40%. Some low-index crystallographic planes are indicated. (a) and (b) are the perpendicular and in-plane components for piezoelectric polarization, (c) and (d) are the perpendicular and in-plane components for the sum of the spontaneous and piezoelectric polarizations.

As expected, we observe in Fig. 3.2(a) that the piezoelectric polarization perpendicular to the growth plane vanishes for the non-polar planes cases (e.g., the a- and m-planes, with a polar angle of 90°). The perpendicular piezoelectric polarization also vanishes at 42° for the semi-polar planes. This orientation is close to the $(11\bar{2}4)$ and $(10\bar{1}2)$ planes. Romanov's calculation shows a crossover orientation of 45° off from the c-axis, [18] and Takeuchi's calculation shows a crossover orientation of 39° off from the

c-axis. [19] The difference could be primarily attributed to the choice of piezoelectric constants and elastic coefficients in the calculation. The value of the GaN elastic constants in the literature typically vary by ~ 20%, but the InN elastic constants are less well known and present a larger fluctuation in the literature. However, the InGaN elastic constants for indium compositions in the range of 10%-40% can be obtained by Vegard's law, while the InN constants do not affect the results as significantly as the GaN constants do.

The in-plane piezoelectric polarization is shown in Fig. 3.2 (b). It has a maximum magnitude for a polar angle of ~30°, and vanishes at 66° in the neighborhood of the $(10\bar{1}1)$ and $(11\bar{2}1)$ planes.

The next step is to superimpose the c-direction spontaneous polarization on the piezoelectric one to obtain the total polarization. One typical problem in non-polar and semi-polar growth is that the perfect planarity is difficult to be attained and some lateral "boundary" or "heterointerface" could be formed during the growth. Hence for the practical purpose we should consider a lateral InGaN/GaN sub-structure, where the difference of spontaneous polarization of InGaN and GaN contributes to the internal electric field. The expression for perpendicular and in-plane total polarization is:

$$P_{tot-z'} = P_{z'} + [P_{sp}(InGaN) - P_{sp}(GaN)]\cos\theta$$

$$P_{tot-y'} = P_{y'} + [P_{sp}(InGaN) - P_{sp}(GaN)]\sin\theta$$

where the spontaneous polarization of InGaN and GaN as a function of composition is obtained from literature.[20] The results are shown in Fig. 3.2(c) and (d). Because the spontaneous coefficients for InGaN and GaN are close, the contribution from spontaneous component is not prominent. However, this is not the case for AlGaN/GaN system, as we will see in the following parts.

Growth on planes in the vicinity of the crossover angles mentioned above should receive more attention because the reduction in the piezoelectric polarization of the InGaN layer leads to lower internal fields and improved emission efficiencies. For example, phase separation in the InGaN layer could result in dot-like structures that facilitate radiative recombination. A reduction of the total polarization should be desirable for the purpose of optimizing radiative recombination. The total polarization as a function of polar angle is plotted in Fig. 3.3, where the values in Fig. 3.2(c) and (d) are used. It is observed that the total polarization field does not vanish for any polar angle. A minimum value is obtained at about 60^{o}. In addition, the orientation dependence of the total piezoelectric polarization is not as strong as the in-plane and perpendicular polarization components.

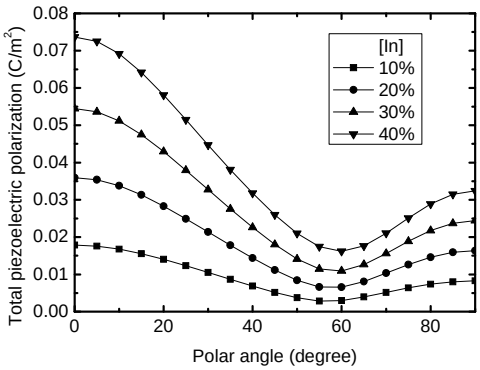

Fig. 3.3. Magnitude of the polarization for InGaN/GaN system as a function of the polar angle, for indium composition ranging from 10% to 40%.

Following the same procedure we calculate the total polarization for AlGaN/GaN system. The lattice mismatch between AlGaN/GaN is less than InGaN/GaN, but the piezoelectric constants of AlGaN are larger than InGaN. On the other hand, the value of spontaneous polarization difference between AlGaN and GaN is up to -0.056 C/m^2, which could be a dominating contribution to the whole polarization.

The calculating results are shown in Fig. 3.4 (a), (b), (c) and (d). The effect of spontaneous polarization is prominent for the arbitrary crystal orientation. In order to reduce the perpendicular polarization, it is favorable to apply non-polar growth or the semi-polar plane with large polar angle, such as $(20\bar{2}1)$. The total polarization still does not vanish for any polar angle and the minimum value is obtained at about 50^{o} (not shown here).

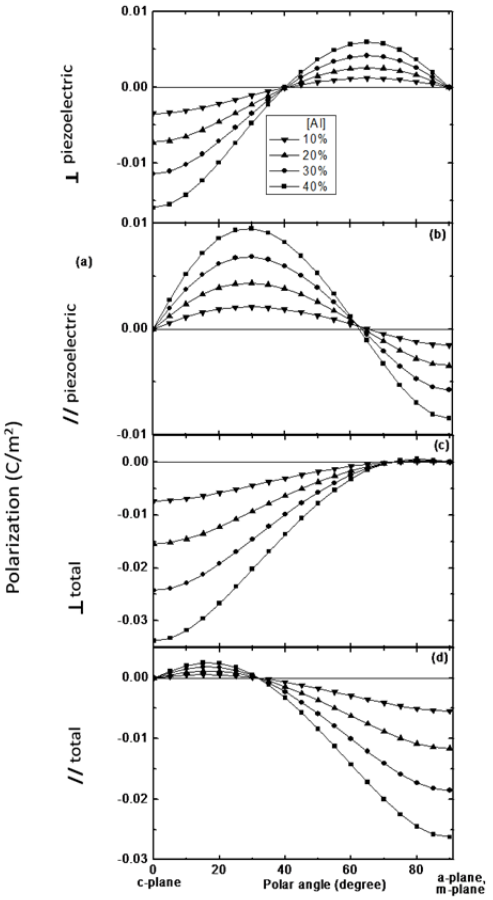

Fig. 3.4. Perpendicular and in-plane components of the polarization in the AlGaN/GaN system as a function of polar angle, for aluminum compositions ranging from 10% to 40%. (a) and (b) are the perpendicular and in-plane components for piezoelectric polarization, (c) and (d) are the perpendicular and in-plane components for the sum of the spontaneous and piezoelectric polarizations.

3.4 IN-PLANE ELECTRIC FIELD FOR NON-POLAR GROWTH

We next discuss the non-polar cases where the polar angle is 90^o. We have pointed out that for non-polar planes such as $(10\bar{1}0)$ and $(11\bar{2}0)$, the piezoelectric polarization is along the [0001] direction, which lies in the plane of the film. However, the magnitude of the non-polar case is less than half of the value in the polar case (c-plane), as shown in Fig. 3.3. This is because the conditions for strain (3.3'') and stress (3.4') are not the same for growth on non-polar planes as for the polar case, so that the magnitude of the relative displacement of the cations and anions is different. Assuming the isotropic biaxial strain we can get an approximate analytical expression for the ratio to be:

$$\frac{P_{0001}(non\text{-}polar)}{P_{0001}(polar)} = \frac{(1 - \frac{C_{12}+C_{13}}{C_{11}})e_{31} + e_{33}}{\frac{2C_{13}}{C_{33}}e_{33} - 2e_{31}}$$

In a heterojunction device with a planar waveguide, a non-zero polarization field in the junction plane will influence the propagation of the electromagnetic waves and hence the guided mode [21]. In a dot-like structure, the in-plane polarization field will affect the quantum states and the transition energies. In non-polar GaN/InGaN/GaN quantum wells, the electric field should depend on the morphological dimensions of the film. It will be zero for a quantum well with infinite lateral dimensions, but it can be quite complex if the lateral uniformity is broken like in the case of island growth. It is therefore necessary to investigate the distribution of the internal field and of the potential drop across the layer caused by the polarization.

In Fig. 3.5 we consider the geometry of the polar and non-polar cases. Let X and Z denote the dimensions of the InGaN layer along the a-axis and the c-axis, respectively. The piezoelectric polarization is a dipole moment resulting from the applied stress and consists of surface charge distributions at film discontinuities. For the polar and non-

polar cases, the dipole moment is parallel to the c-axis. For the c-plane growth, where X>>Z, these bound charges will act like an infinite parallel capacitor. For the a-plane growth where X<<Z, the charges of adjacent dipoles along the c-direction cancel each other, and the final bound charge distribution is a linear array at the ends of the film that are perpendicular to the c-axis, resembling two wires separated by the corresponding lateral dimensions of the crystal. The in-plane potential drop due to these polarization charge distributions can be written in terms of the electric field due to two parallel wire charges as:

$$|V| = \int_0^Z E(z)dz = \frac{P}{\varepsilon_0 \varepsilon_r}\frac{1}{\pi}\times$$
$$\int_0^Z [\arctan\frac{X}{2z} + \arctan\frac{X}{2(Z-z)}]dz$$

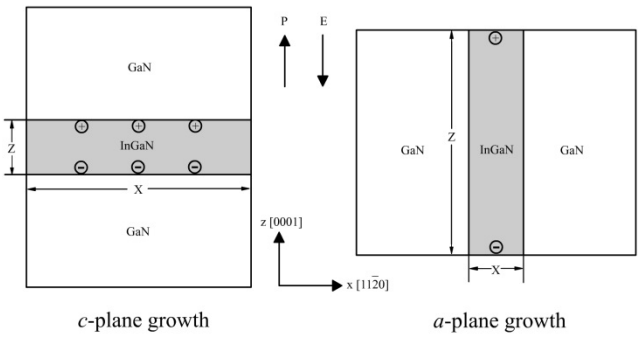

Fig. 3.5. Polarization charge distributions for the polar (left) and non-polar (right) growth. In the polar case the electric field is uniform, since the dipole moments are normal to the growth plane and the lateral dimensions are much larger than the vertical one. In the non-polar case, the electric field and potential drop depend on the dimensions of the layer.

Let us consider the effect of characteristic lateral dimension Z on the in-plane potential drop, of the typical case of a green light emitting $In_{0.2}Ga_{0.8}N$ quantum well, with a well width of X=3 nm, a device in-plane size of Z_{max}=300 μm. The in-plane potential

drop across the lateral dimension is plotted as a function of Z in Fig. 3.6, for values of Z_0 ranging from 3 nm (square quantum dots) to 300 μm (smooth non-polar quantum wells).

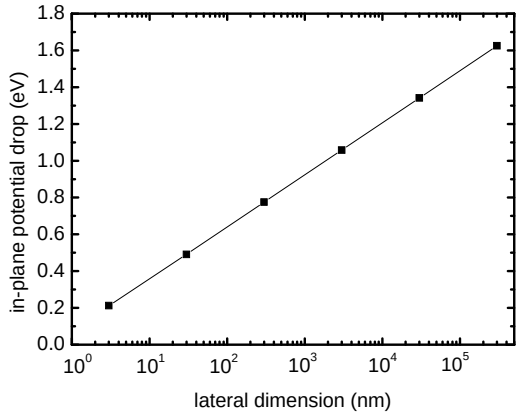

Fig. 3.6. In-plane electrostatic potential drop vs lateral dimension for a non-polar $In_{0.2}Ga_{0.8}N$ quantum well with thickness of 3 nm.

The in-plane potential drop across the lateral dimension in Fig. 3.6 can be fitted by:

$$V = 0.212 + 0.278 \log_{10}(Z / X)$$

The in-plane potential difference ranges from 0.21eV for the quantum wire case to 1.62 eV for the perfect quantum well. This corresponds to an average internal electric field ranging from 0.7 MeV/cm down to 54 eV/cm, respectively. This in-plane potential drop has always been neglected or overestimated. Even though there exists possible compensation to the polarization charges, deviations from a perfect planar structure should present strong in-plane fields, hence a significant potential drop.

3.5 CONCLUSION

We have theoretically investigated the piezoelectric and spontaneous polarization for InGaN epilayers grown pseudomophically on arbitrary (*hkil*) planes of GaN, with specific emphasis on the direction and the magnitude of the in-plane polarization

components. My calculations show that the in-plane component of the polarization is comparable in magnitude to the perpendicular component. In a heterojunction device with a planar waveguide, such strong in-plane polarization field will influence the propagation of the electromagnetic waves and hence the guided mode. In a dot-like structure, this field will affect the quantum states and the transition energies.

For semi-polar planes of InGaN/GaN system, the perpendicular component of polarization reaches zero for growth planes with a polar angle of 42^{o} between the crystallographic c-axis and the normal to the junction plane. The in-plane component vanishes for growth planes with 66^{o} polar angle. These crossover orientations are insensitive to the indium composition, and it should therefore be possible to grow graded indium composition heterostructures with simultaneously reduced internal fields in all layers. For AlGaN/GaN system, such a semi-polar growth with zero polarization components is not found due to its strong spontaneous polarization.

For devices with quantum wells grown on non-polar planes, we have found that the in-plane electric field depends on the degree of planarity of the heterojunctions, and on the respective lateral dimensions. The in-plane potential drop and average electric fields for the non-polar plane InGaN quantum well have been estimated for a range of lateral dimensions. Strong internal electric fields are expected for rough morphologies.

APPENDIX: Derivation of equation (A)

We change the stress-strain equation, $\sigma_{i'j'} = C_{i'j'k'l'}\varepsilon_{k'l'}$, to the matrix form:

$$\sigma_{i'} = C_{i'j'}\varepsilon_{j'}. \tag{A1}$$

The transformation between the matrix notation and the tensor notation is:

1'→x'x',2'→y'y',3'→z'z',4'→y'z',5'→x'z',6'→x'y' （for both $\sigma_{i'}$ and $C_{i'j'}$）;

$$\varepsilon_{1'} = \varepsilon_{x'x'}, \varepsilon_{2'} = \varepsilon_{y'y'}, \varepsilon_{3'} = \varepsilon_{z'z'},$$
$$\varepsilon_{4'} = 2\varepsilon_{y'z'}, \varepsilon_{5'} = 2\varepsilon_{x'z'}, \varepsilon_{6'} = 2\varepsilon_{x'y'} \quad \text{(for } \varepsilon_{j'}\text{)}.$$

In addition, the rotation transform of elastic constants gives:

$$C_{i'j'k'l'} = U_{i'i}U_{j'j}U_{k'k}U_{l'l}C_{ijkl}. \tag{A2}$$

where $U = \begin{bmatrix} 1 & 0 & 0 \\ 0 & \cos\theta & \sin\theta \\ 0 & -\sin\theta & \cos\theta \end{bmatrix}$

Because there are many zero elements in the elastic coefficients matrix C_{ij}, the sum in equations A1 and A2 do not have many terms, thus the expressions for $\sigma_{i'}$ can be simplified. For example, we just figure out one of them:

$$\sigma_{5'} = 2C_{44}(\cos\theta + \sin\theta)(\cos\theta \cdot \varepsilon_{x'z'} - \sin\theta\varepsilon_{x'y'}) \tag{A3}$$

As discussed in the main text, the external applied stress is within the growth plane, and therefore $\sigma_{5'} = \sigma_{x'z'} = 0$ (Equation 4'). Since there is no shear strain in the growth plane, $\varepsilon_{x'y'} = 0$ (Equation 3''). Substituting them into equation A3, we obtain that $\varepsilon_{x'z'} = 0$.

REFERENCES

[1] F. Bernardini, V. Fiorentini, and D. Vanderbilt , Phys. Rev. B. **56**, R10024 (1997).

[2] T. Takeuchi, C. Wetzel, S. Yamaguchi, H. Sakai, H. Amano, I. Akasaki, Y. Kaneko, S. Nakagawa, Y. Yamaoka, and N. Yamada, Appl. Phys. Lett, **73**, 1691 (1998).

[3] D. Cherns, J. Barnard, and F. A. Ponce, Solid State Communications. **111**, 281 (1999).

[4] J. Cai and F. A. Ponce, J. Appl. Phys. **91**, 9856 (2002).

[5] Z. H. Wu, A. M Fischer, F. A. Ponce, W. Lee, J. H. Ryou, J. Limb, D. Yoo, and R. D. Dupuis, Appl. Phys. Lett, **91**, 041915 (2007)

[6] C. Q. Chen, V. Advarahan, J. W. Yang, M. Shatalov, E. Kuokstis, and M. A. Khan, Jpn. J. Appl. Phys. **42**, L1039 (2003).

[7] A. Chakraborty, B. Haskell, S. Keller, J. Speck, S. DenBaars, S. Nakamura and U. Mishra, Jpn. J. Appl. Phys. **44**, L173 (2004).

[8] C. Q. Chen, V. Adivarahan, J. W. Yang, M. Shatalov, E. Kuokstis, and M. Asif Khan, Jpn. J. Appl. Phys. **42**, L1039 (2003).

[9] K. C. Kim, M. C. Schmidt, H. Sato, F. Wu, N. Fellows, M. Saito, K. Fujito, J. S. Speck, S. Nakamura and S. P. Denbaars, Physica Status Solidi - Rapid Research Letters **1**, 125 (2007).

[10] A. Tyagi, H. Zhong, N. N. Fellows, M. Iza, J. S. Speck, S. P. DenBaars, and S. Nakamura, Jpn. J. Appl. Phys. **46**, L129 (2007).

[11] M. C. Schmidt, K. C. Kim, R. M. Farrell, D. F. Feezell, D. A. Cohen,M. Saito, K. Fujito, J. S. Speck, S. P. DenBaars, and S. Nakamura: Jpn. J. Appl. Phys. **46**, L190 (2007).

[12] K. Okamoto, H. Ohta, S. Chichibu, J. Ichihara, and H. Takasu: Jpn. J. Appl. Phys. **46**, L187 (2007).

[13] F. Bernardini and V. Fiorentini, Appl. Phys. Lett. **80**, 4145 (2002).

[14] T. Takeuchi, H. Amano, and I. Akasaki, Jpn. J. Appl. Phys. Part 1 **39**, 413 (1999).

[15] O. Ambacher, J. Majewski, C. Miskys, A. Link, M. Hermann, M. Eickhoff, M. Stutzmann, F. Bernardini, V. Fiorentini, V. Tilak, B. Schaff, and L. Eastman, J. Phys.: Condens. Matter **14**, 3399 (2002).

[16] W. G. Hu, B. Ma, D. B. Li, H. Miyake, and K. Hiramatsu, Appl. Phys. Lett. **94**, 231102 (2009).

[17] J. F. Nye, "Physical Properties of Crystals: Their Representation by Tensors and Matrices", (Oxford, Clarendon Press, London, 1985), pp124-141.

[18] A. E. Romanov, T. J. Baker, S. Nakamura, and J. Speck, J. Appl. Phys. **100**, 023522 (2006).

[19] T. Takeuchi, H. Amano, and I. Akasaki, Jpn. J. Appl. Phys. **39**, 413 (2000).

[20] V. Fiorentini, F. Bernardini, and O. Ambacher, Appl. Phys. Lett. **80**, 1204. (2002).

[21] Decai Sun and Elias Towe, Jpn. J. Appl. Phys. **33**, 702 (1994).

[22] A. Polian, M. Grimsditch, and I. Grzegory, J. Appl. Phys. **79**, 3433 (1996).

[23] A. F. Wright, J. Appl. Phys. **82**, 2833 (1997).

CHAPTER 4

BAND DIAGRAM UNDER POLARIZATION FIELDS

4.1 BAND DIAGRAM CALCULATION AND PARAMETERS USED

The band diagram of a heterostructure is of great importance since it determines the carriers' distribution and behavior in semiconductor devices. Experimentalist developed many techniques to detect the band diagram. Most of them are indirect measurement. However, recently electron holography has been applied to directly measure the electrostatic potential profile of heterostructures, particularly for the nitrides multi-layers in which the large internal field and band offset and can be well resolved. In order to analyze the measured potential energy profile, the calculation of the band diagram becomes a critical issue.

The band diagram calculation requires a set of material properties as the input database, for nitrides most of them have been measured by independent experiments with high accuracy. However, a few parameters such as the band offsets are still in debate. Since we are only interested in the band diagram under the equilibrium condition which can be directly measured by electron holography, carrier transport properties such as mobility are off-topic. The relevant material properties for determining the band diagram of heterostructures are listed as below:

Band gap, band offsets (for conduction and valence band), impurity level (donor and acceptor), effective mass (for electrons and holes), polarization (spontaneous and piezoelectric). The methods to determine these values in the literature are discussed as below:

For nitrides, the fundamental band gap is obtained from optical absorption or luminescence. [1, 2] The band offset can be acquired by using X-ray photoelectron spectroscopy which measures the electron affinity, [3-5] then the conduction band offset

is taken as the difference of affinity according to Anderson's rule. [6] The impurity energy level can be determined by temperature-dependent Hall measurement. [7, 8] The effective mass is acquired from the dispersion curve of energy band in k-space, approximated in the extrema by a parabola. [9] The polarization is generally taken as the sheet charges on the interface, and the charge density equals the polarization difference of two layers. The parameters used for spontaneous and piezoelectric polarization has been discussed in Chapter 3. However, when this microscopic polarization is converted into macroscopic electric field and potential for the band diagram calculation, special attention should be paid.

4.2 TREATMENT OF POLARIZATION

We first examine a heterostructure ABA formed by two different materials A and B. The polarization discontinuity leads to a sheet charge density: $\sigma_P = \left| P_{SP}(A) + P_{PZ}(A) - P_{SP}(B) - P_{PZ}(B) \right|$ on the two interface. The electric field is simply $F_P = \sigma_P / \varepsilon_o \varepsilon_r$ and the potential drop across the B layer is linearly dependent on the layer B's thickness *t* through: $V = \sigma_P t / \varepsilon_o \varepsilon_r$. Now we consider a extreme case: when the thickness of B is so large that the potential drop V exceeds the band gap E_g, the Fermi level enters both conduction and valence band simultaneously at the different spatial regions, like the n- and p- degenerate semiconductors. Under this scenario, the intrinsic electrons and holes locally distributed around the AB interfaces could self-screen the polarization charges. Rigorously, a treatment for the band diagram requires solving Schrödinger and Poisson equation self-consistently. An example of the this calculation results is shown in Fig. 4.1 and Fig. 4.2, while details of the self-consistent solution be given in this chapter later. Notice the parameter used is the critical value for self-screening. Larger well-width or indium content will give a more significant reduction of

internal field due to this self-screening.

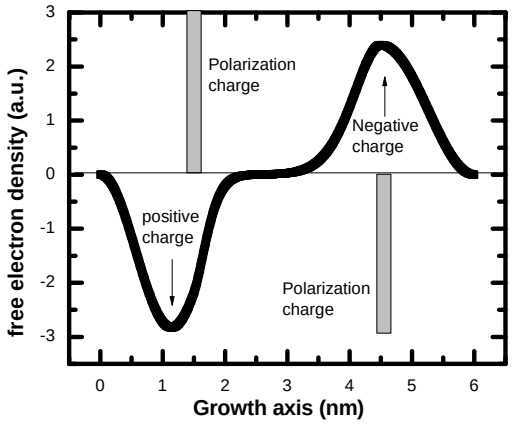

Fig.4.1. Carrier distribution determined by self-consistent solution of Schrödinger and Poisson equations in a $In_{0.5}Ga_{0.5}N$/GaN quantum well/barriers. The well thickness is 3nm. The intrinsic carriers screen the polarization charges, hence reduce the internal field in the quantum well. The polarization charge plotted is not in scale.

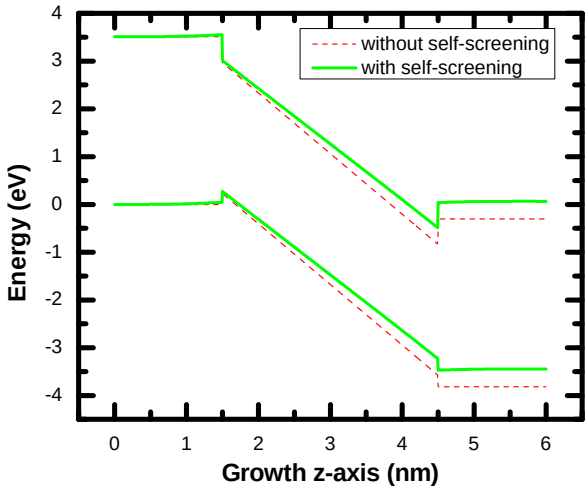

Fig.4.2. Band diagram in a $In_{0.5}Ga_{0.5}N$/GaN quantum well/barriers. The well thickness is 3nm. The initial band diagram is built by compositional profile and polarization field as the dash lines. The actual band diagram is determined by solving the Schrödinger and Poisson equations after iterations. It can be seen that the internal field is reduced by the self-screening.

Now the discussion is extended to a periodic heterostructure with ABABAB… stacking. Both the multiple quantum wells and superlattices that are common in real

devices belong to this case. As long as potential drop across one repeat of AB is not zero, a sufficient numbers of repeats will lead to a potential drop larger than band gap, which degenerates into the previous "self-screening" case. A self-consistent solution of Schrödinger and Poisson equation is again required in order to find the distribution of intrinsic carriers. Unfortunately, when the repeats (and total thickness) go large the quantum-mechanical calculation requires a higher precision in order to give the correct eigen energy and wave function. Computer codes normally assign 16-figure accuracy, which is not sufficient for this case. [10]

An alternative treatment is proposed by Bernardini which simplifies the calculation and is still physically reasonable. [11] The potential drop ΔV across the full heterostructure is assumed to be negligible, technically taken as zero. The potential drop for one repeat, ΔV_i, has to be zero since the structure is periodic. It will be named "periodic boundary condition" in the following discussion.

With this assumption, the Fermi level will always be in the middle of gap, which does not lead to significant numbers of intrinsic carriers. Therefore the electric displacement along the growth direction is conserved. The electrostatic equations in this assumption are:

$$\varepsilon_0 \varepsilon_A F_A + P_A = \varepsilon_0 \varepsilon_B F_B + P_B, \text{ and } w_A F_A + w_B F_B = 0, \tag{4.1}$$

where ε_A and ε_B are relative permittivity of material A and B, ε_0 is vacuum permittivity, P_A and P_B are total polarization (spontaneous plus piezoelectric components) of layer A and B.

The expression of electric field F from equation (4.1) is:

$$F_A = \frac{(P_B - P_A)}{\varepsilon_0} \frac{w_B}{\varepsilon_A w_B + \varepsilon_B w_A}, \; F_B = \frac{(P_A - P_B)}{\varepsilon_0} \frac{w_A}{\varepsilon_A w_B + \varepsilon_B w_A} \tag{4.2}$$

Although this treatment gives us an idea about how the electric field is affected by not only the polarization but also the layer thickness, the resulting potential and field are not compatible with any kind of polarization charge distribution for a structure with different thickness of layer A and B. In other word, a manipulation of band diagram by using (4.2) is needed in this framework if A and B layers have different thickness. The advantage of the "periodic boundary condition" treatment is it reduces the multi-layer problem into the simpler ABA heterostructure, whose solution is easier to be obtained. Also the self-screening issues are automatically removed since potential drop will not exceed band gap in only one period, typically. This treatment will be adopted in the calculation of this chapter.

4.3 SELF-CONSISTENT SOLUTION OF SCHRÖDINGER AND POISSON EQUATIONS

With the proper treatment of polarization charges or fields described in Sec. 4.2, the band diagram for a low dimensional system under equilibrium is calculated by self-consistently solving Schrödinger and Poisson equation. An initial band diagram V(x) is set by the band gap of each layer, determined by the chemical composition. From the initial band profile, the electron and hole's wave function ψ can be obtained by solving the time-independent Schrödinger's equation:

$$-\frac{\hbar^2}{2m}\nabla^2\psi(z)+V(z)\psi(z)=E\psi(z). \tag{4.3}$$

The free charge density n and p is dependent on the wave function ψ, hence the initial band profile V(x) has to be modified by the carrier's distribution, which is described by Poisson equation:

$$-\nabla^2 V=\rho/\varepsilon. \tag{4.4}$$

The carrier density ρ consists of intrinsic carriers n and p, extrinsic carriers N_A^- and N_D^+, as well as polarization charges σ_P:

$$\rho = -e(n - p + N_A^- - N_D^+ + \sigma_P) \tag{4.5}$$

where the treatment of σ_P has been thoroughly discussed in Section 4.2.

The key to calculate the carrier density is to determine the Fermi level using the charge balance equations:

$$\int (n - p + N_A^- - N_D^+) dz = 0 . \tag{4.6}$$

The polarization charges σ_P do not appear here because they exist as dipoles. The intrinsic carrier density n and p follows the Fermi-Dirac statistics, and the extrinsic carrier density follows: [12]

$$N_A^- = N_A \frac{1}{1 + g_A e^{(E_A - E_f)/kT}}, \; N_D^+ = N_D \frac{1}{1 + g_D e^{(E_f - E_D)/kT}},$$

All those carriers lead to a modified energy potential superimposed on the initial one. The band diagram is updated and Schrödinger's equation based on the new potential V'(z) will be solved. The process is repeated until the energy eigenvalues converge. When convergence approaches, the wave functions ψ and the potential energy V are simultaneously solutions of Schrödinger and Poisson equations.

4.4 NUMERICAL RECIPE

This section discusses computational implementation of self-consistent solver for Schrödinger and Poisson equations. The numerical solution of the two equations is discussed separately.

There are several methods to solve Schrödinger's equation, including shooting method, transfer matrix method, eigenvector method and many others. Shooting method

is adopted in the calculation for this dissertation with two main reasons: 1. it is an elementary method for solving second-order ordinary differential equations (e.g. time-independent Schrödinger equations), which does not call some embedded functions in specific software. It guarantees that the algorithm is easy to be implemented in different computing platforms. In contrast, the matrix-based solver always requires functions and algorithms embedded in Matlab in order to accelerate the calculation, making the code not flexible. 2. Its execution time is linearly dependent on the grid size, which has a moderate computational cost.

The shooting method for solving Schrödinger equations can be described in this way: The equation to be solved is: $\psi''(z)+\frac{2m[V(z)-E]}{\hbar^2}\psi(z)=0$. By dividing the space into grids with a separation Δ, the second-order derivative is presented by finite difference: $\psi''(i)=\frac{\psi(i+1)-2\psi(i)+\psi(i-1)}{\Delta^2}$.Therefore we have the shooting equation:

$$\psi(i+1)=[\frac{2m(V_i-E)\Delta^2}{\hbar^2}+2]\psi(i)-\psi(i-1). \tag{4.7}$$

With the boundary condition that wave function is zero outside the studied region, a starting condition for wave function can be taken as $\psi(1)$=0 and $\psi(2)$=1, as a limitation of $\psi(1)=\varepsilon$ and $\psi(2)=N\varepsilon$ when N approaches infinite and ε represents infinitesimal. The starting values have been proven to be a generally effective one for arbitrary potential profile by Harrison. [13]

By applying the initial condition in the shooting equation and iterating, wave function at any point $\psi(k)$ can be obtained. The true eigen-energy must lead to a wave function converging into infinitesimal (less than a threshold value, practically) on the

other side of the studied region. That wave function on the end of the region is named "tail" in the following discussion.

One practical problem of shooting method is the precision of solution for eigen-energy. The calculated "tail" always has a finite number, sometimes a large in magnitude. This is because the wave function has exponential terms, and it is amplified during the stepping iteration, even though the eigen-energy only changes by a small amount. Certainly using large numbers of grids can provide the better precision, but the computational time cost is not very satisfactory. This problem can be overcome by using a two-step eigen-energy searching: looking for the sign change of tail during the first rough energy scan; then perform the finer search around the rough energy solution, in order to determine the zero crossing point for tails with a high precision. The false position method is adopted in the second step as the compromise of convergence and efficiency.

For simplicity, all the above discussion is for constant effective mass of electron and holes. In a heterostructure, variable effective mass will lead to a more rigorous treatment of shooting equations. The strict shooting equation considering position-dependent effect mass model is:

$$\psi(i+1) = [\frac{2(V_i - E)m_i\Delta^2}{\hbar^2} + 1 + \frac{m_i}{m_{i-1}}]\psi(i) - \frac{m_i}{m_{i-1}}\psi(i-1). \qquad (4.8)$$

and the calculated eigen-energy typically have ~ 20 meV difference between constant effective mass model and position-dependent effective mass model, which is not negligible in the spectrum analysis. So the strict shooting equation (4.8) is adopted in the calculations.

4.5 EXAMPLES OF BAND DIAGRAM CALCULATION FOR NITRIDES HETEROSTRUCTURES

In Chapter 1 the calculation of QCSE for single quantum well has been discussed based on the self-consistent solution of Schrödinger and Poisson equations. In this section, more examples of the band diagram calculation of nitrides heterostructures will be shown.

Firstly, for a single quantum well, it was experimentally reported that the polarization fields are reduced by doping the barrier with silicon.[14] In order to understand what doping level is needed in order to quench the polarization field, the band diagram calculation is performed.

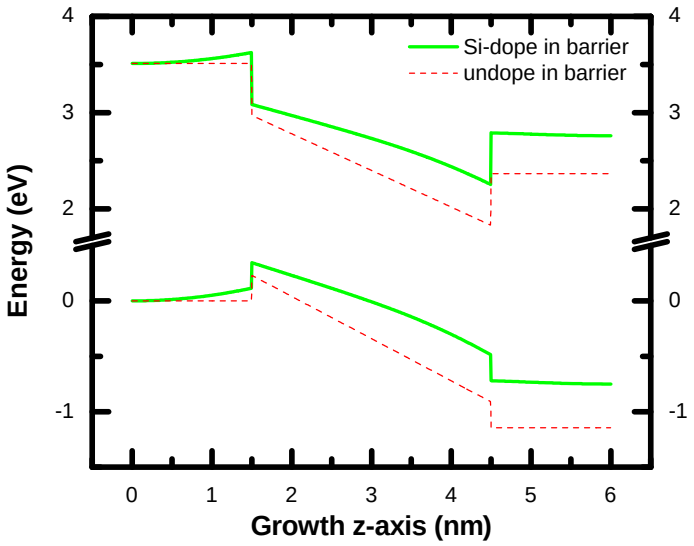

Fig.4.3. Conduction and valence bands in a *c*-plane $In_{0.1}Ga_{0.9}N/GaN$ quantum well/barriers. The well thickness is 3 nm. If the GaN barrier is doped by silicon to the level $N_d = 5 \times 10^{19}/\text{cm}^3$, the quenching of internal field in the quantum well can be clearly seen.

This phenomenon can be understood as the result of carrier screening when the modulation doping is introduced. The ionized dopant remains in the barriers while the

free electrons and holes are trapped by quantum wells. The carriers in the quantum well are drifted by the internal field toward the different side. When the doping level is comparable with the polarization charge density, more specifically, $N_d \sim \frac{\sigma_P}{t_{QW}}$, intrinsic and extrinsic carriers cancel out and the quenching of the polarization field is expected. Simple estimation gives that for $In_{0.1}Ga_{0.9}N$ quantum well, a doping level of > $10^{19}/cm^3$ is needed for reducing the polarization field, which is consistent with my numerical results in Fig. 4.3, and experimental report. [14]

For the structure discussed above, the band is flattened by using the Si-doping barrier, hence the electron and hole overlap is enhanced. However, if the original polarization field is zero (e.g. non-polar growth case), the Si-doping will only change the band diagram in a symmetrical way and the electron and hole overlap will not be much affected. In Fig. 4.4 we show the calculated band diagram of a non-polar quantum well, with and without barrier doping, respectively. Although the band diagram is curved when Si-doped barrier is adopted, the electron and hole distribution are still central symmetric and their overlap barely changed.

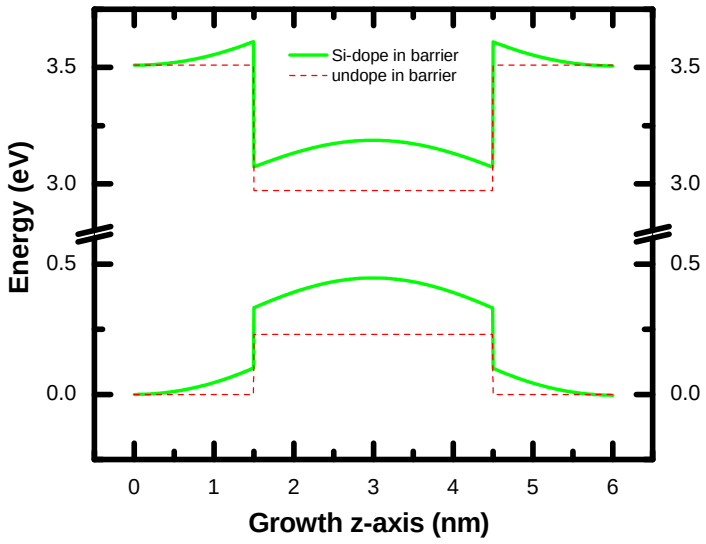

Fig.4.4. Conduction and valence bands in *m*-plane $In_{0.1}Ga_{0.9}N$/GaN quantum well/barriers. The well thickness is 3 nm. If the GaN barrier is doped by silicon to the level $N_d = 5 \times 10^{19}/\text{cm}^3$. The band diagram keeps symmetric so that Si-doping is not beneficial for electronic structure in this case.

The second structure proposed for quenching the internal field is triangular-quantum-well design, more specifically, the indium composition is linearly increasing from zero until the mid of one quantum well, then linearly decreasing to zero. The indium composition profile has a triangular shape so that it is called triangular quantum well. It should be noticed that due to the existence of polarization charges, the band profile is not triangular. The negative polarization charges sit in the first half of growth of quantum wells, while the positive polarization charges in the second half. Therefore, the polarization field gets maximized at the center of the quantum well. A calculated conduction band diagram of a *c*-plane $In_{0.1}Ga_{0.9}N$/GaN quantum well/barriers is shown in Fig. 4.5. The confined electron states are also shown. It can be clearly seen that the wave function is nearly symmetric around the center of quantum well. The improvement can be understood by two reasons: 1. The triangular indium composition profile results in a

potential energy minimum at the center of well; 2. The band tilting induced by polarization charges are reduced. Rather than sheet charges, the polarization charges now distribute uniformly in the whole well, tilting the band in a same way as the band bending of p-n junction depletion region. Using the triangular quantum well as active region of laser, the gain is significantly improved due to the enhanced overlap. [15]

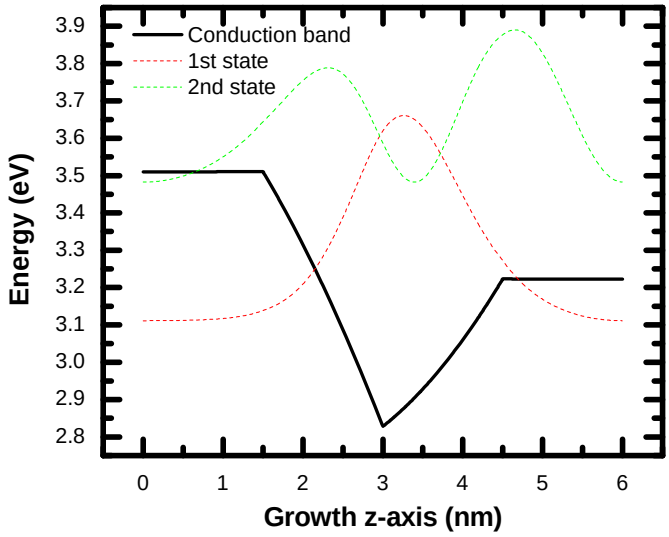

Fig.4.5. Calculated conduction band profile of a *c*-plane InGaN/GaN quantum well/ barriers. The indium composition in the quantum well is linearly increasing from 0 to 10% till the center, then decreasing from 10% to 0. The confined electron states are also plotted.

As we demonstrated from above, polarization fields are detrimental to the active region of light-emitting devices and it can be quenched by some device design such as Si-doped barrier or triangular indium incorporation. On the contrary, the polarization effect could be beneficial to the electronic devices such as HEMT. The epi-structure of a HEMT is a simply $Al_{0.3}Ga_{0.7}N$/GaN heterojunction. A doping level of $5\times10^{18}/cm^3$ in the AlGaN barrier is assumed. The self-consistent solution of band diagram is shown in Fig.

4.6, while the electron distribution is calculated from all the confined state of electrons. The band profile exhibits a negative curvature around the AlGaN/GaN interface, indicating the accumulation of free carriers. These electrons are distributed in a region less than 5nm from the figure, showing a 2-dimensional characteristic, usually called 2-dimensional electron gas (2DEG). The 2DEG is spatially separated from the ionized dopant in the barriers, leading to less impurity scattering and higher mobility.

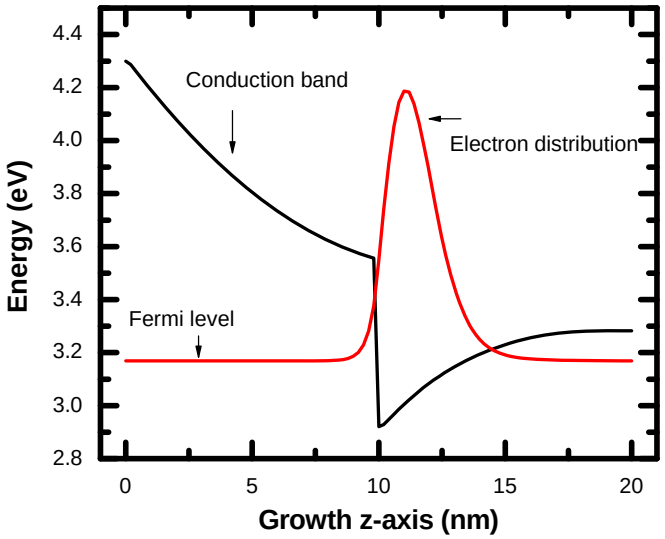

Fig.4.6. Calculated conduction band profile of a *c*-plane $Al_{0.3}Ga_{0.7}N$ heterojunction. The Fermi level and electron distribution are calculated from all the electron states and marked in the plot. 2DEG exists around the AlGaN/GaN interface.

REFERENCES

[1] R. Dingle, D. D. Sell, S. E. Stokowski, P. J. Dean, and R. B. Zetterstrom, Phys. Rev. B. **3**, 497 (1971).

[2] B. Monemar, Phys. Rev. B. **10**, 676 (1974).

[3] J. R. Waldrop and R. W. Grant, Appl. Phys. Lett. **68**, 2879 (1996).

[4] S. P. Grabowski, M. Schneider, H. Nienhaus, and W. Monch, Appl. Phys. Lett. **78**, 2503 (2001).

[5] R. J. Nemanich, S. L. English, J. D. Hartman, A. T. Sowers, B. L. Ward, H. Ade, and R. F. Davis, Appl. Surf. Sci. **146**, 287 (1999).

[6] R. L. Anderson, IBM. J. Res. Dev. **4**, 283 (1960).

[7] P. Hacje, A. Maekawa, N. Koide, K. Hiramatsu, and N. Sawaki, Jpn. J. Appl. Phys. **33**, 6443 (1994).

[8] D. J. Kim, D. Y. Ryu, N. A. Bojarczuk, J. Karasinski, S. Guha, S. H. Lee, and J. H. Lee, J. Appl. Phys. **88**, 2564 (2000).

[9] V. Bougrov, M. E. Levinshtein, S. L. Rumyantsev, A. Zubrilov, "Properties of Advanced Semiconductor Materials GaN, AlN, InN, BN, SiC, SiGe", Eds. M. E. Levinshtein, S. L. Rumyantsev, M. S. Shur, (John Wiley & Sons, New York, 2001), pp 1-30.

[10] P. Harrison, "Quantum Wells, Wires and Dots: Theoretical and Computational Physics of Semiconductor Nanostructures", 3rd Edition, (John Wiley & Sons, New York, 2010), p 74.

[11] V. Fiorentini, F. Bernardini, F. D. Sala, A. D. Carlo, and P. Lugli, Phys. Rev. B. **60**, 8849 (1999).

[12] S. M. Sze, "Semiconductor Devices: Phyiscs and Technology", 3rd Edition, (John Wiley & Sons, New York, 2007), p 22.

[13] P. Harrison, "Quantum Wells, Wires and Dots: Theoretical and Computational Physics of Semiconductor Nanostructures", 3rd Edition, (John Wiley & Sons, New York, 2010), pp 70-72.

[14] T. Deguchi, A. Shikanai, K. Torii, T. Sota, S. Chichibu, and S. Nakamura, Appl. Phys. Lett. **72**, 3329 (1998).

[15] Z. W. Yang, R. Li, Q. Y. Wei, T. Yu, Y. Z. Zhang, W. H. Chen, and X. D. Hu, Appl. Phys. Lett. **94**, 061120 (2009).

CHAPTER 5

EVIDENCE OF 2DHG IN P-TYPE ALGAN/ALN/GAN HETEROSTRUCTURES

This chapter presents the polarization effects leading to a two-dimensional hole gas (2DHG) formation. For the first time, a direct electrostatic potential mapping using electron holography of a 2DHG structure is achieved, and accumulation of 2DHG is evidenced.

The electronic band structure of a modulation-doped *p*-type AlGaN/AlN/GaN heterostructure, where the AlGaN layer is compositionally graded, is studied by electron holography. The layer structure is specially designed for the strong accumulation of 2DHG, taking into consideration the large polarization discontinuity and large band offset on the AlN/GaN heterointerface. The electrostatic potential profile and 2DHG distribution have been measured with high spatial resolution across the heterostructure. A positive curvature in the potential profile has been observed, and it is considered as evidence for the accumulation of holes in a 2DHG at the AlN/GaN interface. It is also observed that the potential barrier for the 2DHG is greatly affected by acceptor ionization in the *p*-AlGaN layer. This knowledge of nature of the energy barriers for hole transfer between adjacent channels is important in the optimization of vertical conductivity of *p*-type AlGaN/GaN heterostructures, which can be used as current spreading layers in GaN-based light emitting diodes or laser diodes. *****

(*) This chapter has been published as:
Q. Y. Wei, Z. H. Wu, K. W. Sun, F. A. Ponce, J. Hertkorn, and F. Scholz. *Evidence of two-dimensional hole gas in p-type AlN/GaN heterostructures.* Applied Physics Express, 27 November 2009, Vol. **2**, 121001.

5.1 INTRODUCTION

Low conductivity of *p*-GaN is an important factor limiting the performance of GaN-based light emitting devices (LEDs) for use in solid state lighting.[1] Highly resistive *p*-layers increase the operating voltage and generate large amounts of heat, which reduce the device efficiency and lifetime. Due to the low mobility of holes, GaN based LEDs are also prone to current crowding, necessitating large area ohmic contacts having non ideal mirror properties that reduce the light extraction efficiency in the device.[2] In order to achieve superior vertical and lateral *p*-type conductivity, modulation doped AlGaN/GaN multiple heterostructures have been proposed and optimized.[3-4] Lateral conductivity can be readily improved by using the conducting channels of two-dimensional hole gases (2DHG) formed at the AlGaN/GaN interfaces. On the other hand, the vertical conductivity has to be deliberately optimized by minimizing the corresponding energy barriers. The magnitude of these barriers is affected by valence band discontinuities, spontaneous and piezoelectric polarizations, and ionized impurities. The Al composition can be graded in the AlGaN barrier layers in order to reduce the effective barrier height and remove the electrostatic potential curvature.[5,6]

Electron holography has been used in the TEM to measure electrostatic fields and charges at defects and interfaces in nitride semiconductors.[7-9] The phase of the electron hologram is proportional to the projected electrostatic potential according to the formula $\phi = C_E V t$, where C_E is the interaction constant（0.00728 rad/V nm for 200keV accelerating electrons and t is the sample thickness which can be obtained from the amplitude of the electron hologram.[9] The internal fields are proportional to the slope of the electrostatic potential profile derived from the hologram. The corresponding electrostatic charges are found using Poisson equation, and are related to the curvature of the potential profile. Electron holography has recently been used to determine the

conduction band structure of *n*-type modulation doped AlGaN/AlN/GaN heterostructures with graded AlGaN, where the 2DEG is discerned as a negative curvature in the potential profile.[10] In this paper, we investigate the electrostatic potential distribution of a *p*-type modulation doped AlGaN/AlN/GaN multi-heterostructure with a compositionally graded AlGaN, with the objective of understanding the characteristics of the 2DHG distribution along the growth direction.

5.2 EXPERIMENTAL DETAILS

The AlGaN/AlN/GaN heterostructure was epitaxially grown by metal-organic chemical vapor deposition on a nominally undoped 3-μm thick GaN layer on a *c*-plane sapphire substrate by Dr. Hertkorn at Ulm University, in Germany. The 2DHG heterostructure consists of 6 periods; each period starts with a 0.5 nm AlN layer, followed by a 5 nm nominally undoped GaN layer, and ending with a 12 nm AlGaN barrier layer with an Al concentration that is nominally graded linearly from 0% to 10%. The thin AlN layer is used to avoid interface alloy scattering effects and to improve the lateral mobility of the 2DHG. The initial portion of the AlGaN layer has a Mg doping level of $\sim 1\times10^{19}$ cm^{-3}, but the Mg flux is turned off for the last few nanometers. Cross-sectional thin samples were prepared for transmission electron microscopy (TEM) using standard mechanical polishing and argon-ion milling techniques. Samples for holography measurement were chemically etched in KOH solution, and cleaned carefully using an air gun. We have used a field-emission TEM equipped with an electrostatic biprism and operated with an incident electron beam of 200 keV. All electron holograms were recorded using a charge-coupled device camera. The multilayer heterostructure under study is shown in Fig. 5.1, with a diagram showing details of one period and a bright field TEM image. The AlN layer appears with the brightest contrast in the TEM image, followed by the GaN layer with a relatively darker contrast, and the graded AlGaN layer

with fading brightness. The valence band diagram for one period was calculated and is shown in Fig. 5.1(c). The accumulation of holes is expected to happen in the GaN adjacent to the AlN/GaN interface.

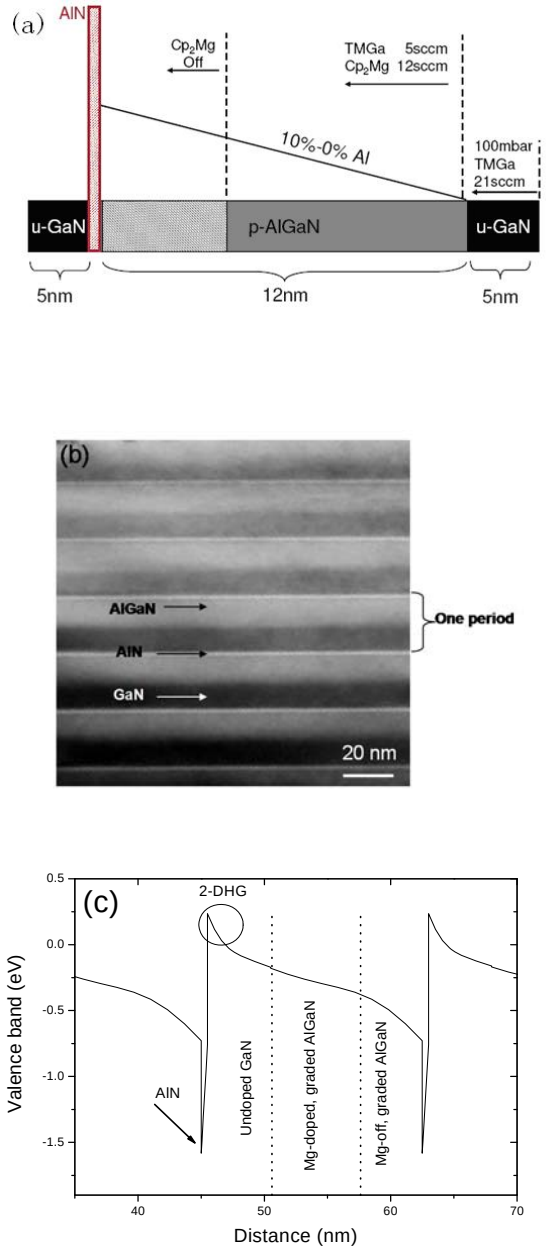

Fig. 5.1. (a) Schematic growth structure. The growth direction is from right to left. (b) Bright-field transmission electron micrograph of the *p*-AlGaN/AlN/GaN heterostructure. The growth direction is from bottom to top. The brighter contrast corresponds to the layer with higher Al composition, and (c) valence band profile for one period in the heterostructure. The location of the 2-DHG accumulation is circled.

To obtain adequate electron holography data, the cross-section TEM specimen must be oriented away from strong diffraction conditions. We achieved this by first rotating the specimen within the heterostructure plane out of the zone axis; while retaining the sharp projection of the 2-D structures. We then tilted slightly in the perpendicular direction in order to minimize diffraction. The quality of the signal may still deteriorate to some extent due to dynamic diffraction. In practice, we have found that a relatively thick region (~ 200 nm) and a large in-plane tilt angle can lead to strong and uniform signals.

The object and reference waves interfere coherently at the image plane of the microscope. Their relative phase shift is encoded in the intensity distribution of the interference sinusoidal fringes. A standard method has been used for data extraction and processing in electron holography. The deconvolution of the holographic phase and amplitude is achieved by a Fourier transform of the hologram, followed by an inverse Fourier transform of one of the resulting sidebands that is produced by the electrostatic field of the biprism.[9] The resulting phase and amplitude images are shown in Fig. 5.2. The biprism voltage of holography was set to accommodate the simultaneous requirements of sampling size and interference fringe contrast. Due to the experimental limitations, only the three periods adjacent to the surface are sampled.

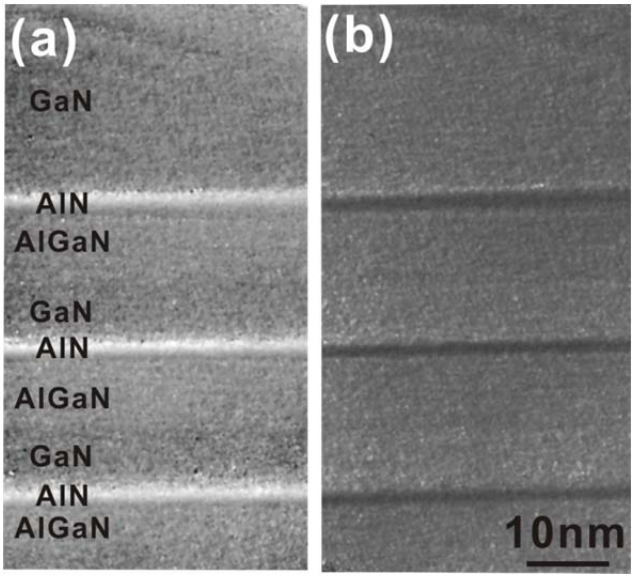

Fig. 5.2.(a) Phase image and (b) amplitude image of p-AlGaN/AlN/GaN extracted from an electron hologram for the top three periods.

The phase image $\phi(x,y)$ and to the electrostatic potential distribution $V(x,y)$ are related by $\phi(x,y) = C_E V(x,y)t$. The amplitude and sample thickness *t*, are related by $t = 2\lambda \ln(A_r / A_o)$, where λ is the inelastic mean free path and A_r and A_o are the amplitudes of the reference and object waves, respectively. It is important to use the correct value for the inelastic mean free path, which we measure using convergent beam electron diffraction techniques to be 61 nm for 200 kV electrons in GaN as shown in Chapter 2. With this value, we obtain a mean inner potential of ~13.4 V for GaN, in good agreement with published values.[11] Finally we obtain the 2D distribution of the electrostatic potential from $V(x,y) = \dfrac{\phi(x,y)}{2C_E \lambda \ln(A_r / A_o)}$, and then integrate along the growth direction to obtain the one-dimensional potential profile. The results are shown in Fig. 5.3(a). The locations of the interface are determined by a careful match between diffraction contrast and phase image. The formation of 2DHG is revealed by a positive

curvature formed in the GaN immediately to the right of the AlN layer in the potential energy profile. The positive curvature represents the accumulation of holes.

We now explore the connection between the electrostatic potential profile in the 2DHG region and the band structure. A self-consistent one-dimensional Schrödinger–Poisson solver [12] is used to simulate the energy band for the studied structure. The doping level is 1×10^{19} cm^{-3} in the AlGaN and AlN layers, and 2×10^{18} cm^{-3} in the GaN layers. The polarization charge density at the AlN/GaN interface is calculated to be -6.4×10^{13} cm^{-2} using values for the spontaneous and piezoelectric polarization constants given in Ref [13]. This negative charge density results in the attraction and accumulation of a 2DHG right next to the AlN/GaN interface, corresponding to a positive curvature of the potential profile. The calculated valence band potential profile for the GaN region is shown in more detail in Fig. 5.3(b). A good match between measured and calculated values of the potential variation is observed.

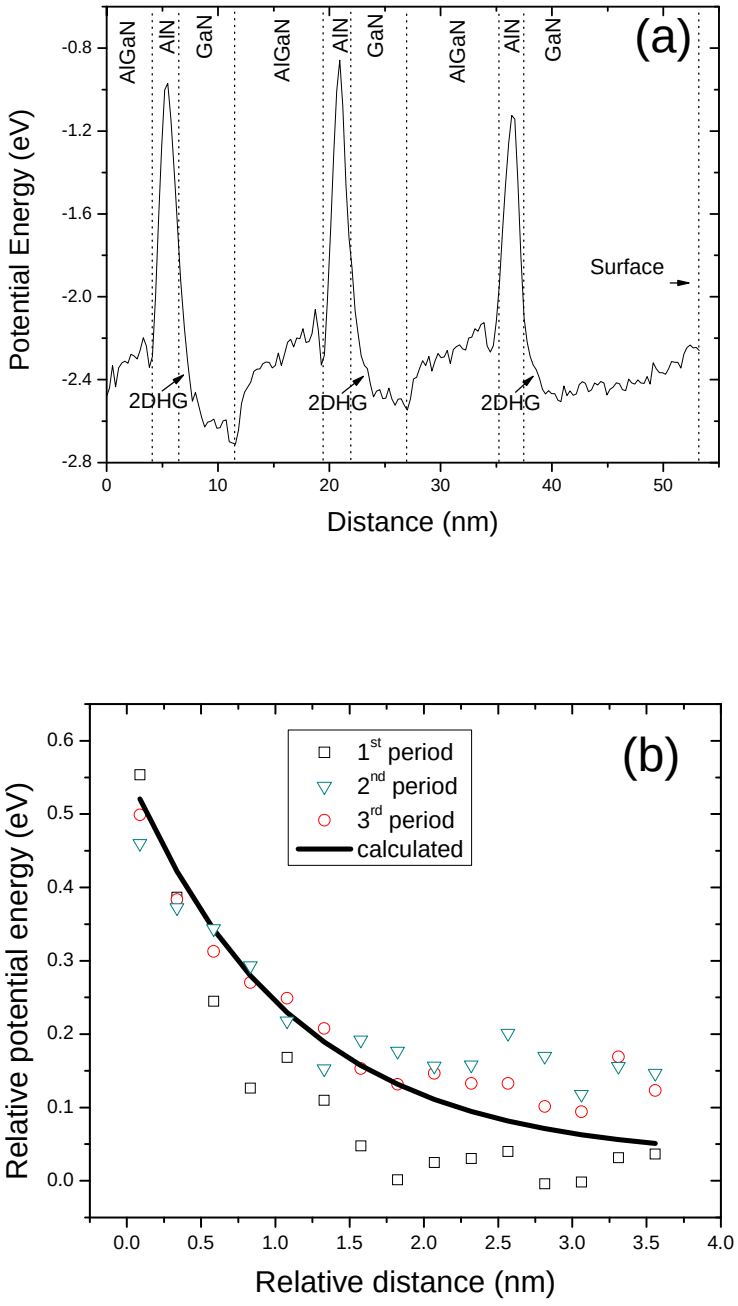

Fig. 5.3. (a) Potential energy profile across the p-AlGaN/AlN/GaN for the top three periods, derived from Fig.2, assuming an inelastic mean-free path of 61 nm for GaN.
(b) Magnified potential energy profile in one of the 2DHG region.

5.3 DISCUSSION ON THE POTENTIAL PROFILE

The electrostatic potential in a semiconductor material is related to the spatial distribution of electrostatic charges. These charges can be of four major types: (1) Interface dipole charges (related to band offsets); (2) fixed charges due to spontaneous and piezoelectric polarizations; (3) ionized impurities; and (4) free carriers that redistribute under the effect of the other charges. The electrostatic potential derived from electron holography shows continuity at the AlN/GaN interface. This indicates that the 2DHG effectively neutralizes the polarization charge sheet at the heterointerface. This is to be expected. The variation that we observe should be due to hole accumulation, in the form of a positive curvature in the potential profile. The experimental and calculated potential distributions show a noticeable curvature in the vicinity (~1nm) of the interface, but become relatively flat farther away, indicating that the 2DHG accumulation happens over only a few atomic monolayers of the interface.

In addition, it is important to understand the valence band profile in the graded AlGaN layer, which provides a barrier height responsible for vertical transport of holes. In the graded AlGaN layer, we observe that the potential energy has an overall negative curvature. This curvature should be attributed to non-linear terms of the electrostatic potential, such as to doping and polarization modulations, which are the main contributors to the volume charge density. The volume charge density can be written as the sum of two components: the negative (ionized) acceptor density N_A^- in the *p*-AlGaN, and the polarization charge density, $\rho_P = -\nabla \cdot P$. Due to its high ionization energy, the Mg-acceptor is not fully ionized, with $N_A^- \sim 10^{17} cm^{-3}$, about two orders of magnitude lower than the dopant density. For the second component, the spontaneous and piezoelectric polarizations in AlGaN grown on GaN have negative signs, and their

magnitude increases with Al composition. Although we cannot exactly determine the Al composition as a function of position, it is reasonable to assume that it is monotonically increasing in the graded layer during growth. Hence the polarization charge ρ_P should be continuously positive. Because the measured potential profile suggests a net negative charge density in the graded AlGaN region, we conclude that $N_A^- > \rho_P^+$, or in other word, the ionized Mg-atoms play a more critical role than the volume polarization charges in modifying the band structure in this sample.

5.4 SUMMARY

The electrostatic potential across a modulation-doped *p*-type AlGaN /AlN/GaN heterostructure has been profiled by electron holography in the TEM. The accumulation of 2DHG at the AlN/GaN interface has been determined experimentally. The measured potential profile in the 2DHG region is consistent with band structure calculations. In addition, in the graded AlGaN layer the ionized Mg-acceptor is demonstrated to affect the valence band structure significantly, while the polarization charges only exhibit a minor contribution. This information is important for the optimization of the vertical conductivity of the *p*-layer in light emitting devices and laser diodes.

REFERENCES

[1] I. Akasaki and H. Amano, Jpn. J. Appl. Phys. **386**, 5393 (1997).

[2] X. Guo and E. F. Schubert, J. Appl. Phys. **90**, 4191 (2001).

[3] E. F. Schubert, W. Grieshaber, and I. D. Goepfert, Appl. Phys. Lett. **69**, 3737 (1996).

[4] L. Hsu and W. Walukiewicz, Appl. Phys. Lett. **74**, 2405 (1999).

[5] S. Heikman, S. Keller, D. S. Green, S. P. Denbaars, and U. K. Mishra, J. Appl. Phys. **94**, 5321 (2003).

[6] M. Z. Kauser, A. Osinsky, A. M. Dabiran, and P. P. Chow, Appl. Phys. Lett. **85**, 5275 (2004).

[7] D. Cherns, J. Barnard, and F. A. Ponce, Solid State Commun. **111**, 281 (1999).

[8] D. Cherns and C. G. Jiao, Phys. Rev. Lett. **87**, 205504 (2001).

[9] J. Cai and F. A. Ponce, J. Appl. Phys. **91**, 9856 (2002).

[10] Z. H. Wu, F. A. Ponce, J. Hertkorn, and F. Scholz, Appl. Phys. Lett. **91**,142121 (2007) .

[11] L. Zhou, D. A. Cullen, D. J. Smith, M. R. McCartney, A. Mouti, M. Gonschorek, E. Feltin, J. F. Carlin, and N. Grandjean, Appl. Phys. Lett. **94**,121909(2009).

[12] M. Grundmann, Interactive 1-D Poisson-Schrödinger solver BANDENG, University of California at Santa Barbara, Santa Barbara, CA, (2004).

[13] F. Bernardini, V. Fiorentini, and D. Vanderbilt, Phys. Rev. B **56**, R10024 (1997).

CHAPTER 6

FREE CARRIER ACCUMULATION AT CUBIC ALGAN/GAN HETEROJUNCTIONS

This chapter reports the free electron accumulation in the absence of polarization. A cubic phase nitride has zero spontaneous polarization due to its higher crystal symmetry, while its piezoelectric polarization is also zero when growing along (001) plane. Therefore the band structure and charge distribution in the cubic nitride heterostructure are different from the wurtzite case. The origin of free electron accumulation of cubic AlGaN/GaN heterojunction is first time explained in this work.

Cubic $Al_{0.3}Ga_{0.7}N$/GaN heterostructures are grown by plasma-assisted molecular beam epitaxy on 3C-SiC (001) substrates. A profile of the electrostatic potential across the cubic-AlGaN/GaN heterojunction is obtained using electron holography in the transmission electron microscope. The experimental potential profile indicates that the unintentionally doped layers show n-type behavior and accumulation of free electrons at the interface with a density of $5.1 \times 10^{11}/cm^2$, about one order of magnitude less than in wurtzite AlGaN/GaN junctions. A combination of electron holography and cathodoluminescence measurements yields a conduction-to-valence band offset ratio of 5:1 for the cubic AlGaN/GaN interface, which also promotes the electron accumulation. Band diagram simulations show that the donor states in the AlGaN layer provide the positive charges that to a great extent balance the two-dimensional electron gas.*

(*)This chapter has been published as:
Q. Y. Wei, T. Li, J. Y. Huang, F. A. Ponce, E. Tschumak, A. Zado, and D .J. As, *Free carrier accumulation at cubic AlGaN/GaN heterojunctions.* Applied Physics Letter, 3 April 2012, Vol. **100**, 142108.

6.1 INTRODUCTION

The cubic phase of GaN with space group $F\bar{4}3m$ exhibits no spontaneous polarization and has been a subject of study for the past two decades.[1-4] Furthermore, all piezoelectric polarization components (along the growth direction and in the growth plane) should vanish for films grown along a <100> direction,[5] which is a different case from the wurtzite GaN where the total polarization is never zero for any orientation.[6] The absence of polarization effects is one of the advantages of cubic group III nitrides over the hexagonal group III nitrides. However, there is limited experimental understanding of the electronic band structure of cubic nitride heterostructures. In particular, accumulation of carriers at the AlGaN/GaN interface has been observed but its origin is not well understood. We report here the results of a study of the electrostatic potential variation and the origin of two-dimensional electron gas (2DEG) accumulation in cubic AlGaN/GaN heterojunctions, using a combination of transmission electron microscopy, electron holography, and cathodoluminescence spectroscopy.

6.2 EXPERIMENTAL DETAILS

A cubic $Al_{0.3}Ga_{0.7}N$/GaN heterostructure was grown by plasma assisted MBE on 3C-SiC (001) substrate by Dr. Donat As's group at Paderborn University in Germany,[7] with GaN and AlGaN layer thickness of 600 nm and 30 nm, respectively. The layer thickness and aluminum composition are close to the value of optimized wurtzite AlGaN/GaN heterostructures with high 2DEG density.[8] Because of the high conductivity of the 3C-SiC substrates, the doping concentration in our samples could not be obtained from Hall effect measurements. Capacitance-voltage (C-V) measurements on cubic AlGaN/GaN metal-oxide-semiconductor (MOS) structures [9,10] and on Schottky barrier devices [11-13] showed a background carrier concentration for the cubic GaN layer of about $9x10^{16}$-$2x10^{17}cm^{-3}$ and for the AlGaN epilayers of about $1\text{-}4x10^{18}cm^{-3}$,

respectively. Secondary ion mass spectroscopy (SIMS) measurements [10] indicated that oxygen may be the reason for this background carrier concentration. In analogy to the discussion of the growth of hexagonal AlGaN with plasma assisted MBE [14] we suspect the nitrogen gas used in the plasma source as the source of oxygen, however the Al and Ga sources cannot be excluded.

Cathodoluminescence (CL) spectra were obtained at near liquid helium temperatures, in a scanning electron microscope operated at an electron acceleration voltage of 5 kV with a beam current of 400 pA. Cross-sectional thin samples were prepared for transmission electron microscopy (TEM) using standard mechanical wedge polishing and argon-ion milling techniques. The electron holography measurements were performed on a Philips CM200 field-emission transmission electron microscope operating at 200 keV and equipped with an electrostatic biprism. All electron holograms were recorded using a charge-coupled device camera. The electron holography measurements were performed to study the electrostatic potential profile of the cubic AlGaN/GaN heterostructure. In electron holography, the phase of the electron passing through the sample is affected by the electrostatic potential in the crystal. The phase shift in the electron beam traveling across the specimen, with respect to the electron beam in vacuum, is $\phi(x,y) = C_E V(x,y)t$, where C_E is constant for a fixed electron accelerating voltage (C_E = 0.00728 rad/V-nm for 200 keV electrons), $V(x,y)$ is the projected electrostatic potential of the sample, and t is the sample thickness.[15] Using the holographic method, we digitally retrieve the phase shift $\phi(x,y)$ from the original hologram, acquire the distribution of the electrostatic potential $V(x,y)$, and integrate along the growth plane to obtain the one-dimensional potential profile. More details

about electron holography measurements for two-dimensional electron and hole gases in group III nitride heterostructures can be found elsewhere.[16, 17]

6.3 ELECTROSTATIC POTENTIAL PROFILE

Fig. 6.1 (a) is a cross-section TEM image of the cubic $Al_{0.3}Ga_{0.7}N$/GaN heterostructure. The crystal defects are mainly microtwins along {111} planes, which are common in cubic thin films.[18,19] Electron holography was performed on the region marked by the rectangle, and the integrated thickness and phase profiles are shown in Figs. 6.1 (b) and (c). The TEM specimen has a uniform thickness in the GaN region, but the AlGaN layer becomes thinner toward the surface. This is due to preferred oxidation and removal of the Al-containing region during ion milling. Thus, a polynomial fitting is applied to obtain the thickness profile in the AlGaN layer.

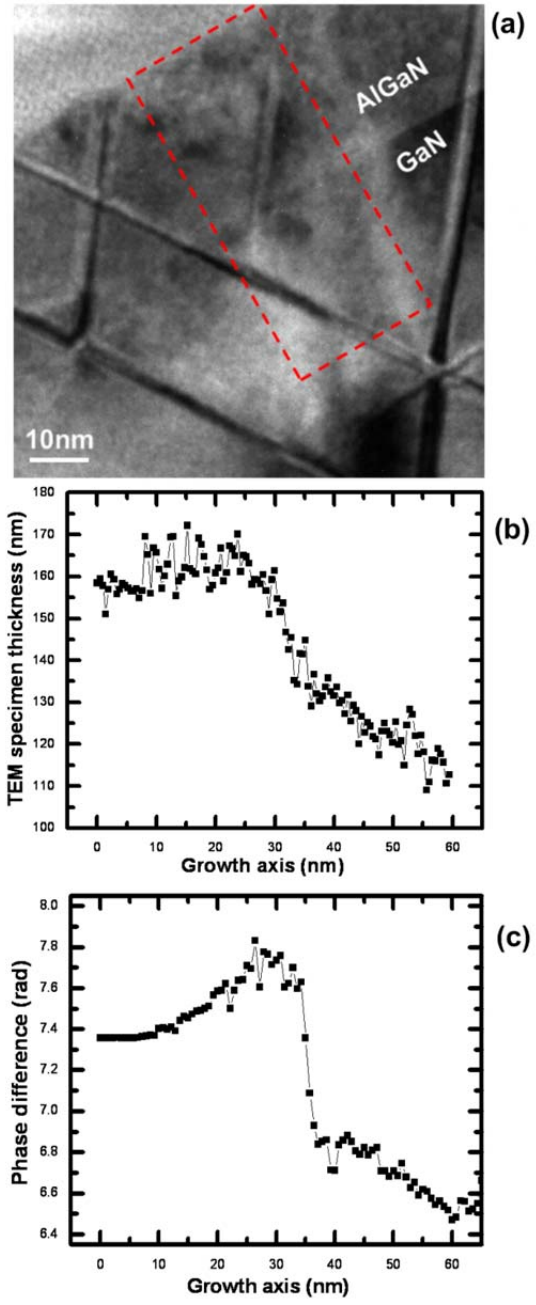

Fig. 6.1. The AlGaN/GaN heterostructure in cross section: (a) TEM image along a <110> projection showing microtwins typical in cubic GaN epitaxy; the [001] growth direction is indicated by an arrow. (b) Thickness and (c) phase profiles obtained from an electron hologram corresponding to the outlined region in (a).

The electrostatic potential profile is then obtained by dividing the phase shift by the thickness profiles; the result is shown in Fig. 6.2. In the GaN layer, the potential has a negative curvature, which indicates carrier depletion and free electrons accumulation at

the GaN/AlGaN interface. The potential becomes flat in GaN at ~20 nm away from the interface, suggesting the free electrons are confined within that range, hence have a quasi-two-dimensional characteristic. A sheet carrier concentration $5.1\times10^{11}/cm^2$ is obtained from the potential curvature using Poisson equation; this value is about one order of magnitude smaller than the density of typical wurtzite GaN 2DEG.[16] The obtained electrical data are in good agreement (within a factor of two) with conventional C-V measurements on similar cubic AlGaN/GaN heterostructures and MOS structures.[9,12,13] A positive curvature of the potential energy profile in the AlGaN region is also observed, indicating an ionized donor density which is not negligible. The electron holography measurement of the potential profile has an overall error of 15% in this experiment, mainly from the estimation of thickness and from residual diffraction contrast effects.

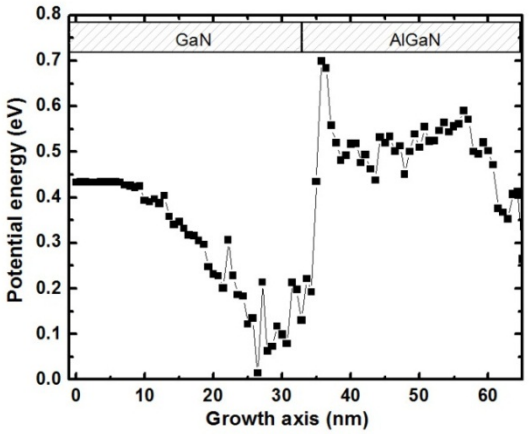

Fig. 6.2. Potential energy profile obtained by dividing the phase and amplitude profiles from the electron hologram. The 2DEG is characterized by a negative curvature in the potential energy profile with a density of $5.1\times10^{11}/cm^2$ calculated using Poisson equation. A positive curvature in the AlGaN potential energy profile is also observed, indicating a significant ionized donor density.

6.4 BAND EDGE OF CUBIC ALGAN AND GAN

To better understand this quasi 2DEG in cubic AlGaN/GaN, more information about the band-edge of cubic nitrides is needed. Figure 6.3 shows the cathodoluminescence spectrum of the sample taken at liquid helium temperature (4 K). Three separated lines at 3.29, 3.17 and 3.09 eV, correspond to GaN band-edge emissions. The 3.29 eV peak is assigned to an excitonic transition in cubic GaN, while the 3.17 eV and 3.09eV peaks are assigned to a donor-acceptor recombination and its phonon replica, in good agreement with other reports.[20-22] The AlGaN peak is at 3.95 eV with a full-width-at-half-maximum (FWHM) of 176 meV, and can be fitted by three Gaussian curves. These peaks are not as well resolved as the GaN band-edge peaks (with ~40meV FWHM), probably due to alloy fluctuations and residual oxygen contamination. The peak at 3.95 eV gives a band gap difference between cubic AlGaN and GaN of 0.78 eV, consistent with the nominal composition of the AlGaN film.

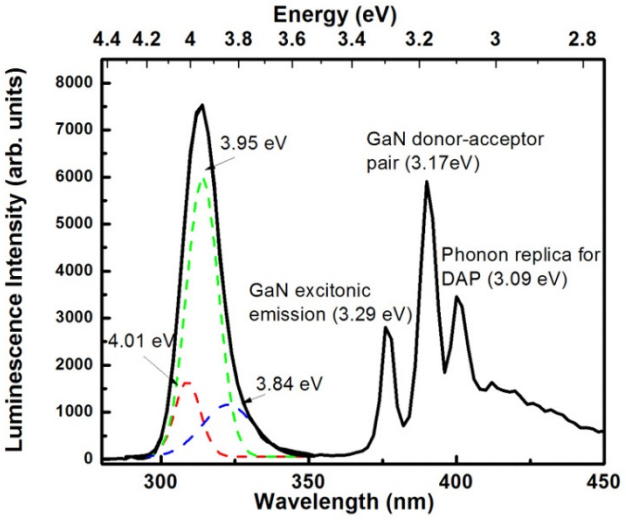

Fig. 6.3. Cathodoluminescence spectrum of the cubic AlGaN/GaN heterostructure at a temperature of 4K. The spectrum shows a broad AlGaN emission at 3.95 eV with a FWHM of 176 meV, and three separate GaN near-band-edge peaks.

6.5 BAND DIAGRAM SIMULATION

An interesting observation is that the difference in band gap between AlGaN and GaN is 0.78 eV in Fig. 6.3, while the electrostatic potential of AlGaN and GaN has an offset of ~ 0.65 eV in Fig. 6.2. The potential energy determined by electron holography can be understood as the conduction band for our case since the unintentionally doped nitride is typically n-type, and holography measurements provide a profile of the electrostatic potential experienced by the electrons in the conduction band. Hence, our experimental results suggest a conduction -to-valence band offset ratio at least as large as 5:1 for cubic AlGaN/GaN, while the first-principle calculations predict a value of 3:1 for cubic AlN/GaN.[23] The discrepancy may be due to the inaccuracy of band gap value of AlN in Ref. 23 . With our measured energy band values, the electronic band diagram can be calculated by solving the Poisson and Schrodinger equations self-consistently, where charge neutrality from donors and free electrons are satisfied. The simulated potential energy profile compared with the experimental data is shown in Fig. 6.4. In the simulation, the effective mass of electron and holes used are 0.2 and 1.2 m_0 where m_0 is rest electron mass, assuming they are not much different from ones of wurtzite nitrides. An effective n-doping level of $2\times10^{18}/cm^3$ in the AlGaN depletion region is used, and a zero polarization field for cubic nitride is assumed. The conduction and valence band offsets are set as 0.65 eV and 0.13 eV, respectively, from our electron holographic and optical spectral measurement. The first three electron states are also shown in the figure, which indicates the carriers' distribution is limited in a characteristic length less than 20 nm, in a quasi-2-dimensional nature. The existence of several occupied states is due to the larger conduction band offset of nitrides than other other semiconductors used for 2DEG, such as GaAs/AlGaAs. The consistency of experimental and theoretical data

demonstrates that the free electron accumulation is induced by the donor states in the AlGaN layer, and promoted by the large conduction band offset.

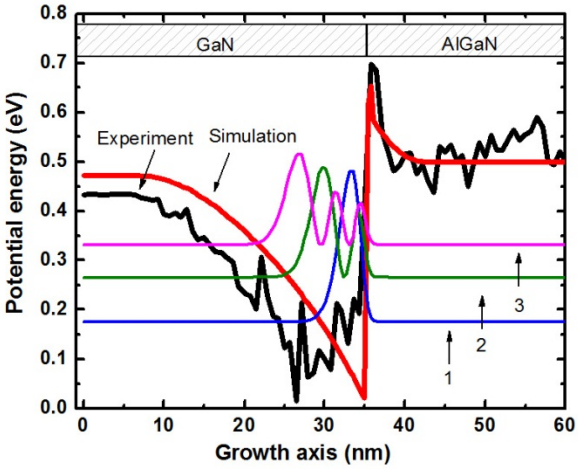

Fig. 6.4. Simulated conduction band profile compared with the electrostatic potential obtained by electron holography. First three electron states are also shown. The n-doping level of AlGaN is set at $2\times10^{18}/cm^3$.

We next discuss further aspects of the polarization charge effects. One important feature of the cubic nitride structure is its zero spontaneous polarization due to the higher crystal symmetry, in contrast with its piezoelectric polarization that depends on the growth orientation. For pseudomorphic heteroepitaxial growth, the biaxial strain is due to the lattice mismatch between the epilayer and substrate. For arbitrary growth facets, the strain and the piezoelectric tensors can be transformed by using a rotation matrix. The epitaxial growth is traction-free, which means the stress along the growth direction is zero. Under these conditions, the polarization field in the AlGaN/GaN heterostructures can be calculated for arbitrary crystal orientations. Figure 6.5 shows the calculated polarization fields for AlGaN grown on GaN as a function of polar angle, where the polar angle is defined with respect to the (001) plane. The polarization along the growth direction is maximum for a <111> growth direction, while the polarization component

along the growth plane is maximum for a <110> growth direction. For a <001> growth direction, both perpendicular and in-plane polarization values are zero. However, if a residual hexagonal phase exists during cubic epitaxial growth, there could be a local polarization discontinuity which introduces electric dipole moments. In TEM images as in Fig. 6.1(a), we observe thin hexagonal regions due to stacking faults at the boundaries of the {111} microtwins that can lead to an abrupt potential drop within a few atomic monolayers, but not to a macroscopic field. Therefore the dipole moment due to microtwins should have a negligible effect in our case. It should be noticed that the residual hexagonal regions, in sufficient high densities, could produce polarization fields that significantly modify the band diagram.

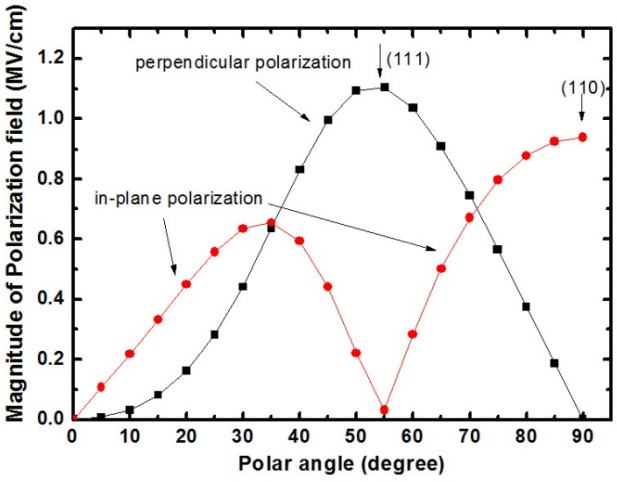

Fig. 6.5. Calculated polarization fields as a function of crystal orientation for a cubic $Al_{0.3}Ga_{0.7}N$ /GaN heterojunction. The polar angle is defined with respect to the (001) plane. The polarization value along the growth direction is maximum for a (111) growth plane, while the polarization component on the growth plane is maximum for a (110) growth plane. For a (001) growth plane, both perpendicular and in-plane polarization are zero.

6.6 CONCLUSION

The cubic $Al_{0.3}Ga_{0.7}N$/GaN heterojunction is found to have a 2DEG with a density of $5.1\times10^{11}/cm^2$, which originates from the donor states with density of

$2\times10^{18}/cm^3$ in the AlGaN layer, probably due to residual oxygen contamination. A large conduction-to-valence band offset ratio of 5:1 is observed, which enhances the 2DEG accumulation. Since the polarization field is negligible in [001] cubic structures, we demonstrate that 2DEG can be achieved in the nitride semiconductors without the need of polarization effects.

REFERENCES

[1] S. Strite, J. Ruan, Z. Li, A. Salvador, H. Chen, D. J. Smith, W. J. Choyke, and H. Morkoc, J. Vac. Sci. Technol. **4**, 1924 (1991).

[2] H. Okumura, S. Misawa, and S. Yoshida, Appl. Phys. Lett. **59**, 1058 (1991).

[3] S. Miyoshi, K. Onabe, N. Ohkouchi, H. Yaguchi, R. Ito, S. Fukatsu, and Y. Shiraki, J. Crystal Growth. **124**, 439 (1992).

[4] D. Schikora, M. Hankeln, D. J. As, K. Lischka, T. Litz, A. Waag, T. Buhrow, and F. Henneberger, Phys. Rev. B. **54**, R8381 (1996).

[5] D. Sun and E. Towe, Jpn. J. Appl. Phys. **33**, 702 (1994).

[6] Q. Y. Wei, T. Li, Z. H. Wu, and F. A. Ponce, Phys. Stat. Sol. A **207**, 2226 (2010).

[7] D. J. As, S. Potthast, J. Schörmann, S. F. Li, K. Lischka, H. Nagasawa, and M. Abe, Materials Science Forum. **527-529**, 1489 (2006).

[8] O. Ambacher, J. Smart, J. R. Shealy, N. G. Weimann, K. Chu, M. Murphy, W. J. Schaff, and L. F. Eastman, J. Appl. Phys. **85**, 3222 (1999).

[9] A. Zado, E. Tschumak, K. Lischka, and D. J. As, Phys. Stat. Sol. C. **7**, 52 (2010).

[10] A. Zado, J. Gerlach, and D. J. As, Semicond. Sci. Technol. **27**, 035020 (2012).

[11] D. J. As, S. Potthast, J. Fernandez, J. Schörmann, K. Lischka, H. Nagasawa, and M. Abe, Appl. Phys. Lett. **88**, 152112 (2006).

[12] D. J. As, S. Potthast, J. Fernandez, K. Lischka, H. Nagasawa, and M. Abe, Microelectronic Engineering. **83**, 34 (2006).

[13] S. Potthast, J. Schörmann, J. Fernandez, D. J. As, K. Lischka, H. Nagasawa, and M. Abe, Phys. Stat. Sol. C **3**, 2091 (2006).

[14] C. R. Elsass, T. Mates, B. Heying, C. Poblenz, P. Fini, P. M. Petroff, and S. P. DenBaars, and J. S. Speck, Appl. Phys. Lett. **77**, 3167 (2000).

[15] J. Cai and F. A. Ponce, J. Appl. Phys. **91**, 9856 (2002).

[16] Z. H. Wu, M. Stevens, F. A. Ponce, W. Lee, J. H. Ryou, D. Yoo, and R. D. Dupuis, Appl. Phys. Lett. **90**, 032101 (2007).

[17] Q. Y. Wei, Z. H. Wu, K. W. Sun, F. A. Ponce, J. Hertkorn, and F. Scholz, Appl. Phys. Express **2**, 121001 (2009).

[18] F. A. Ponce and J. Aranovich, Appl. Phys. Lett. **38**, 439 (1981).

[19] F. A. Ponce, W. Stutius, and J. G. Werthen, Thin Solid Films **104**, 133 (1983).

[20] D. J. As, F. Schmilgus, C. Wang, B. Schöttker, D. Schikora, and K. Lischka, Appl. Phys. Lett. **70**, 1311 (1997).

[21] J. Menniger, U. Jahn, O. Brandt, H. Yang, and K. Ploog, Phys. Rev. B **53**, 1881 (1996).

[22] G. Ramirez-Flores, H. Navarro-Contreras, A. Lastras-Martinez, R. C. Powell, and J. E. Greene, Phys. Rev. B **50**, 8433 (1994).

[23] C. Mietze, M. Landmann, E. Rauls, H. Machhadani, S. Sakr, M. Tchernycheva, F. H. Julien, W. G. Schmidt, K. Lischka, and D. J. As, Phys. Rev. B **83**, 195301 (2011).

CHAPTER 7

COMPOSITIONAL INSTABILITY IN INALN/GAN LATTICE-MATCHED EPITAXY

This chapter presents the microstructural and optical characterization of InAlN epilayer. InAlN material lattice matched to GaN is expected to have zero piezoelectric polarization and strong spontaneous polarization. However, the study of polarization effect in InAlN is not very practical since its growth deviates from optimum condition according to the reports so far. An important issue is the compositional instability that is the subject of this chapter.

The $In_xAl_{1-x}N$/GaN system is found to show compositional instability at the lattice-matched composition (x=0.18) in epitaxial layers grown by metal organic chemical vapor deposition. The breakdown in compositional homogeneity is triggered by threading dislocations, propagating from the GaN underlayer, with a screw component, and which tend to open up into V-grooves at a certain thickness of the $In_xAl_{1-x}N$ layer. The V-grooves coalesce at ~ 200 nm and are filled with material that exhibits a significant drop in indium content and a broad luminescence peak. TEM observations suggest that the structural breakdown is due to heterogeneous nucleation and growth at the facets of the V-grooves.*

(*) This chapter has been published as:
Q. Y. Wei, T. Li, Y. Huang, J. Y. Huang, Z. T. Chen, T. Egawa, and F. A. Ponce, *Compositional instability in InAlN/GaN lattice-matched epitaxy.* Applied Physics Letter, 27 February 2012, Vol. **100**, 092101.

7.1 INTRODUCTION

The $In_xAl_{1-x}N$ alloys have recently received much attention for applications in thin film structures with x ~ 18%, lattice matched to GaN. Minimizing the lattice mismatch is expected to provide better structural characteristics, and the possibility of growing thick $In_xAl_{1-x}N$ layers for distributed Bragg reflectors and optical waveguides.[1,2] However, from previous studies of thick $In_xGa_{1-x}N$ films with x~0.20, we should suspect InAlN alloy instability due to tendencies towards spinodal decomposition.[3,4] Compositional instabilities in InGaN/GaN and AlGaN/GaN systems have also been explained by a compositional pulling effect where, during the initial deposition of InGaN or AlGaN on GaN, the incorporation of In or Al atoms is impeded by lattice mismatch strain.[5,6] In this paper, we report the observation of compositional instability in thick InAlN epilayers grown on GaN, triggered by the presence of threading dislocations that produce V-shape pits, whose facets act heterogeneous nucleation sites for growth with significant lower indium content.

7.2 EXPERIMENTAL DETAILS

The InAlN epilayers in this study were grown on GaN at ~ 800^oC by metal organic chemical vapor deposition using a Taiyo Nippon Sanso SR2000 system, by Dr. Chen at Nagoya institute of technology. [7] We have investigated the effect of thickness on the structural and optical properties of films grown under otherwise similar conditions. We observe an interesting transition in the microstructure of epilayers in the thickness range between 140 and 500 nm. The microstructure of the epilayers was studied by transmission electron microscopy (TEM), in a Philips CM200 instrument operating at 200KV. The TEM specimens were prepared by mechanical wedge-polishing techniques, followed by ion milling in a cold stage in order to minimize indium diffusion.

Cathodoluminescence spectra were obtained at near liquid-helium temperatures in a scanning electron microscope.

7.3 CHEMICAL COMPOSITION DETERMINATION

The RBS spectra of InAlN/GaN samples are shown in Fig. 7.1. The expected He scattering energies by indium and aluminum atoms in our measurement are 1.741 and 1.105 MeV, respectively, and are identified in the figure with vertical lines. These values are calculated based on the energy and momentum conservation during the Rutherford backscattering process, the scattering energy is:

$$E_s = KE_i = [\frac{(M_2{}^2 - M_1{}^2 \sin^2\theta)^{1/2} + M_1\cos\theta}{M_1 + M_2}]^2 E_i \tag{7.1}$$

where K is called the kinetic factor, E_i and E_s are incident and scattered beam energy, respectively. M_1 is the mass of helium atom, M_2 is the mass of target atom, θ is backscattering angle which is 170 ^{o} for our detector setup.

The numbers of scattered hellium particles is determined by:

$$n = I \cdot \Omega \cdot N \cdot t \cdot \sigma \tag{7.2}$$

where I is the number of incident particles, Ω is the solid angle of detector, $N \cdot t$ is the area density of target particles, and $\sigma = (\frac{Z_1 Z_2 e^2}{4E})^2 \frac{1}{\sin^4(\theta/2)}$ is the cross section of Coulomb scattering. For a fixed experimental setup, the chemical composition of element A and B in the same layer can be simply determined by their scattering yield:

$$\frac{Y_A}{Y_B} = \frac{N_A}{N_B}\frac{Z_A{}^2}{Z_B{}^2} \tag{7.3}$$

From the experimental data of 140 nm-thick InAlN, the ratio of Al/In yield is ~0.320, which gives a indium content of 18.0% using equation 7.3. For the 500 nm-thick

InAlN, due to the step-like shape of yield profile, there is no a single value for chemical composition in the epilayer.

Another feature of RBS spectrum is the energy width for each peak of element. The spectral width for each atom is related to the epilayer thickness, and is due to frictional energy losses as the He atom penetrates to a certain depth before being backscattered, thus providing a compositional depth profile of each atomic species.

The scatting energy loss from the layer with thickness Δt is

$$\Delta E = \Delta t(K\frac{dE}{dx}\bigg|_{in} + \frac{1}{|\cos\theta|}\frac{dE}{dx}\bigg|_{out}) \tag{7.4}$$

where $\frac{dE}{dx}$ is the energy loss rate from the electron collision in the sample. An expression for energy loss rate is derived based on classical collision model:

$$\frac{dE}{dx} = -\frac{2\pi Z_1^{\ 2} e^4}{E} N Z_2 (\frac{M_1}{M_e}) \ln(\frac{2M_e v^2}{10 Z_2}) \tag{7.5}$$

It should be noticed that for inward and outward path, the energy loss rate take different values because the energy E is evaluated at the different depth.

Using Equation 7.5, we find that scattering energy width of Al, Ga and In are ~120-130 KeV for 140 nm-thick $In_{0.18}Al_{0.82}N$ epilayer, which are close to experimental energy width of 110-120 KeV. That also explains why the Ga peak shifts ~110 KeV from the calculated peak energy (1.588MeV) from Equation 7.1. These results demonstrate that the epilayer is totally gallium-free. For 500 nm-thick InAlN epilayer, the theoretical value of indium energy width is 490 KeV, however, a 330 KeV width of indium peak is observed. It indicates that this sample could have a porous structure or many deep pits on the surface, which reduces its effective thickness, hence the actual energy width.

To sum it up, a comprehensive analysis of the spectra shows that the 140 nm-thick InAlN layer has a uniform composition with indium content of ~18%. On the other hand, the 500 nm-thick epilayer consists of a uniform $In_{0.18}Al_{0.82}N$ layer followed by a region where the composition decreases linearly down to ~ $In_{0.10}Al_{0.90}N$.

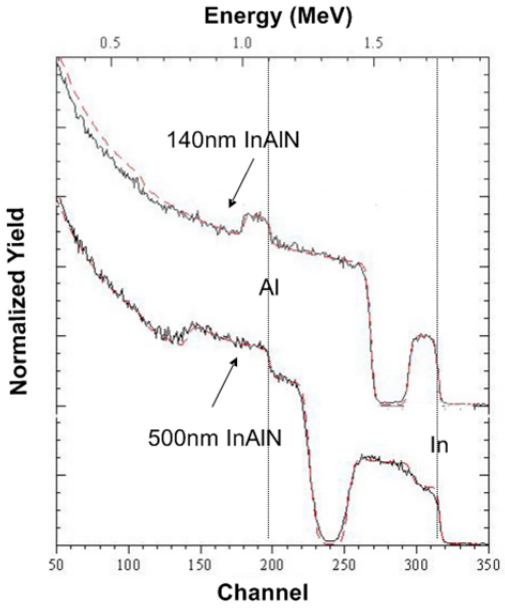

Fig. 7.1. Rutherford backscattering spectra of InAlN epilayers with thickness of 140 nm and 500 nm. Solid lines are experimental data and dashed lines are simulated. The peaks corresponding to In and Al in the simulation indicate that the 140 nm epilayer has a uniform composition of $In_{0.18}Al_{0.83}N$, while the 500 nm epilayer consists of two sub-layers, with $In_{0.10}Al_{0.90}N$ at the top and $In_{0.18}Al_{0.82}N$ at the bottom.

We also performed the energy-dispersive X-ray spectroscopy to probe the chemical variation. Spectra taken at the bottom and top region of the 500 nm-thick epilayer is shown in Fig. 7.2. Due to the lack of standard samples with known composition for calibration, the absolute value of composition obtained is not accurate, only the intensity ratio of In/Al peak is considered. The intensity ratio of In/Al peak reduces by 23.3%, assuming the bottom region has a 18.0% indium, the top region will have 14.4% indium on average, which is consistent with the trend of the RBS results.

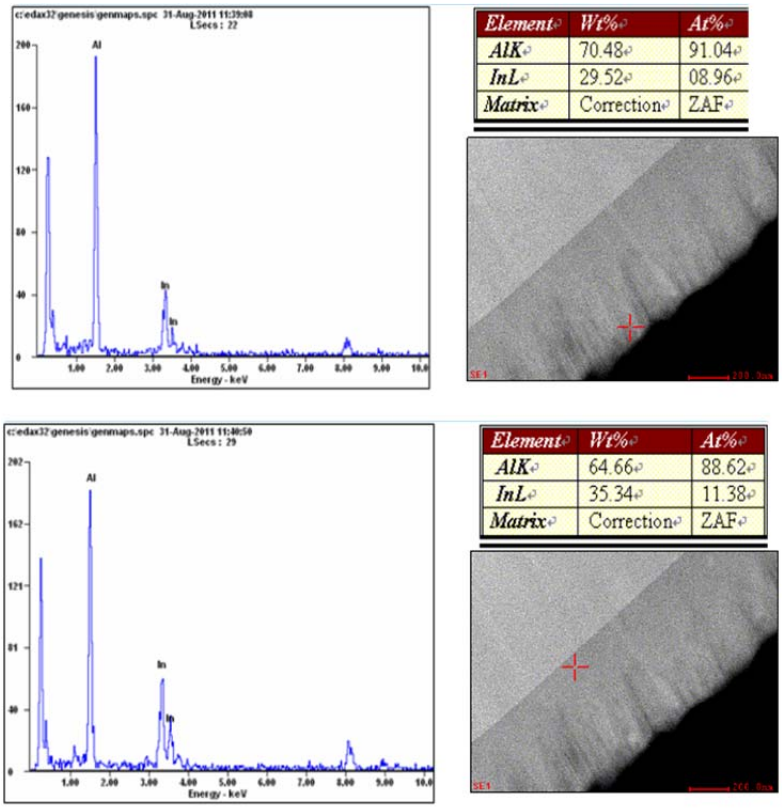

Fig. 7.2. Energy-dispersive X-ray spectroscopy of 500 nm-thick InAlN epilayer. The spectra are taken from the region marked with cross, as shown on the right side. The top region exhibits a lower In/Al intensity ratio.

Some comments need to be included here about the technique for determining the chemical composition in the films. The composition values determined by RBS are not affected by strain and defects in the epilayer, hence they are more accurate than conventional X-ray diffraction measurement, where Poisson-ratio effects need to be considered.[3] Because XRD measures the lattice constant that varies at different strain condition, the choice of Poisson ratio which describe the relationship between the in-plane strain and out-of-plane strain is critical. However, the value of Poisson ratio used in literature scattered, leading to the inaccurate determination of composition. This problem becomes worse when the epilayer is away from the relaxed case, i.e., a thin epilayer with the thickness below the critical value.

7.4 MICROSTRUCTURE PROPERTIES

We use cross-sectional TEM to understand the apparent formation of sub-layers in the thicker layer. Fig. 7.3 show an example of TEM diffraction contrast analysis of the 500 nm-thick sample. Under standard diffraction contrast, most of the dislocations are visible under g =[0002], indicating the predominance of screw and mixed dislocations, with Burgers vectors ***c*** and ***c+a***, respectively, where ***a*** and ***c*** are the unit cell vectors in the hexagonal lattice.[8] A ratio of mixed to screw dislocations of ~1:1 was found by diffraction contrast analysis.

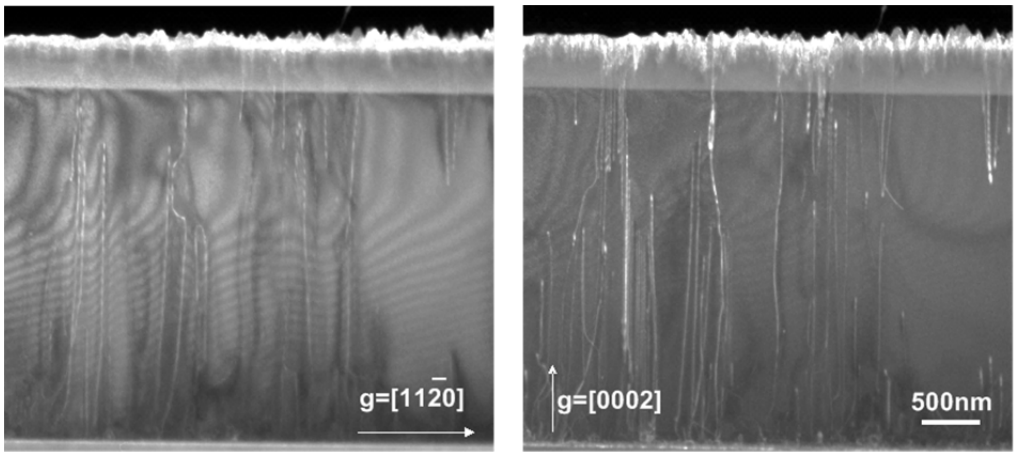

Fig. 7.3. Cross-section TEM dark-field images of 500 nm-thick InAlN epilayers grown on GaN, with (a) g=[11$\bar{2}$0], and (b) g=[0002].

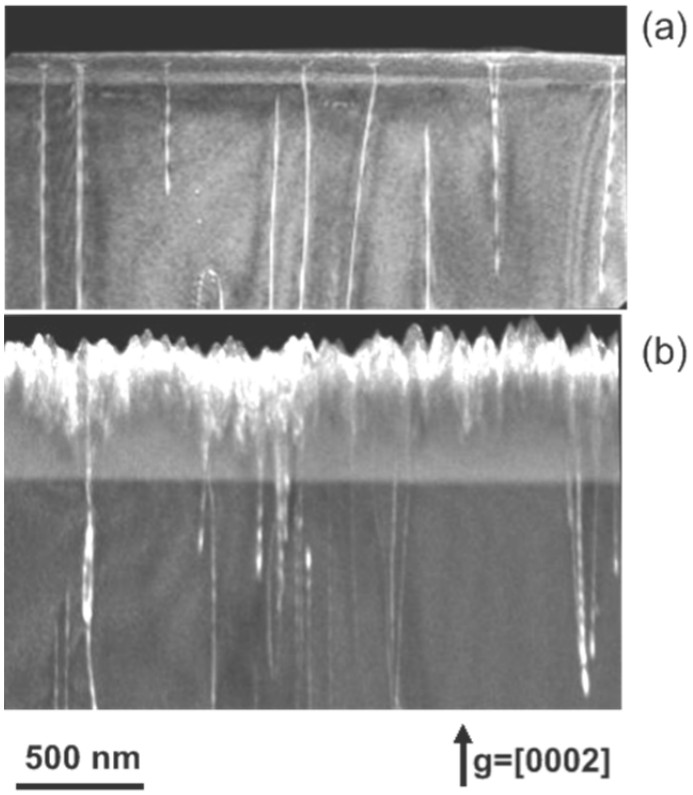

Fig. 7.4. Cross-section TEM dark-field images of InAlN epilayers grown on GaN, with thickness (a) 140 nm, and (b) 500 nm. A relatively uniform layer contrast is observed in (a), but two sublayers with different contrast are observed in (b). Threading dislocations are observed to open at certain thickness in both figures.

Figure 7.4 shows dark-field images for the 140 nm and 500 nm-thick InAlN samples for comparison. The image of the 140 nm-thick layer in Fig. 7.4(a) exhibits a relatively uniform contrast. There are only a few threading dislocations in the epilayer with an average density of ~ $2\times10^{9}/cm^{2}$. Those dislocations open up at ~ 80nm above the InAlN/GaN interface. In the 500 nm-thick film in Fig. 7.4(b), it is observed that the defects rapidly increase beyond a thickness of ~ 200 nm.

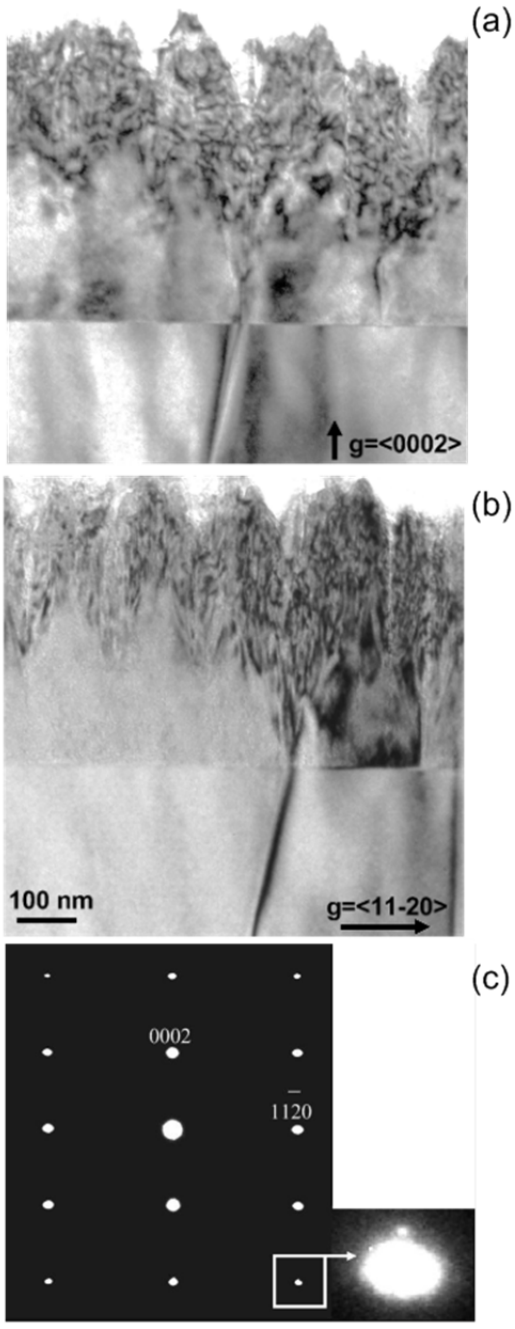

Fig. 7.5. Cross-section TEM bright-field images of 500 nm InAlN epilayers with (a) g= [0002], (b) g =[$11\bar{2}0$]. (c) Selected area diffraction pattern of top region of the film.

The microstructure of the 500 nm-thick epilayer can be observed in the bright-field TEM images in Fig. 7.5, which show the screw and edge components of the threading dislocations. These dislocations begin to open up laterally within the first ~ 100

nm above the InAlN/GaN interface, forming a V-groove with a divergence angle of ~ 36°, which is close to $\{1\bar{1}01\}$ facets. The beginning of similar openings is observed at the tip of some threading dislocations in the 140-nm-layer in Fig. 7.4(a). The fan-like regions originating from other dislocations in the vicinity but not contained in the thin TEM foil in Fig. 7.5 (of estimated cross-section thickness of ~ 80 nm) coalesce at a distance of ~ 200 nm from the InAlN/GaN interface. Microdiffraction from selected areas at the top of the film, in Fig. 7.5(c), shows two distinct sets of diffraction spots. In the magnified region in the inset, we observe a small diffraction disk above a bigger disk. The small disk corresponds to the bottom region with uniform composition, while the larger disk corresponds to the top region of the film that constitutes the largest fraction of the area selected for diffraction. The large disk is elongated along the $[11\bar{2}0]$ axis reflecting varied lateral dimensions of the crystallites responsible for this reflection. The large disk is displaced along the [0001] direction, indicative of the lower indium content in the top region. Thus, the compositional variation for thick InAlN layers can be summarized as follows. Initially, threading dislocations open up during growth due to the strain energy associated with the large Burgers vector, developing $\{1\bar{1}01\}$ facets.[9, 10] We attribute the steady opening of the screw dislocations to local strain generated by random-alloy fluctuations. During subsequent growth, crystallites with an indium composition of ~ 10% nucleate heterogeneously at the inclined facets of the open-core dislocations. The drop in indium content is clear from the RBS data in Fig. 7.1, as well as from EDX spectroscopy. No indium precipitates are detected. We suggest that the drop in indium content is related to growth on an inclined crystal plane. Or, more specifically, that compositional pulling leads to an Al-rich gas phase during c-plane growth, and that the presence of an inclined facet allows higher Al incorporation and an increase in growth rate. The crystallites that grow on the V-grooves resemble a columnar structure with

diameters of ~15nm, corresponding to a density of ~$5\times10^{11}/cm^2$. The final top surface reflects the V-groove morphology of the open-core threading dislocations. These observations in InAlN films are consistent with a model proposed by Northrup et al. for the formation of pits in GaN and its effect on In incorporation during growth of InGaN. [11]

It is interesting to compare our results with the study by Zhou et.al. [12] of InAlN thin films (~50nm thick) grown by MBE on GaN on sapphire. They observe the formation of a vertical honeycomb structure, which is attributed to lateral phase separation. Materials grown by MBE typically have a higher dislocation density, and growth happens at lower temperatures (465-480 °C) while the MOCVD thin films grow at 800 °C.

7.5 DRIVING FORCE OF COMPOSITIONAL INSTABILITY

The driving force for the compositional variation can be assessed from the phase diagram in Fig. 7.6. The solution model interaction parameter used in calculating this phase diagram is estimated from the lattice constant of InN and AlN, to be 7.0 kcal/mole.[13,14] The phase diagram shows the nature of the binodal and spinodal curves. The indium compositions observed in those samples (10% and 18%) are marked with crosses. At 800^{o}C, $In_{0.18}Al_{0.82}N$ is at the boundary between the metastable and unstable regions. Upon subsequent growth, the heterogeneous nucleation on the facet of hollow-core dislocations results in a phase with lower indium content and, from the phase diagram, with lower free energy.

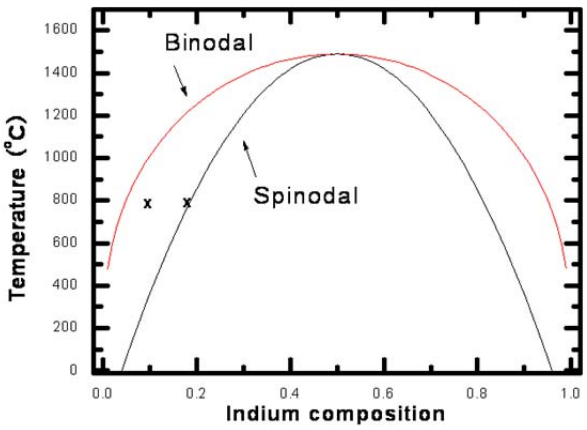

Fig. 7.6. Spinodal and bimodal stability curves, calculated using an interaction parameter of 7.0 kcal/mole. The crosses indicate the compositions of the samples studied in this work.

7.6 OPTICAL PROPERTIES

The optical characteristics of these layers can be assessed from the cathodo-luminescence spectra in Fig. 7.7. The spectra were obtained with an electron accelerating voltage of 2.5 keV, which probes the near-surface region of the thin-film structures. In the case of the 140 nm-thick layer, the InAlN emission is centered at 3.74 eV (331 nm) with a FWHM of 0.30 eV; these values are similar to those reported by others.[2] The emission peak has anomalously low energies for the composition of the film, giving the impression of large Stokes-shift (of ~ 1 eV) or, alternatively, of a large bowing parameter ($b > 10$). The large Stokes-shift implies deep localization centers in InAlN, whose origin is still not clear.[15] For the 500 nm-thick layer, the broad emission of InAlN is probably due to the degraded crystal quality and/or to high densities of point defects.

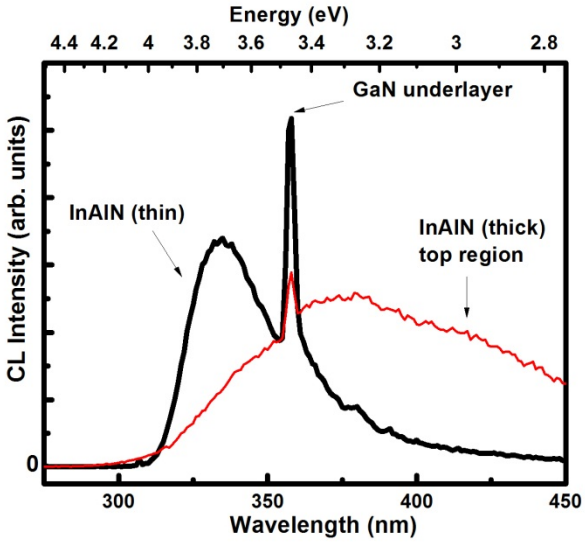

Fig. 7.7. Cathodoluminescence spectra of InAlN epilayers with thickness of 140 nm and 500 nm. The InAlN emission becomes broader and red-shifted for the thicker film.

7.7 CONCLUSION

Compositional variations have been observed in thick InAlN epilayers. InAlN latticed-matched to GaN requires an indium content close to the miscibility gap at typical growth temperatures. The compositional instability is triggered by the presence of threading screw dislocations that open up into a faceted inverted pyramidal shape. InAlN crystallites with lower indium content nucleate heterogeneously on the facets of coreless dislocations. Two regions with distinct chemical composition and microstructural features are formed. The degraded crystal quality results in a defect-related broad optical emission.

REFERENCES

[1] J. F. Carlin and M. Ilegems, Appl. Phys. Lett. **83**, 668 (2003).

[2] R. Butté, J.-F. Carlin, E. Feltin, M. Gonschorek, S. Nicolay, G. Christmann, D. Simeonov, A. Castiglia, J. Dorsaz, H. J. Buehlmann, S. Christopoulos, G. Baldassarri Höger Von Högersthal, A. J. D. Grundy, M. Mosca, C. Pinquier, M. A. Py, F. Demangeot, J. Frandon, P. G. Lagoudakis, J. J. Baumberg, and N. Grandjean, J. Phys. D **40**, 6328 (2007).

[3] F. A. Ponce, S. Srinivasan, A. Bell, L. Geng, R. Liu, M. Stevens, J. Cai, H. Omiya, H. Marui, and T. Tanaka, Phys. Stat. Sol. B **240**, 273 (2003).

[4] V. G. Deibuk and A. V. Coznyi, Semiconductors. **39**, 623 (2005).

[5] S. Pereira, M. R. Correia, E. Pereira, K. P. O'Donnell, C. Trager-Cowan, F. Sweeney, and E. Alves, Phys. Rev. B **64**, 205311 (2001).

[6] M. Hao, H. Ishikawa, T. Egawa, C. L. Shao, and T. Jimbo, Appl. Phys. Lett. **82**, 4702 (2003).

[7] Z. T. Chen, S. X. Tan, Y. Sakai, and T. Egawa, Appl. Phys. Lett. **94**, 213504 (2009).

[8] F. A. Ponce, D. Cherns, W. T. Young, and J. W. Steeds, Appl. Phys. Lett. **69**, 770 (1996).

[9] D. Cherns, W. T. Young, J. W. Steeds, F. A. Ponce, and S. Nakamura, J. Crystal Growth. **178**, 201 (1997).

[10] D. Cherns, W. T. Young, J. W. Steeds, F. A. Ponce, and S. Nakamura, Phil. Mag. A **77**, 273 (1998).

[11] J. E. Northup, L. T. Romano, and J. Neugebauer, Appl. Phys. Lett. **74**, 2319 (1999).

[12] L. Zhou, D. J. Smith, M. R. Mccartney, D. S. Katzer, and D. F. Storm, Appl. Phys. Lett. **90**, 081917 (2007).

[13] I.-H. Ho and G. B. Stringfellow, Appl. Phys. Lett. **69**, 2701 (1996).

[14] J. A. Van Vechten, Phys. Rev. **182**, 891 (1969).

[15] S. Srinivasan, L. Geng, R. Liu, F. A. Ponce, Y. Narukawa, and S. Tanaka. Appl. Phys. Lett. **83**, 5187 (2003).

CHAPTER 8

SUMMARY AND FUTURE WORK

8.1 SUMMARY

In the dissertation, the spontaneous and piezoelectric polarization of group-III nitrides have been investigated both theoretically and experimentally.

In Chapter 3, the orientation dependence of polarization field was calculated under pseudomorphic growth conditions. For the first time, the in-plane polarization fields have been determined. In order to quench the total polarization field for light emitting devices, the semi-polar plane growth was suggested. My results are highly consistent with many more recent experimental reports: (a) the $(11\bar{2}2)$ growth plane with polar angle of 58° and the $(20\bar{2}1)$ plane with polar angle of 75° both exhibit an opposite signs of perpendicular polarization field compared to (0001) plane, from experimental measurements, demonstrating that the crossover angle where the perpendicular polarization field vanishes is at least less than 58°.[1, 2] (b) For non-polar growth (*m*-plane), a double-peak quantum well emission was generally observed and attributed to the in-plane piezoelectric field within the dislocated regions.[3] (c) The recent effort on high-efficiency light emitting devices, especially lasers, is pushing toward semi-polar planes.[4, 5]

In Chapter 4, the band diagram of nitride heterojunction under polarization field was studied by self-consistently solving the Schrödinger and Poisson equation. The computational implementation of the band diagram calculation was discussed in details. Band diagrams of several practical heterostructures were calculated and the optimized device design was discussed: (a) the polarization field in the *c*-plane quantum well can be reduced by introducing the barrier doping, or the triangular quantum well; (b) the 2-

dimensional carrier gas in AlGaN/GaN can be achieved by adopting either a high-doping in the barriers, or a large polarization field.

In Chapter 5 and 6, the electrostatic potential energy profiles for nitride heterostructure designed for 2DHG and 2DEG were measured by electron holography. A p-type AlGaN/AlN/GaN heterostructure was grown on (0001) of wurtzite GaN, in which 2DHG exhibits itself as the positive curvature of potential energy at AlN/GaN interface. The large band offset and polarization discontinuity of AlN/GaN is critical for the formation of 2DHG. A unintentionally-doped AlGaN/GaN heterostructure was grown on the (001) plane of zinc-blende GaN. The negative curvature of potential energy at AlGaN/GaN interface indicates the free electron accumulation. The impurity introduced during the growth of AlGaN is believed to be the source of 2DEG accumulation, while the low 2DEG density is due to the lack of polarization charges. Comparison between experimental measurement and simulation demonstrates that electron holography can provide the information of the electronic bands.

In Chapter 7, InAlN film nearly lattice-matched to GaN which ideally has zero piezoelectric polarization and large spontaneous polarization, was characterized. The $In_xAl_{1-x}N$/GaN system is found to show compositional instability at the lattice-matched composition (x~0.18) in epitaxial layers. The breakdown in compositional homogeneity is triggered by threading dislocations with a screw component propagating from the GaN underlayer, which tends to open up into V-grooves at a certain thickness. The structural breakdown is due to heterogeneous nucleation and growth at the facets of the V-grooves. To prevent this compositional instability and to enhance the epitaxial layer quality, the use of a dislocation-free GaN substrate or growing InAlN/GaN superlattice instead of thick InAlN film is desired.

8.2 FUTURE WORK

The performance of a p-n junction light emitting device is determined by the band diagram under applied bias, in other word, under non-equillibrium conditions where the Fermi level is no longer a constant. It is not straightforward to deduce the band diagram under forward bias from one under zero bias. The drift-diffusion model needs to be included. Therefore, a direct measurement of the band diagram using in-situ electron holography with varied bias is very necessary to solve this problem. A specimen holder in which a voltage can be applied needs to be designed, and overheat from the TEM thin foil needs to be prevented. This experiment could be critical for understanding the polarization effect and for optimizing device design.

Bulk GaN is now commercially available and non-polar and semi-polar growth is being used in industry. [6] Although the dislocation density from GaN underlayers is significantly reduced due to the homoepitaxy, the lattice mismatch between InGaN and GaN in the active region remains large, leading to basal stacking fault for non-polar plane [7-9] and misfit dislocation for semi-polar plane, respectively. [10, 11] The extended defects due to lattice mismatch are fundamental issues for nitride heterostructure LEDs, especially for long wavelength emitters with high indium content. How those defects affect the device performance, such as emission efficiency and degradation lifetime, will be interesting topics. In addition, when the growth plane is tilted toward a non-polar or semi-polar facet, the atomic configuration on the film surface will be different from *c*-plane growth, which leads to a new challenge for metal contact and coating adhesion in the device fabrication.

The strain does not only affect the piezoelectric polarization, but also the valence band electronic structure. It has been reported that the shear strain in some of the semi-

polar plane growth could reduce the effective mass of holes, resulting in a higher gain of GaN-based lasers.[12, 13] It will be required to extend the study on the mechanical strain for arbitrary crystal orientation, in order to fully understand the electronic and optical properties of GaN-based devices with non-*c*-plane growth facet.

REFERENCES

[1] H. Shen, M. Wraback. H. Zhong, A. Tyagi, S. P. Denbaars, S. Nakamura, and J. S. Speck, Appl. Phys. Lett. **94**, 241906 (2009).

[2] C. Y. Huang, M. T. Hardy, K. Fujito, D. F. Feezell, J. S. Speck, S. P. Denbaars, and S. Nakamura, Appl. Phys. Lett. **99**, 241115 (2011).

[3] Y, Huang, K. W. Sun, A. M. Fischer, Q. Y. Wei, R. Juday, F. A. Ponce, R. Kato, and T. Yokogawa, Appl. Phys. Lett. **98**, 261914 (2011).

[4] M. T. Hardy, D. F. Feezell, S. P. Denbaars, and S. Nakamura, Materials Today, **14**, 408 (2011).

[5] H. Ohta, S. P. Denbaars, and S. Nakamura, J. Opt. Soc. Am. B **27**, B45 (2010).

[6] J. W. Raring, M. C. Schmidt, C. Poblenz, B. Li, Y. C. Chang, M. J. Mondry, Y. D. Lin, M. R. Krames, R. Craig, J. S. Speck, S. P. Denbaars, and S. Nakamura, Proc. SPIE. **7939**, 79390Y (2011).

[7] A. M. Fischer, Z. H. Wu, K. W. Sun, Q. Y. Wei, Y. Huang, R. Senda, D. Lida, M. Iwaya, H. Amano, and F. A. Ponce, Appl. Phys. Express **2**, 041002 (2009).

[8] T. Detchprohm, M. Zhu, Y. Li, L. Zhao, S. You, C. Wetzel, E. A. Preble, T. Paskova, and D. Hanser, Appl. Phys. Lett. **96**, 051101 (2010).

[9] F. Wu, Y. D. Lin, A. Chakraborty, H. Ohta, S. P. Denbaars, S. Nakamura, and J. S. Speck, Appl. Phys. Lett. **96**, 231912 (2010).

[10] F. Wu, A. Tyagi, E. C. Young, A. E. Romanov, K. Fujito, S. P. Denbaars, S. Nakamura, and J. S. Speck, J. Appl. Phys. **109**, 033505 (2011).

[11] A. E. Romanov, E. C. Young, F. Wu, A. Tyagi, C. S. Gallinat, S. Nakamura, S. P. Denbaars, and J. S. Speck, J. Appl. Phys. **109**, 103522 (2011).

[12] Y. Enya, Y. Yoshizumi, T. Kyono, K. Akita, M. Ueno, M. Adachi, T. Sumitomo, S. Tokuyama, T. Ikegami, K. Katayama, and T. Nakamura, Appl. Phys. Express **2**, 082101 (2009).

[13] W. G. Scheibenzuber, "GaN-based laser diodes: Towards longer wavelengths and short pulses". Ph. D. Dissertation, Fraunhofer Institute for Applied Solid State Physics, (2012).

APPENDIX A

LIST OF PUBLICATIONS DURING THE STUDY TOWARDS THE DOCTORAL DEGREE

Publications that resulted from my work at ASU are listed below:

[1] Q. Y. Wei, T. Li, J. Y. Huang, F. A. Ponce, E. Tschumak, A. Zado, and D. J. As, "Free carrier accumulation at cubic AlGaN/GaN heteojunctions", Appl. Phys. Lett. **100**, 142108 (2012).

[2] Q. Y. Wei, T. Li, Y. Huang, J. Y. Huang, Z. T. Chen, T. Egawa, and F. A. Ponce, "Compositional instability in InAlN/GaN lattice-matched epitaxy", Appl. Phys. Lett. **100**, 092101 (2012).

[3] Y. Huang, K. W. Sun, A. M. Fischer, Q. Y. Wei, R. Juday, F. A. Ponce, R. Karo, and T. Yokogawa, "Effect of misfit dislocations on luminescence in m-plane InGaN quantum wells", Appl. Phys. Lett. **98**, 261914 (2011).

[4] Z. H. Wu, Y. Q. Sun, J. Yin, Y. Y. Fang, J. N. Dai, C. Q. Chen, Q. Y. Wei, T. Li, K. W. Sun, A. M. Fischer, and F. A. Ponce, "Reduction of structural defects in a-plane GaN epitaxy by use of periodic hemispherical patterns in r-plane sapphire substrates", J. Vac. Sci. Technol. B **29**, 021005 (2011).

[5] Y. Q. Sun, Z. H. Wu, J. Yin, Y. Y. Fang, H. Wang, C. H. Yu, X. Hui, C. Q. Chen, Q. Y. Wei, T. Li, K. W. Sun, and F. A. Ponce, "High quality a-plane GaN films grown on cone-shaped patterned r-plane sapphire substrates", Thin. Solid. Films. **519**, 2508 (2011).

[6] J. P. Liu, Y. Zhang, Z. Lochner, S. S. Kim, J. H. Ryou, S. C. Shen, P. D. Yoder, R. D. Dupuis, Q. Y. Wei, K. W. Sun, A. M. Fischer, and F. A. Ponce, "Performance characteristics of InAlGaN laser diodes depending on electron blocking layer and waveguiding layer design grown by metalorganic chemical vapor deposition", J. Cryst. Growth, **315**, 272 (2011).

[7] Q. Y. Wei, T. Li, Z. H. Wu, and F. A. Ponce, "In-plane polarization of GaN-based heterostructures with arbitrary crystal orientation", Phys. Stat. Sol. A **207**, 2226 (2010).

[8] Q. Y. Wei, Z. H. Wu, F. A. Ponce, J. Hertkorn, and F. Scholz, "Polarization effects in 2-DEG and 2-DHG AlGaN/AlN/GaN multi-heterostructures measured by electron holography", Phys. Stat. Sol. B **247**, 1722 (2010).

[9] H. D. Fonseca-Filho, C. M. Almeida, R. Prioli, M. P. Pires, P. L. Souza, Z. H. Wu, Q. Y. Wei, and F. A. Ponce, "Growth of linearly ordered arrays of InAs nanocrystals on scratched InP", J. Appl. Phys. **107**, 054313 (2010).

[10] F. A. Ponce and Q. Y. Wei, "Polarization fields in high efficiency green LEDs", J. Light. Emitting Diodes **2**, 1 (2010).

[11] Z. H. Wu, K. W. Sun, Q. Y. Wei, A. M. Fischer, F. A. Ponce, Y. Kawai, M. Iwaya, S. Kamiyama, H. Amano, and I. Akasaki, "Misfit strain relaxation in m-plane epitaxy of InGaN on ZnO", Appl. Phys. Lett. **96**, 071909 (2010).

[12] T. Li, A. M. Fischer, Q. Y. Wei, F. A. Ponce, T. Detchprohm, and C. Wetzel, "Carrier localization and nonradiative recombination in yellow emitting InGaN quantum wells", Appl. Phys. Lett. **96**, 031906 (2010).

[13] Q. Y. Wei, Z. H. Wu, K. W. Sun, F. A. Ponce, J. Hertkorn, and F. Scholz, "Evidence of Two-Dimensional Hole Gas in p-Type AlGaN/AlN/GaN Heterostructures", Appl. Phys. Express **2**, 121001 (2009).

[14] F. A. Ponce, Q. Y. Wei, Z. H. Wu, H. D. Fonseca-Filho, C. M. Almeida, R. Prioli, and D. Cherns, "Nanoscale dislocation patterning by scratching in an atomic force microscope", J. Appl. Phys. **106**, 076106 (2009).

[15] J. Hertkorn, S. B. Thapa, T. Wunderer, F. Scholz, Z. H. Wu, Q. Y. Wei, F. A. Ponce, M. A. Moram, C. J. Humphreys, C. Vierheilig, and U. T. Schwarz, "Highly conductive modulation doped composition graded p-AlGaN/(AlN)/GaN multiheterostructures grown by metalorganic vapor phase epitaxy", J. Appl. Phys. **106**, 013720 (2009).

[16] R. Li, J. M. Zhang, L. Chen, H. Zhao, Z. Yang, T. Yu, D. Li, Z. C. Liu, W. H. Chen, Z. J. Yang, G. Y. Zhang, Z. Z. Gan, X. D. Hu, Q. Y. Wei, T. Li, and F.A. Ponce, "Donor-related cathodoluminescence of p-AlGaN electron blocking layer embedded in ultraviolet laser diode structure", Appl. Phys. Lett. **94**, 211103 (2009).

[17] Z. W. Yang, R. Li, Q. Y. Wei, T. Yu, Y. Z. Zhang, W. H. Chen, and X. D. Hu, "Analysis of optical gain property in the InGaN/GaN triangular shaped quantum well under the piezoelectric field", Appl. Phys. Lett. **94**, 061120 (2009).

[18] A. M. Fischer, Z. H. Wu, K. W. Sun, Q. Y. Wei, Y. U. Huang, R. Senda, D. Iida, M. Iwaya, H. Amano, and F. A. Ponce, "Misfit strain relaxation by stacking fault generation in InGaN quantum wells grown on m-plane GaN", Appl. Phys. Express. **2**, 041002 (2009).